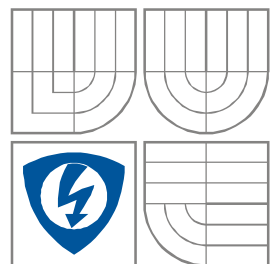# VYSOKÉ UČENÍ TECHNICKÉ V BRNĚ
BRNO UNIVERSITY OF TECHNOLOGY

FAKULTA ELEKTROTECHNIKY A KOMUNIKAČNÍCH TECHNOLOGIÍ
ÚSTAV RADIOELEKTRONIKY

FACULTY OF ELECTRICAL ENGINEERING AND COMMUNICATION
DEPARTMENT OF RADIO ELECTRONICS

RECONSTRUCTION OF THE ANTENNA NEAR-FIELD
REKONSTRUKCE BLÍZKÉHO POLE ANTÉN

DISERTAČNÍ PRÁCE
DISSERTATION THESIS

AUTOR PRÁCE   Ing. Jan Puskely
AUTHOR

VEDOUCÍ PRÁCE   doc. Ing. Zdeněk Nováček, CSc.
SUPERVISOR

BRNO, 2010

Abstrakt

Cílem disertační práce je navrhnout efektivně pracující algoritmus, který na základě bezfázového měření v blízkém poli antény bude schopen zrekonstruovat komplexní blízké pole antény resp. vyzařovací diagram antény ve vzdáleném poli.

Na základě těchto úvah byly zkoumány vlastnosti minimalizačního algoritmu. Zejména byl analyzován a vhodně zvolen minimalizační přistup, optimalizační metoda a v neposlední řadě i optimalizační funkce tzv. funkcionál. Dále pro urychlení celého minimalizačního procesu byly uvažovány prvotní odhady. A na závěr byla do minimalizačního algoritmu zahrnuta myšlenka nahrazující hledané elektrické pole několika koeficienty.

Na základě předchozích analýz byla navržená bezfázová metoda pro charakterizaci vyzařovacích vlastností antén. Tato metoda kombinuje globální optimalizaci s obrazovou kompresní metodou a s lokální metodou ve spojení s konvečním amplitudovým měřením na dvou površích. V našem případě je globální optimalizace použita k nalezení globálního minima minimalizovaného funkcionálu, kompresní metoda k redukci neznámých proměnných na apertuře antény a lokální metoda zajišťuje přesnější nalezení minima. Navržená metoda je velmi robustní a mnohem rychlejší než jiné dostupné minimalizační algoritmy.

Další výzkum byl zaměřen na možnosti využití měřených amplitud pouze z jednoho měřícího povrchu pro rekonstrukci vyzařovacích charakteristik antén a využití nového algoritmu pro rekonstrukci fáze na válcové geometrii.

Klíčová slova

Blízké pole antén, rekonstrukce fáze, rovinné a válcové snímání blízkého pole, bezfázová měření, globální optimalizace, obrazové kompresní metody, Fourierův iterační algoritmus.

Abstract

The aim of this dissertation thesis is to design a very effective algorithm, which is able to reconstruct the antenna near-field and radiation patterns, respectively, from amplitude-only measurements.

Under these circumstances, the properties of minimization algorithm were researched. The selection of the minimization approach, optimization technique and the appropriate functional were investigated and appropriately chosen. To reveal the global minimum area faster, the possibilities in the form of initial estimates for accelerating minimization algorithm were also considered. And finally, the idea to represent the unknown electric field distribution by a few coefficients was implicated into the minimization algorithm.

The designed near-field phaseless approach for the antenna far-field characterization combines a global optimization, an image compression method and a local optimization in conjunction with conventional two-surface amplitude measurements. The global optimization method is used to minimize the functional, the image compression method is used to reduce the number of unknown variables, and the local optimization method is used to improve the estimate achieved by the previous method. The proposed algorithm is very robust and faster than comparable algorithms available.

Other investigations were focused on possibilities of using amplitude from only single scanning surface for reconstruction of radiation patterns and the application of the novel phase retrieval algorithm for cylindrical geometry.

Keywords

Antenna under test, phase reconstruction, planar and cylindrical near-field scanning, phaseless near-field measurement, global optimizations, image compression methods, Fourier iterative algorithm

Prohlášení

Prohlašuji, že svou disertační práci na téma „Rekonstrukce blízkého pole antén" jsem vypracoval samostatně pod vedením školitele a s použitím odborné literatury a dalších informačních zdrojů, které jsou všechny citovány v práci a uvedeny v seznamu literatury na konci práce.

Jako autor uvedené disertační práce dále prohlašuji, že v souvislosti s vytvořením této disertační práce jsem neporušil autorská práva třetích osob, zejména jsem nezasáhl nedovoleným způsobem do cizích autorských práv osobnostních a jsem si plně vědom následků porušení ustanovení § 11 a následujících autorského zákona č. 121/2000 Sb., včetně možných trestněprávních důsledků vyplývajících z ustanovení § 152 trestního zákona č. 140/1961 Sb.

V Brně dne 31. srpna 2010

_____
Jan Puskely

Poděkování

Děkuji vedoucímu disertační práce doc. Ing. Zdeňku Nováčkovi, CSc. za účinnou metodickou, pedagogickou a odbornou pomoc a další cenné rady při řešení mé disertační práce. Poděkování patří také celé mojí rodině za podporu v průběhu mého doktorského studia.

V Brně dne 31. srpna 2010

_____
Jan Puskely

Bibliographic citation

PUSKELY, J. *Reconstruction of the antenna near field.* Doctoral thesis. Brno: Brno University of technology, Faculty of electrical engineering and communication, 2010. 122 p.. Supervisor of the doctoral thesis doc. Ing. Zdeněk Nováček, CSc.

List of acronyms

2D FFT	two-dimensional fast Fourier transform
2D FFT^{-1}	two-dimensional inverse fast Fourier transform
AUT	antenna under test
BGA	binary genetic algorithm
CoM	compression method
DCT	discrete cosine transform
DEA	differential evolutionary algorithm
DWT	discrete wavelet transform
EMC	equivalent magnetic current
FF	far field
FIA	Fourier iterative algorithm
GA	genetic algorithm
GO	global optimization
NF	near field
PSO	particle swarm optimization
PWS	plane wave spectrum
RCGA (RVGA)	real-coded genetic algorithm (real-valued genetic algorithm)
RF	radio frequency

List of symbols

A	input data of DCT
$\mathbf{A}$	plane wave spectrum
$A_n(k_z), B_n(k_z)$	modal coefficients
b	randomly chosen constant in GAs
B	output data of DCT
C	observation curve
$c_{ji,G+1}$	child vector in DEA
D	largest dimension of the antenna aperture
d	separation between two probes in hybrid method
$\mathbf{E}\ (E_z, E_\phi)$	tangential components of the electric field
$E(s)$	field radiated by the antenna under test AUT on the observation curve C
E_1	computed complex electric field values on the first plane
E_2	computed complex electric field values on the second plane
F	scaling factor in DEA
$F(\xi)$	reduced field obtained from the field $E(s)$
g_n	position of the global optimum of the whole swarm in PSO
H	height of the scanning plane (cylinder)
$H_n^{(1)}$	Hankel function of the first kind and order n
$H(k_x, k_y)$	propagation phase function
K	restriction factor in PSO
k	wave number
k_x	spatial frequency in direction of axes x
k_y	spatial frequency in direction of axes y
M	number of the rows in matrix A
$\widetilde{M}_1$	measured amplitude on the first plane
$\widetilde{M}_2$	measured amplitude on the second plane
N	number of the columns in matrix A
Np	number of the individuals in population in DEA
N_z	number of the samples along the z axis

N_ϕ	number of the samples along the ϕ versor
P	largest dimension of scanning probe
p_c	probability of crossover in GAs
p_{c}	probability that the parent vector becomes the child vector in DEA
p_{dn}	n^{th} parameter in the father chromosome in GAs
$\mathbf{p}_{\mathrm{i,G}}$	parent vector in DEA
p_m	probability of mutation in GAs
p_{m}	probability of the mutation in DEA
p_{mn}	n^{th} parameter in the mother chromosome in GAs
p_n	position of the personal optimum of the nth agent in PSO
PS	population size
R_1, R_2	radii of the scanning cylinders
R_{min}	minimum radius of the scan cylinder enclosing AUT
$\mathbf{T}$	dyadic linear operator connecting $\mathbf{E}$ to the corresponding tangential near field components over the second surface
$t_{ji,G+1}$	trial vector in DEA
V_1	complex signals obtained by integrated probe 1
V_2	complex signals obtained by integrated probe 2
v_n	velocity vector of the nth agent in PSO
x_n	position of the nth agent in PSO
Δt	time step in PSO
Δs	sampling step observation curve C
Δx	sampling step in x axis
Δy	sampling step in y axis
$\Delta \phi$	sampling step along the ϕ versor
$\Delta \varphi$	unknown phase shift between the signals V_1 and V_2
λ	wavelength
φ_1, φ_2	acceleration constants in PSO
π	Ludolph's number
θ_{max}	valid (critical) angle

Table of contents

1 Introduction

All today's wireless communication systems contain one key element, an antenna of some form. This antenna serves as the transducer between the controlled energy residing within the system and the radiated energy existing in free space. In order to satisfy the system requirements, a suitable antenna must be chosen and its performance must be evaluated.

The characterization of the antenna performance can be achieved by measurement in the near-field region or far-field region of the antenna. Information available from field measurements includes: far-field pattern, antenna gain, antenna directivity, axial ratio, beamwidth, phase center position etc. [1], [4].
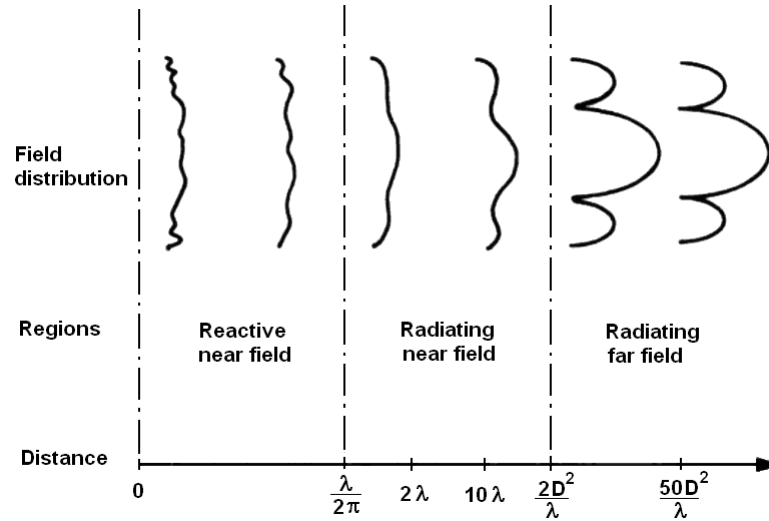
Fig. 1.1 Exterior fields of radiating antenna

Fig. 1.1 depicts the regions into which the exterior fields of a radiating antenna are commonly divided. The transitions between these regions are not distinct and changes between them are gradual [2], [3].

The reactive near-field region is the region close to the antenna and up to about $\lambda/2\pi$ away from any radiating surface. λ is the wavelength. In the reactive region, the energy decays very rapidly with distance. In the radiating near-field region, the average energy density remains fairly constant at different distances from the antenna, although there are localized energy fluctuations. The near-field test system measures the energy in the radiating near-field region and converts those measurements by a Fourier transform into the far-field result. The radiating near-field region extends from the reactive region boundary out to a distance defined as, $2D^2/\lambda$ with D being the largest dimension of the antenna aperture. The far-field region is beyond this distance where the angular distribution of the energy does not vary with distance, and the power level decays according to the inverse square law with distance.

1.1 Far-field vs. Near-field measurement

Any antenna can be successfully measured either in the near-field or in the far-field range, with appropriate implementation. There are significant cost, size, and complexity details which will lead to a recommendation of one type over the other.

Far-field ranges are a better choice for lower frequency antennas and where simple pattern cut measurements are required, and near-field ranges are a better choice for higher frequency antennas and where complete pattern and polarization measurements are required [3]. Table 1.1 summarizes some pros and cons of the far-field measurements and near-field measurements, respectively [1].

Table 1.1 Comparison of the FF and NF measurement properties

	NEAR-FIELD			FAR-FIELD		
	PLANAR	CYLIN-DRICAL	SPHERI-CAL	OUTDOOR RANGE	ANECHOIC CHAMBER	COMPACT RANGE
High gain antenna	Excellent	Good	Good	Adequate	Adequate	Excellent
Low gain antenna	Poor	Good	Good	Adequate	Good	Excellent
High frequency	Excellent	Excellent	Excellent	Good	Poor	Excellent
Low frequency	Poor	Poor	Good	Good	Fair	Poor
Gain measurement	Excellent	Good	Good	Excellent	Good	Excellent
Close sidelobes	Excellent	Excellent	Excellent	Good	Poor	Excellent
Far sidelobes	Adequate	Excellent	Excellent	Good	Poor	Good
Low sidelobes	Excellent	Excellent	Excellent	Variable	Poor	Good
Axial ratio	Excellent	Excellent	Excellent	Good	Poor	Good
Zero G effects	Excellent (hor. mode)	Poor	Good (hor. mode)	Poor	Poor	Poor
Multipath	Good	Good	Good	Adequate	Adequate	Good
Weather	Excellent	Excellent	Excellent	Poor	Excellent	Excellent
Security	Excellent	Excellent	Excellent	Poor	Excellent	Excellent
Facility cost	Low	Moderate	Moderate	High	Moderate	Very high
Operating cost	Moderate	Moderate	Moderate	High (remote)	Moderate	Moderate
Speed (complete measurem.)	Excellent	Good	Fair	Fair	Fair	Fair
Speed (simple cuts)	Good	Fair	Fair	Excellent	Excellent	Excellent
Complexity	Moderate	Moderate	High	Moderate	Low	High
Mechanical surface measurements	Excellent	No	No	No	No	No
Antenna access	Excellent	Excellent	Excellent	Good	Good	Fair
Antenna alignment	Easy	Moderate	Difficult	Moderate	Moderate	Difficult

Generally, standard far-field antenna measurement cannot be made for very large antennas for which the far-field distance becomes too large to fit within actual test range or an anechoic chamber. Measurement can then only be made in the near field. In addition standard far-field measurements do not show what happens in the close vicinity of the antenna. Near-field measurements provide a fast and accurate method of determining the antenna properties. The advantage of near-field measurements is a complete characterization of the antenna performance (far-field pattern, antenna gain, antenna directivity, axial ratio, beamwidh, phase center position, etc.).

1.2 Measurement in the near-field

Near-field measurements are used where large antennas are to be tested indoors in a relatively small space. This type of range uses a small RF probe antenna which is scanned over a surface surrounding the test antenna. During the measurement, near-field information is collected over a discrete matrix of points. This data is then transformed to the far-field using suitable techniques [2], [6]. The resulting far-field data can then be displayed in the same formats as conventional far-field antenna measurements.

1.2.1 Conventional measurement methods

Conventional measurement methods in the near-field assume scanning of the amplitude and phase of the electric field [2], [4], [5]. Measurement of antenna near-field is performed in the near-field region lying in the range of distances λ and $2D^2/\lambda$. Magnetic and electric field propagate almost with zero phase shifts in this region, as it is in a far field. The knowledge of the electric field will be considered for this reason.

Assume that the AUT radiates only into the right half-space and planar scanning area is located at defined distance from the AUT (Fig. 1.2). In the basic layout of the measuring site, the probe is connected to the level meter (usually vector analyzer) by means of appropriate transmission lines, such as coaxial cable or waveguide. And this entails two main disadvantages of these standard methods [7]:

• Metal transmission lines, which are in the vicinity of the measured antenna, greatly distort the field by the local short-circuiting tangential components of electric field. This occurs even when using very thin lines.

• Flexible transmission line does not usually provide adequate stability of amplitude and phase measurements at high frequencies.
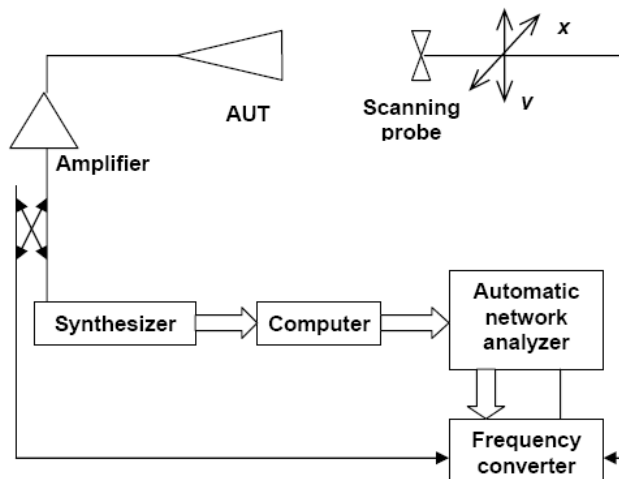

Fig. 1.2 Setup of the conventional near-field measurements [7]

For these two reasons, the direct measurement (amplitude and phase) method is not suitable for testing the near-field in the vicinity of the antenna at high frequencies.

The near-field far-field transformation procedures are based on the knowledge of complex values of the near field. A suitable numerical processing is then applied for the

far field reconstruction. Several transformation schemes have been developed for different geometries of the scanning surface, the choice among them being made according to the radiating properties of the antenna under test (AUT) and to the required hardware complexity. In fact a trade-off between the mechanical specifications on the scanning system and the numerical processing complexity must be made.

Measurement geometries

Which near-field technique is most appropriate depends on the nature of the pattern, the physical size of the antenna, the nature of the available mount and/or probe transport system(s), and the physical size and shape of the portion of the near field in which the amplitude is significant.

In near-field testing, the test antenna is usually aligned to the scanner's coordinate system and then either the probe or the test antenna is moved. In practice it is easier and more cost effective to scan the RF probe over linear axes or the test antenna over angular axes. There are many scanning coordinate systems available for collecting the near-field data. The most commonly used near-field techniques are planar [8]-[10], cylindrical [11] and spherical [12], [13] (Fig. 1.3):
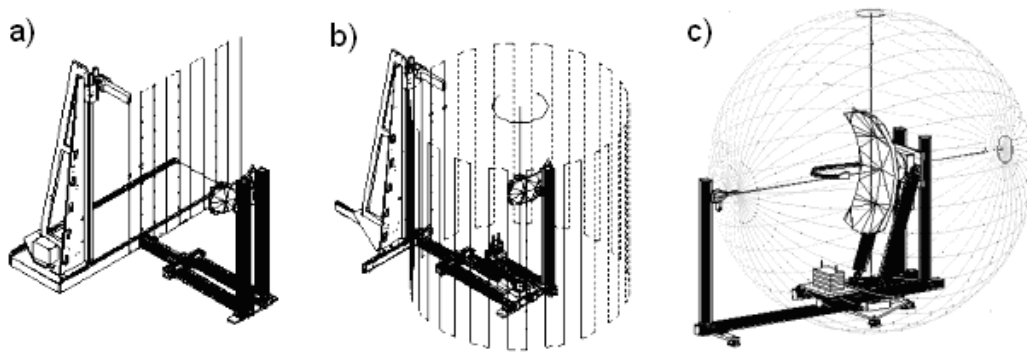
Fig. 1.3 Three different types of near-field scan; a) planar; b) cylindrical; c) spherical [1]

Table 1.2 compares these three standard configurations [2], [3].

Table 1.2 Comparison of the three standard configurations

ANTENNA TYPE/PARAMETER	PLANAR	CYLINDRICAL	SPHERICAL
High-gain Antennas	Excellent	Good	Good
Low-gain Antennas	Poor	Good	Excellent
Stationary AUT	Yes	Possible	Possible
Zero-gravity Simulation	Excellent	Poor	Variable
Alignment Ease	Simple	Difficult	Difficult
Speed	Fast	Medium	Slow

For my doctoral thesis, cylindrical and planar scanning was considered. Firstly, they are relatively simple and they represent the basic measurement method in the near-field. Secondly, they belong among the most widespread and most appropriate methods for their versatility. Cylindrical scanning is often used for antennas which have a narrow pattern on one axis and a broad pattern on a second axis but can be used also for directional antennas. Planar scanning is suitable for high-gain antennas.

1.2.2 Contemporary methods of the phase distribution reconstruction

As was already mentioned, high accuracy in the reconstructed pattern requires high accuracy in the measured amplitude and phase of the near field. Such accuracy is much more difficult to achieve for the phase measurement than for the amplitude one. In fact, the probe positioning errors of the scanning system result essentially in uncertainties on the detected phase. Furthermore, the phase measurement is more sensitive to the equipment inaccuracies than the amplitude one. Therefore, it is necessary to use sophisticated measuring devices, which, however, are correspondingly costly. With increasing frequency, the complexity and cost of these devices is increasing significantly. Efforts to avoid the phase measurement lead through phaseless measurements, i.e. to obtain radiation patterns in the far region from only the knowledge of the amplitude distribution in the near region. At present, microwave holography technique and phase retrieval techniques are the most promising techniques of the measurement without knowledge of the distribution phase in the near region.

1.2.2.1 Microwave holography technique (interferometric method)

Microwave holography is based on Gabor's holography used in electron microscopy [20]. In principle, the holographic method determines the amplitude wave resulting from the interference between the measured antenna and the reference antenna [21], [22]. The radiation patterns of the measured antenna in the far region are obtained by numerical processing of the diagram field strength. The method of microwave holography has a lot of disadvantages. Distance of the scanning surface from the measured antenna must be greater than in the case of the common scanning in the near field. It degrades the benefits of measurement in the near field. In addition, precision of the method depends on the exact knowledge of the impedance and radiation characteristics of the reference antenna since for obtaining the radiation patterns of the measured antenna, it is necessary to remove the reference wave from the measured signal. And finally, it is the stability of the reference wave which must be ensured throughout the whole measurement. Due to these difficulties, holographic methods are not widespread.

1.2.2.2 Phase retrieval techniques

Phase retrieval techniques are based on only-amplitude measurements in the near region. Phase information is restored using numerical minimize and iterative methods. The idea of the phase reconstruction from only the amplitude is not completely new; it comes from other scientific areas of the electromagnetic theory, especially from optics domain and electron microscopy. In the antennas domain, the idea appeared only in the 1980s and the first works interested in near-field measurement based on amplitude only were published by Naples group of scientists at the beginning of the 1990s [23]. They used the method of functional minimization for reconstruction of phases. During the 1990s, the scientists from the University of California (UCLA) started to solve the problem of phase reconstruction too. In contrast to Italian group they use simple Fourier iterative algorithm [28].

At the beginning of the 2000s, local optimization procedure utilizing phaseless electric field data over arbitrary shaped surfaces for the reconstruction of an equivalent

magnetic current density which represents the radiating structure or an antenna under test was exploited [31].

In an attempt to make use of the benefits of interferometric and functional methods, a novel hybrid procedure for far-field reconstruction from phaseless near-field data was proposed by a scientist from university of Calabria in 2005 [35]. Basically, interferometric approach was adopted to retrieve the near-field phase from amplitude-only measurements, which were collected by a simple microstrip circuit used in conjunction with two identical probes moving on the scanning surface.

Functional minimization method

The functional minimization method is based on the minimization of the difference between the calculated amplitudes and measured ones on two surfaces in the near-field region. The aim is to reveal the minimal function representing the complex intensity of the electric field distribution. If the phase distribution is known, we are able to determine the antenna radiation patterns.

Known minimization algorithms were used to solve the functional. These algorithms can be divided into local and global ones. The local minimization is used when choosing an initial estimate in the area of the global minimum. In contrast, the use of the global algorithm is not conditioned by any choice of the initial estimation, but the convergence can slow down [7].

Appropriate choice of the minimizing method and proper geometric arrangement of scanning planes affect significantly the resulting accuracy of the reconstructed radiation patterns. At present, the functional minimization is mainly based on the local minimization methods (e.g. the Newton method) [23]. Generally, a functional has not only one minimum, but shows, except global minimum, several local minima. The number of local minima increases with increasing error rate of measured amplitudes [27]. To ensure that the minimizing process does not get stuck in a local minimum, several approaches can be used.

- Appropriate choice of the initial estimate of the field distribution which must lie in the area of the global minima. To obtain the initial estimate, roughly measured phase on one of the scanning planes is usually used. It was proved that if the roughly measured phase is in range of ±45°, the method converges to the global minimum. Otherwise, the method gets stuck in a local minimum. This approach can be used to improve the measured values loaded by phase error caused by, for example, transmission line, etc. [24].

- Modified functional in the form which shows no local minima [25]. Convergence to the global minimum is guaranteed regardless of the initial estimate chosen. This was achieved by minimizing the differences squared amplitude and appropriate weighting of the minimized functional samples [25]. Another condition necessary for local minima elimination is to use the measured amplitude data which have minimal mutual correlation. This can be achieved by the maximum separation of the scanning planes [25]. However, the need to use a greater distance between the scanning planes themselves brings about the need for larger anechoic chambers. This limitation has been overcome by using two scanning probes instead of the two scanning planes [26]. In practical terms, it means replacing two sets of the measured amplitude on the two planes with two sets of the measured amplitude on a single plane, but using two different

measuring probes (with different radiation patterns). The same condition of the minimum mutual correlation must apply for amplitude files. In other words, the scanning probes must have as different radiation patterns as possible.

- Using global optimization techniques for finding the global minimum. Particle swarm optimization was used for minimizing of the functional [7]. In contrast to the local minimization, the use of the global approach is not conditioned by the choice of the initial estimate and an additional modification of the minimized functional. On the other hand, minimizing process is not able to reach accurate results and also the convergence is relatively very slow. To ensure the required precision of the radiation patterns, the Fourier iterative algorithm FIA is applied [28].

Fourier iterative algorithm

Fourier iterative algorithm also minimizes the similarly defined functional. Initial estimate is refined in every step and the whole cycle is finished when difference between the current and the previous value is less than the defined value or when the difference between measured and estimated amplitudes is less than required accuracy. Iterative algorithm is simpler and more straightforward compared to the method of functional minimization since it does not need to implement any numerical methods to minimize the functional [28]. On the other hand, convergence can be slower than by using numerical methods.

The success of using Fourier iterative algorithm as well as other local methods depends on the choice of the initial estimation of the electric field on the antenna aperture. If this initial estimation is very rough, the method can get stuck in a local minimum [28]. Recently, the initial estimation was obtained by phase distribution roughly measuremed on one of the scanning planes [29].

At present, it is the electric field distribution on the antenna aperture obtained by transformation of the amplitude distribution from the first scanning plane and followed by cutting to the size of the antenna aperture which is used for the choice of the initial estimation [7]. The disadvantage is that this estimation can not be used for antennas with significantly non-uniform distribution in the antenna aperture. Further, the global optimization technique, differential evolutionary algorithm (DEA), is used in conjunction with Fourier iterative algorithm [30].

Method based on reconstruction of equivalent magnetic currents (EMC)

Previous methods led to an iterative scheme in which the phase of the known amplitude near field data at two different planes was reconstructed in a forward-backward fashion.

In this part, a method which reconstructs directly the sources from the knowledge of the electric field data over some region is introduced. The sources are established in terms of an equivalent magnetic current (EMC) density and are used to represent the AUT as an EMC distribution that encloses the AUT. From this representation, a relationship between sources and the electric field data over some region can be established through a full-wave integral equation [34]. NF-FF transformation has been considered the main application, although the calculation of the EMC distribution can also be useful for diagnostics when the algorithm is applied to planar antennas.

At the beginning of the 1990s, the technique which uses equivalent currents and a matrix method to reconstruct far field exploited the amplitude and phase information on arbitrary scanning surfaces [31], [32].

In 2002, the amplitude-only data were used and the cost function regarding the difference between the known amplitude data and the field radiated by the EMC distribution was defined [33]. The conjugate gradient method was used to minimize the cost function and obtain the EMC distribution. Finally, the electric field data could be calculated at any point from this EMC distribution. The surface of the measured amplitude data (measurement domain) does not need to be restricted to the typical two planes usually defined, but can be defined on arbitrary domains of the nonplanar measurement surfaces which can be of any arbitrary number. The accuracy of the method depends on the amount of information fed to the optimization procedure.

The advantage of this integral representation is that the near-field sampling does not need to satisfy the Nyquist sampling criteria. The possibility of measuring amplitude-only data over arbitrary surfaces and the source diagnosis capabilities makes this technique an alternative to the classic iterative phase retrieval schemes [33].

The disadvantage is the low accuracy of this technique when using measured amplitude-only field data on one surfaces. Amplitude measurements over two planes improve the accuracy, while the quality of the results using amplitude information on one scanning surface can vary depending on the problem [33]. The method also suffers from high numerical complexity and large computational efforts.

Novel hybrid approach combining interferometric method and minimization method

This hybrid procedure combines all the best features of the interferometric methods and minimization phaseless methods [35]. Basically, an interferometric approach is adopted, while avoiding the use of a reference antenna as in standard interferometry [22]. The phase reference is directly obtained from the field radiated by the AUT. Two identical probes simultaneously moving over an arbitrary measurement surface are connected to a simple microstrip circuit where incoming probe signals interfere and produce signals for the following interferometric algorithm [36]. This method provides currently the best phaseless measurements.

Thus, the necessary amplitude information is obtained and subsequently processed by a simple interferometric algorithm. Depending on the distance between the probes, a certain number of sets of complex near-field measurements is obtained and from these sets, constant phase-shifts are determined, one for each set. A proper objective functional is minimized respecting the unknown constant shifts. The proposed methodology leads in principle to the evaluation of the near-field phase on the scanning surface. The two probes approach was firstly proposed in [36] and [37] for a single frequency and the planar/plane-polar scanning geometries and then it was extended to an arbitrary scanning surface and improved to cover the entire X-band [37].

The proposed approach is placed "halfway" between interferometric techniques and functional relationship based methods. In particular, it takes advantage of the interferometric approach to reduce significantly the number of unknowns in the phase retrieval algorithm. Although the functional to be minimized is highly nonlinear, the lower number of unknowns, given by the phase shifts, allows an accurate and fast convergence to the solution, acting to decrease the occurrence of local minima.

Compared to the interferometric method, another important advantage of the proposed procedure is related to the absence of a reference antenna, which gives a simpler and more compact measurement setup.

On the other hand, some problems related to the microstrip circuit arise in the practical application of this novel technique. In fact, difficulties are encountered while fixing the distance between the two interference points along the measurement curve. The Nyquist requirement would prescribe a distance equal to $\lambda/2$, the usually adopted sampling step in the NF-FF transformation. However, a larger distance equal to λ or $3\lambda/2$ is required in practice to reduce mutual coupling effects between the scanning probes to a negligible level. This implies a certain number of sets of retrieved near-field phase, resulting from the application of the proposed interferometric technique [35].

1.3 Dissertation aims

Currently, the standard measurement of the near field (measuring amplitude and phase) are implemented in commercial products and NF-FF transformations are brought to perfection at all three types of basic scanning surfaces. Further research in this near field measurements could be aimed at the new scanning geometries and the transformations from near to far field but this is practically impossible without the appropriate equipment. Therefore, searching for the new procedures in the conventional near field measurements is not considered fruitful.

1.3.1 Effective minimization of the functional

Phaseless measurements still represent a current and open problem. This is especially true with respect to the effective minimization of functional which is the biggest issue connected with these methods. Currently, additional information about the measured antenna, rough phase measurement on the whole scanning surface or global optimization are used in minimization methods to avoid getting stuck in a local minimum. One of the main aims of this thesis lies in effective minimization of the functional.

Minimization functional methods suffer from large computational efforts, especially in the cases when we have to analyze radiation properties of electrically large antenna. In this case, the problem description comprises several thousands of unknowns, and CPU-time demands of the minimizing process are enormous. Under these circumstances, there is the idea of representation of the unknown electric field distribution by a few coefficients.

In this thesis, the novel method combining global optimization with compression method is presented. The global optimization method (GO) is used for minimizing the functional and compression method (CoM) is used for reducing the number of unknown variables. This algorithm is used for obtaining the initial estimation. To reach global minima with sufficient accuracy, the common Fourier iterative algorithm is subsequently used.

In order to make this algorithm effective, investigation of using amplitude from only one scanning plane for reconstruction of radiation pattern will be discussed. Thus, the process of obtaining retrieved phase is simplified and made faster.

1.3.2 Application of the novel phase retrieval algorithm for cylindrical geometry

From the mathematical point of view, the planar phase retrieval schemes are least difficult. Their implementation is very easy and therefore they are the subject of the most functional based phase retrieval techniques. Since the cylindrical phase retrieval techniques have received considerably less attention, the novel approach will be applied also for cylindrical geometry which is suitable mainly for omnidirectional antennas.

2 Current minimization methods

The first method is the functional minimization method. The method can exploit local optimization techniques or global ones. When using local approaches, the effectiveness of the algorithm is conditioned by all available additional information of the AUT, or by rough phase measurement in the near-field or by using modified functional which reduces the occurrences of local minima. At present, the functional minimization is based on global optimization techniques which are very robust when searching for the global minimum in a multidimensional domain. In contrast to the local minimization, global algorithms are not conditioned by the choice of the initial estimation lying in the global minimum area. On the other hand, these methods require large computational efforts and their accuracy is not sufficient.

The second method minimizing the functional is the Fourier iterative algorithm. The iterative algorithm is simpler and more straightforward but the convergence can be slower compared to the numerical methods. Success of the Fourier iterative algorithm depends on the choice of the initial estimate.

2.1 Functional minimization method

The functional minimization method is based on the minimization of the difference between the calculated amplitudes and measured ones on one surface and two surfaces, respectively, in the near-field region. The goal of this method is to reveal the minimal function representing the complex intensity of the electric field distribution on the aperture of the measured antenna. If the phase distribution on the aperture is known, we are able to determine both the phase distribution on both scanning surfaces and the antenna radiation patterns.

Except of the electric field distribution on the antenna aperture, the electric field distribution of the one scanning plane or far field in the far region can be minimized also in the reconstruction process. If the far-field (plane wave spectrum) would be minimized, the 181×181 complex parameters for resolution of $1°$ at radiation pattern would be necessary to minimize. When we minimize the field distribution on the scanning plane, only the phase is necessary for minimization (amplitude is known). Since the number of scanning points is high, we get thousands of minimized parameters, which is still a huge amount of unknowns. The field distribution on the antenna aperture was chosen for minimization, because it contains the smallest number of minimized parameters [7].

As was already mentioned, there are two measurement schemes for obtaining the measured amplitudes (Fig. 2.1). The first principle utilizes one probe which scans two surfaces in different distances from AUT and the second one rests in using two scanning probes instead of the two scanning surfaces [23], [26]. In practical terms, it replaces two sets of measured amplitude on two surfaces by two sets of measured amplitude on a single surface, in which case, howerever, two different measuring probes (with different

radiation patterns) are necessary. Although the first principle brings the need to use greater distance between the scanning planes themselves in some cases, this plane scanning strategy will be chosen for simplicity in the following considerations. Since if the omnidirectional probe is used we do not have to consider radiation properties of the scanning probe and the phase retrieval algorithm is simpler.
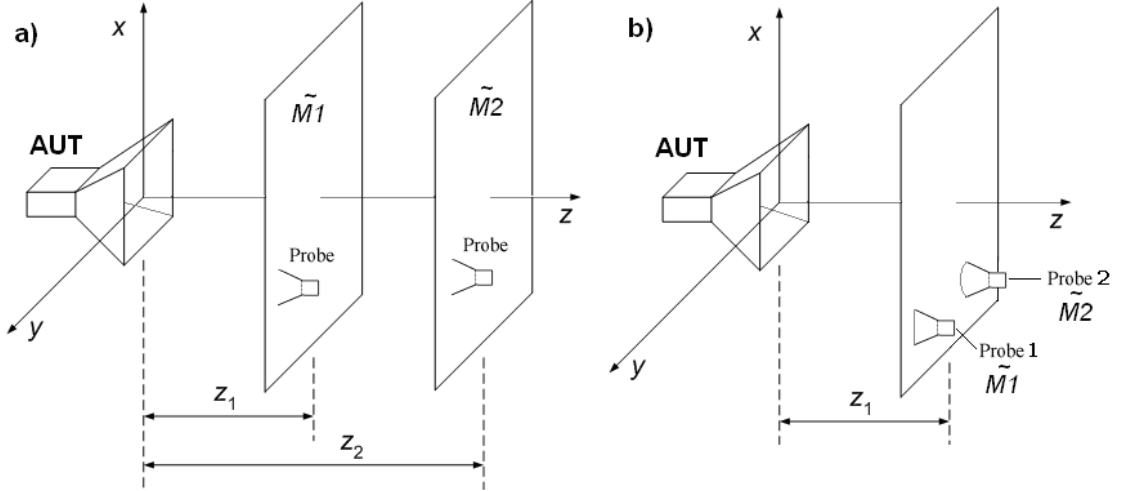

Fig. 2.1   Main principles of the NF antenna plane phaseless measurement.

Planar scanning, sampling theorem and NF-FF transformation

Planar scanning is exploited to measure the directional and highly directional antennas. It is convenient, because bulk radiated power is concentrated in a narrow space angle. Moreover, the used transformations are relatively easy in plane scanning. X-Y plane scanning was chosen (Fig. 2.2).
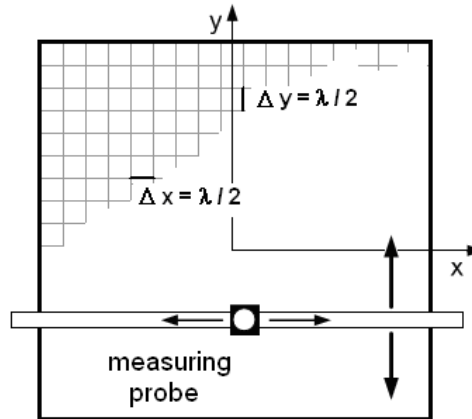
Fig. 2.2   Planar x-y scanning

Assume that we have the measured electric field intensity on the two planes in the near field located at distances $z = z_1$ and $z = z_2$ (Fig. 2.1a). For simplicity, the perfect scanning probe is assumed. Files of the measured amplitudes (actual amplitude plus random error of the measurement) are denote $\tilde{M}_1$ (amplitude on the first plane) and $\tilde{M}_2$ (amplitude on the second plane). The scanning grid on both planes must meet the sampling theorem [4]

$$\Delta x \leq \frac{\lambda}{2}$$

$$\Delta y \leq \frac{\lambda}{2} \qquad\qquad (2.1a, 2.1b)$$

where λ is the wavelength of the measurement frequency.

From the practical point of view, the scanning planes are always finite dimensions. Using the finite plane entails a certain error in the calculated far field. The error depends on the relative intensity of the field lying outside the scanning plane. There is a definition of the critical angle, which is graphically illustrated in Fig. 2.3 [4]. The size of the AUT and the size and location of the finite measurement area define the critical angle θ_{max}. The calculated far-field pattern of the antenna will be accurate in the region between $\pm\theta_{max}$. The size of the critical angle can be expressed by simple empirical relationship [4]

$$\theta_{max} = \arctan\left(\frac{H - D - P}{2d}\right), \qquad\qquad (2.2)$$

where d is distance between AUT and probe, D and P are antenna height and probe height, respectively, and H is height of the scanning plane. The formula (2.2) says that if we want to achieve large critical angle, we must use very high scanning plane located close to the measured antenna.
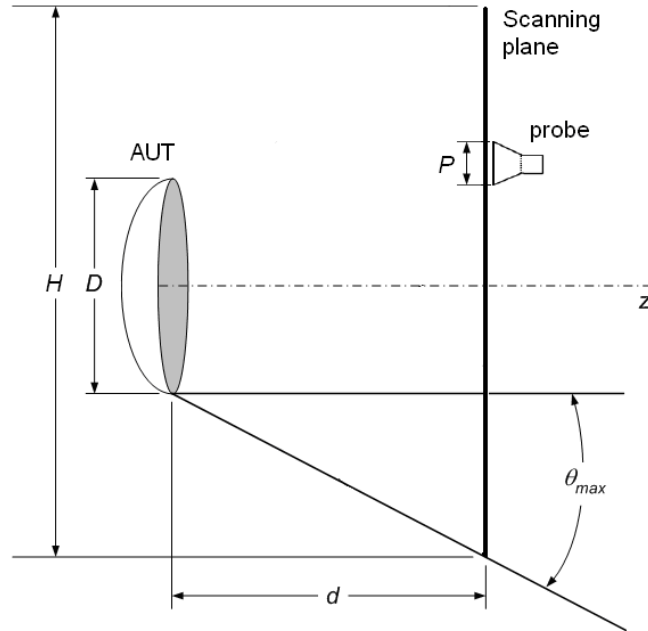
Fig. 2.3 Definition of the critical angle θ_{max}

NF-NF and NF-FF transformations

Relationship between discrete samples of the electric intensity in the near field on plane of the final dimensions and plane wave spectrum (PWS) is represented by two-dimensional Fourier transform [4]

$$\mathbf{A}\left(k_x, k_y\right) = \sum_{n=1}^{N} \sum_{m=1}^{M} \mathbf{E}\left(n\Delta x, m\Delta y, 0\right) e^{-jk_x n\Delta x} e^{-jk_y m\Delta y} \Delta x \Delta y, \qquad (2.3)$$

where $\mathbf{E}(n\Delta x, m\Delta y, 0)$ is a complex vector of electric field measured on the $x(n)^{\text{-th}}$ and y $(m)^{\text{-th}}$ position in the scanning raster in the near field and k_x, k_y are spatial frequencies in the direction of axes x and y and can be defined in spherical coordinate system [4]

$$k_x = k \sin\theta \cos\phi$$

$$k_y = k \sin\theta \sin\phi \qquad (2.4a, 2.4b)$$

In addition, we will consider that the spectrum of plane waves is zero $A(k_x, k_y) = 0$ outside the area of radius ρ, which includes all directions to which $k_x^2 + k_y^2 < \rho^2$ applies. This condition is fulfilled for directional antennas, for which the most electromagnetic energy passes through the scanning planes.

For displacement of the field from one plane to another, the propagation function is used. Thus, the field at plane z_0 (aperture) is related to field at plane z_m by [4]

$$\mathbf{A}\left(k_x, k_y, k_{z_m}\right) = \mathbf{A}\left(k_x, k_y, k_{z0}\right) \cdot H\left(k_x, k_y\right) \qquad (2.5)$$

where the propagation function $H\left(k_x, k_y\right)$ is actually phase function

$$H\left(k_x, k_y\right) = e^{-jz_m \sqrt{1-k_x^2-k_y^2}}. \qquad (2.6)$$

The conjugate $H^*\left(k_x, k_y\right)$ is used for inverse propagation from z_m to z_0.

The goal of the algorithm is to find such distribution of the electric intensity E (module and phase) on the antenna aperture, which corresponds to the amplitude distributions on both planes. The proper distribution of the electric field on the antenna aperture corresponds to the global minimum of the functional [25]

$$\Phi(E) = \left\| |E|^2 - \tilde{M}_1^2 \right\|^2 + \left\| |TE|^2 - \tilde{M}_2^2 \right\|^2, \qquad (2.7)$$

where

$$T = F \cdot e^{-jk_z(z_2-z_1)} F^{-1}, \qquad (2.8)$$

F, F^{-1} denote the direct Fourier transform and inverse Fourier transform, respectively.

Minimizing scheme

The algorithm of the functional minimization assumes knowledge of two amplitude sets, scanning planes distances from the AUT and dimensions of the AUT. The phase retrieval scheme using global optimization approach is shown in Fig. 2.4.
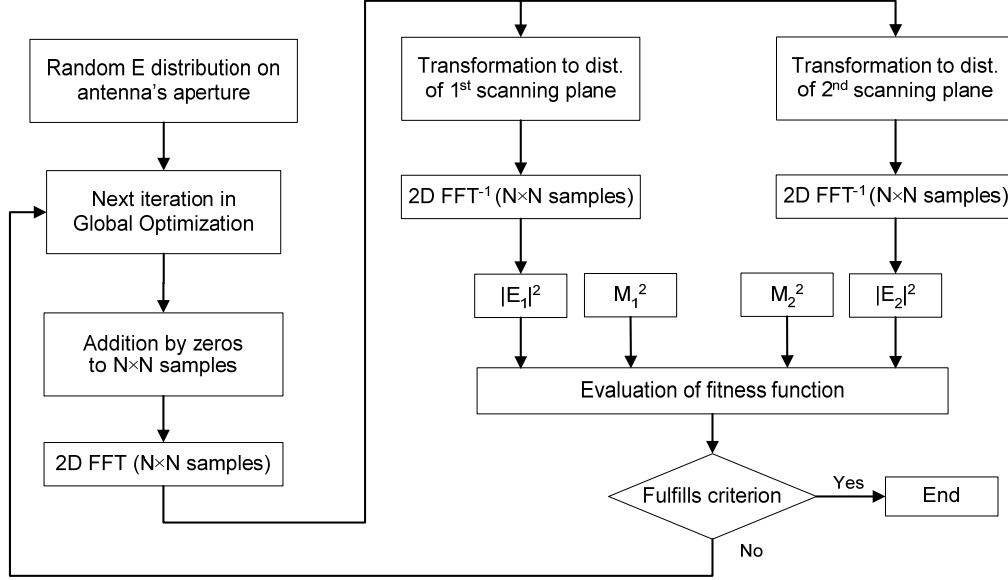
Fig. 2.4 Flow chart of the functional minimization method using GO

The whole minimizing algorithm begins by choosing the initial estimate of the electric field distribution on the antenna aperture. The initial estimate is then completed by zeros to the dimension of the scanning planes. After this adjustment, the electric field intensity on the aperture is transformed to PWS with the help of two-dimensional Fast Fourier Transform (2D FFT). Now we have an estimate of two-dimensional wave spectrum, which is also proportional to the radiation patterns.

At this point, the algorithm branches into two parts differing only in the phase functions and in files of the measured amplitude ($\widetilde{M}_1$ and $\widetilde{M}_2$). Thus, after the two-dimensional Fourier Transform, PWSs are multiplied by phase functions and shifted to the distance of the first scanning plane and the second scanning plane surface, respectively. Subsequently, Inverse Fast Fourier Transform (2D FFT^{-1}) is used for obtaining electric field distribution on both scanning planes from the PWSs.

In the next step, obtained distributions are compared with the measured amplitude and the resulting error is calculated. The calculated errors, corresponding to the defined functional, of the first and second branch are added together. Ideally, i.e. in finding the correct distribution of the electric field on the antenna aperture, the error should be minimum value. The following block represents the appropriate minimizing method that is able to minimize the defined functional, in our case, the global optimization.

The difference between the local scheme which so far was used for the minimization of the functional and the global scheme rests in the fact that for the local scheme, weighted error distributions calculated in distances of scanning planes are transformed back into the plane of the measured antenna aperture. This moreover requires executing four Fourier transformations and two multiplications by phase

functions. Thus, using the global algorithm moreover leads to the reduction of the CPU-time required for evaluating the objective function and to the acceleration of the process. The flow chart of the minimizing algorithm is shown in Fig. 2.4.

2.2 Fourier iterative algorithm

The Fourier iterative algorithm minimizes the functional too. The initial estimation is refined in every step. The whole cycle is finished if the difference between the current value and the previous one is smaller than the defined value or if the difference between the measured amplitudes and the estimated ones is better than the required accuracy. The iterative algorithm is simpler and more straightforward than the method of the functional minimization. On the other hand, the convergence can be slower compared to the numerical methods.

Iterative scheme

The flow chart of the Fourier iterative algorithm is shown in Fig. 2.5. Iterative scheme begins from the initial estimate of the electric field distribution on the measured antenna aperture similarly like minimization method. This estimate is completed symmetrically with zeros to the sample number of the amplitude distribution in both scanning planes. PWS is computed from the electric field distribution by 2D FFT. Subsequently obtained PWS is multiplied by phase function and moved to the first scanning plane. After applying 2D FFT^{-1}, the electric field distribution is obtained back. The fitness function is calculated from the extracted amplitudes and from the measured ones. If the difference between the previous and the current error is less than the desired value, the algorithm is ended and resulting intensity E1 on the first scanning plane is the one which is searched for.

In case the condition is not met, calculated amplitudes $|E1|^2$ are replaced by measured ones and complex electric field distribution is moved back to the plane of the aperture. Now we have a more accurate estimate of the electric field distribution on the antenna aperture and the iterative scheme continues its second half. The second part is exactly the same as the first one, but with the difference that intensities are transformed to the second scanning plane and back. If the condition is not fulfilled, the scheme continues until the maximum number of iterations is reached.

Success of the Fourier iterative algorithm as well as other local methods depends on the choice of the initial estimate. This method is suitable for achieving precise phase in the cases when the phase can not be measured with sufficient accuracy.

Fig. 2.5 Flow chart of the Fourier iterative algorithm

3 Effective minimization of the functional

Both these functional based approaches have some disadvantages. Fourier iterative algorithm is conditioned by the choice of the initial estimate lying in the area of the global minimum. On the other hand, global optimizations allow the choice of a random initial estimate but minimizing process is not able to reach precise results and also the convergence is relatively slow. However, there is the possibility to combine the global optimization and the Fourier iterative algorithm [7]. First, the minimization algorithm is used to find an initial estimate lying in the area of the global minimum. The second part consists of the common Fourier iterative algorithm improving the initial estimate. We will pay particular attention to the minimization method.

Under these circumstances, the properties of minimization algorithm are investigated. Selection of the minimization approach, optimization technique and the appropriate functional influence mainly properties of the algorithm. To reveal the global minimum area faster, the possibilities of accelerating minimization algorithm are also considered. An algorithm of such design works very effectively in case of electrically small antennas.

Problem description comprises several thousands of unknowns, and CPU-time demands of the minimizing process are enormous especially when we have to analyze radiation properties of electrically large antennas. Under these circumstances, the unknown electric field distribution can be represented by a few coefficients. A novel method combining global optimization with a compression method is presented in a different part of this thesis.

Other investigations are focused on the possibilities of using amplitude from only one scanning plane for reconstruction of radiation pattern.

3.1 Investigation of minimization algorithm properties

In this section, different investigations of minimization method properties are presented. The comparisons are carried out on the radiation pattern reconstructions of four different antenna types: antenna array, horn antenna, dish antenna and lens antenna.

3.1.1 Measured and synthesized data of the analyzed antennas

As mentioned above, the analysis was performed on four different sets of data. Data of the horn antenna, dish antenna and lens antenna were measured and data of the antenna array was synthesized. These reconstructions differ primarily in the number of the variables and far field radiation patterns. In case of the horn antenna, radiation pattern is less directional compared to the dish antenna, lens antenna, and antenna array which belong to directional antennas.

3.1.1.1   Choice of scanning plane distances

Measurements of antenna near-field are performed in the near-field region lying in the range of distances λ and $2D^2/\lambda$ and sampling theorem is always met. Methods based on local minimization of functional require a relatively large separation of the scanning surfaces (usually a few wavelengths [19]), to provide as different amplitude distribution as possible. This can be avoided by using an algorithm based on GO [7], [50]. The different separations between the scanning surfaces are considered to involve all possible cases. The separation range is from a half of wavelength and more.

The horn antenna

The horn antenna T1-R100 had the aperture of the size 136×101 mm and the horn length of 173 mm. The antenna was analyzed at the frequency 12.4 GHz. The measurement site is shown in Fig. 3.1. The horn antenna was attached to the tripod so that the longer site of the antenna aperture was parallel to the horizontal plane (H polarization). The scanning probe (the waveguide R100 aperture) was oriented horizontally as well.

Fig. 3.1   Measurement site arrangement

The values of the horizontal electric field intensity component in discrete points were measured by a probe. The points were placed in vertical and horizontal direction with the pitch of 10 mm (0.41λ) at two scanning planes of the size 400×400 mm. Generally, 1 681 (41×41) values on each plane were obtained. The measurement was performed in the Rayleigh zone. The first plane was placed in the distance of 60 mm ($\sim 2.48\lambda$) and the second one in the distance of 70 mm ($\sim 2.89\lambda$) (the distance was measured from the antenna aperture to the waveguide aperture). With respect to the measurement arrangement, the valid angle is $\theta_v = 62^\circ$. Since the aperture of the antenna

is 136×101 mm (15 times 13 sampling points), the solution space contains 390 real parameters the optimal values of which are to be found out.

The contour plots of the amplitude near-field directly measured by the probe at frequency 12.4 GHz are depicted in Fig. 3.2 for both scanning planes. The far-field radiation patterns of the horn antenna obtained by direct transformation of the measured complex near-field are shown in Fig. 3.3 and 3.4.
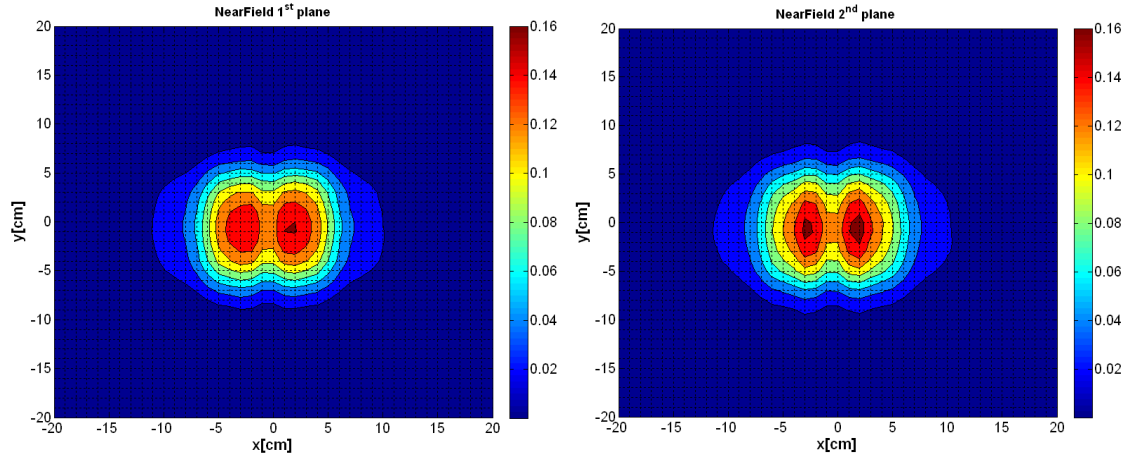
Fig. 3.2 Contour plot of the near-field amplitudes for both scanning planes; horn antenna
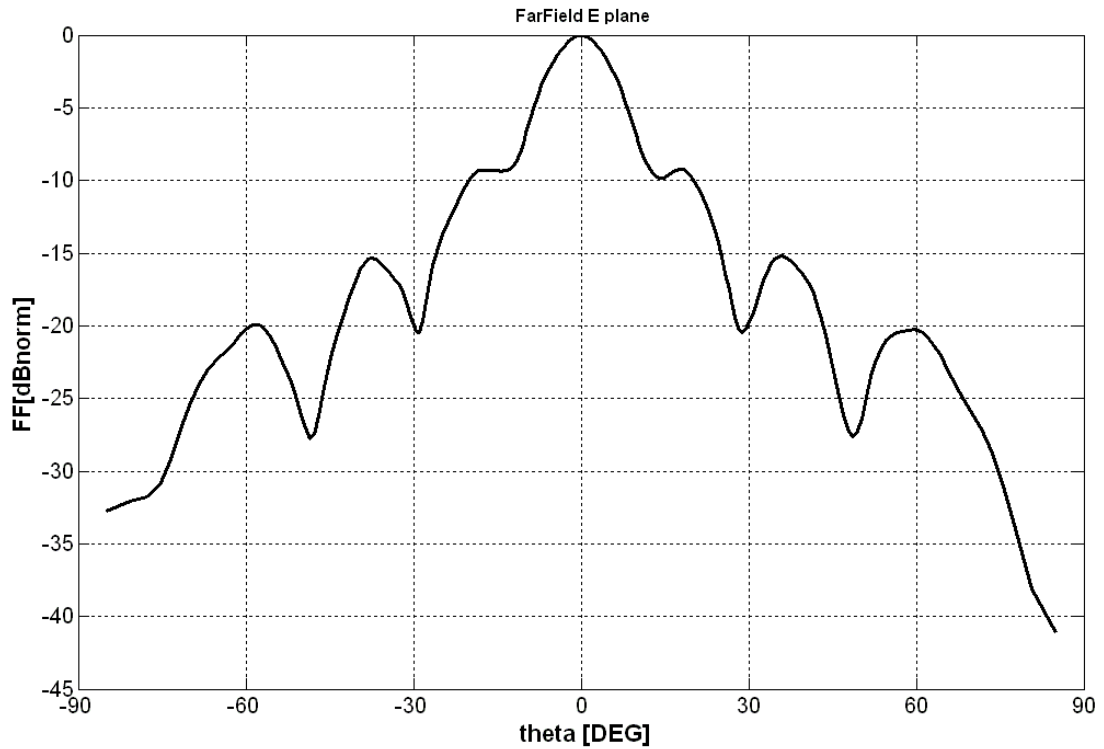
Fig. 3.3 Far-field of the horn antenna obtained by direct transformation of the measured complex near-field; E plane
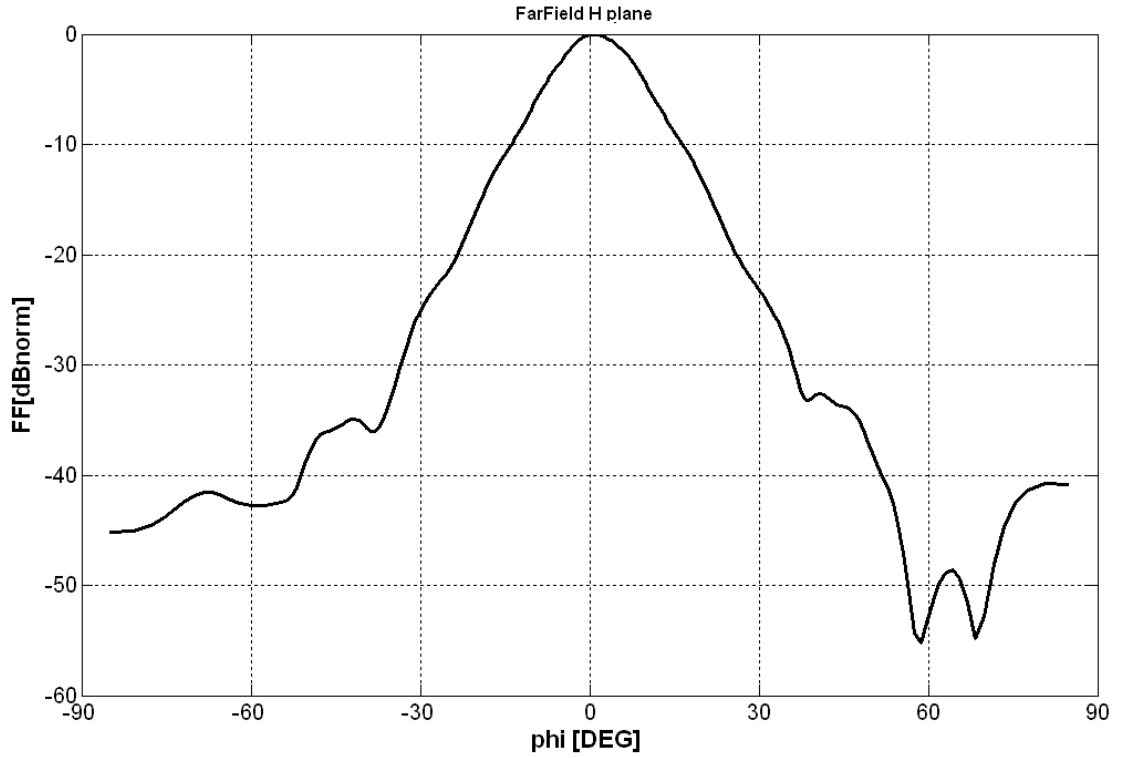
Fig. 3.4 Far-field of the horn antenna obtained by direct transformation of the measured complex near-field; H plane

The dish antenna

The dish antenna with reflector diameter of 0.6 m was the second measured antenna. The measurement site is shown in Fig. 3.5. The antenna was analyzed at the frequency 14.4 GHz. The waveguide R140 was used as the scanning probe. The values of the horizontal electric field intensity component in discrete points were measured. The points were placed in the vertical and horizontal direction with the pitch of 10 mm (0.48λ) at two scanning planes of the size 800×800 mm. Generally, 6 551 (81×81) values on each plane were obtained. The first plane was placed in the distance of 268 mm (~12.86λ) and the second one in the distance of 298 mm (~14.3λ). These distances correspond to the valid angle of $\theta_v = 18.55°$ ($|k_x/k| = |k_y/k| = 0.32$). Since the aperture of the antenna is 600×600 mm (61 times 61 sampling points), the solution space contains 7 442 real parameters the optimal values of which are to be found out.

The contour plots of the amplitude near-field at frequency 14.4 GHz are depicted in Fig. 3.6 for both scanning planes. The far-field radiation patterns of the dish antenna obtained by direct transformation of the measured complex near-field are shown in Fig. 3.7 and 3.8.
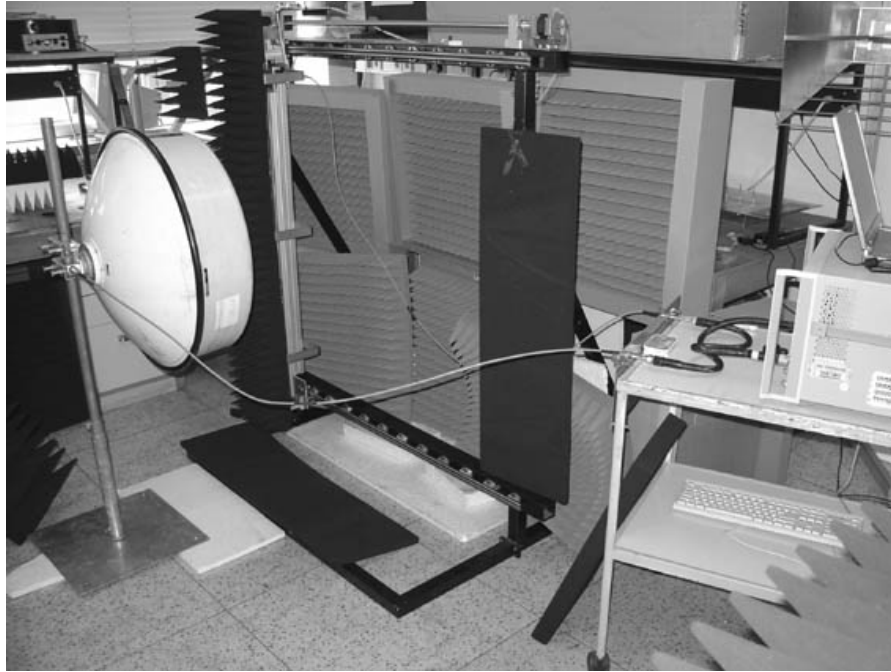
Fig. 3.5   Measuring site for the measurement of dish antenna in the near field
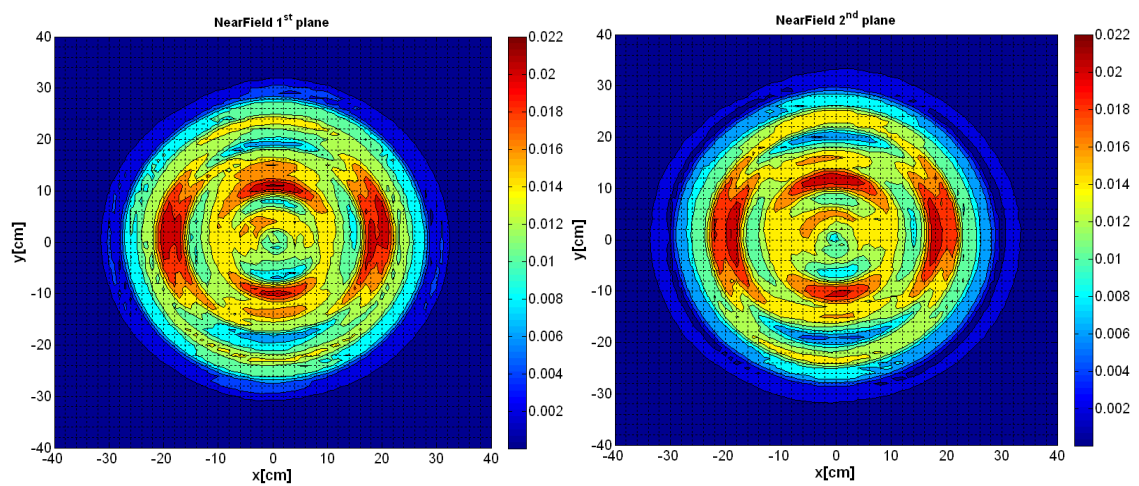
Fig. 3.6   Contour plot of the near-field amplitudes for both scanning planes; dish antenna
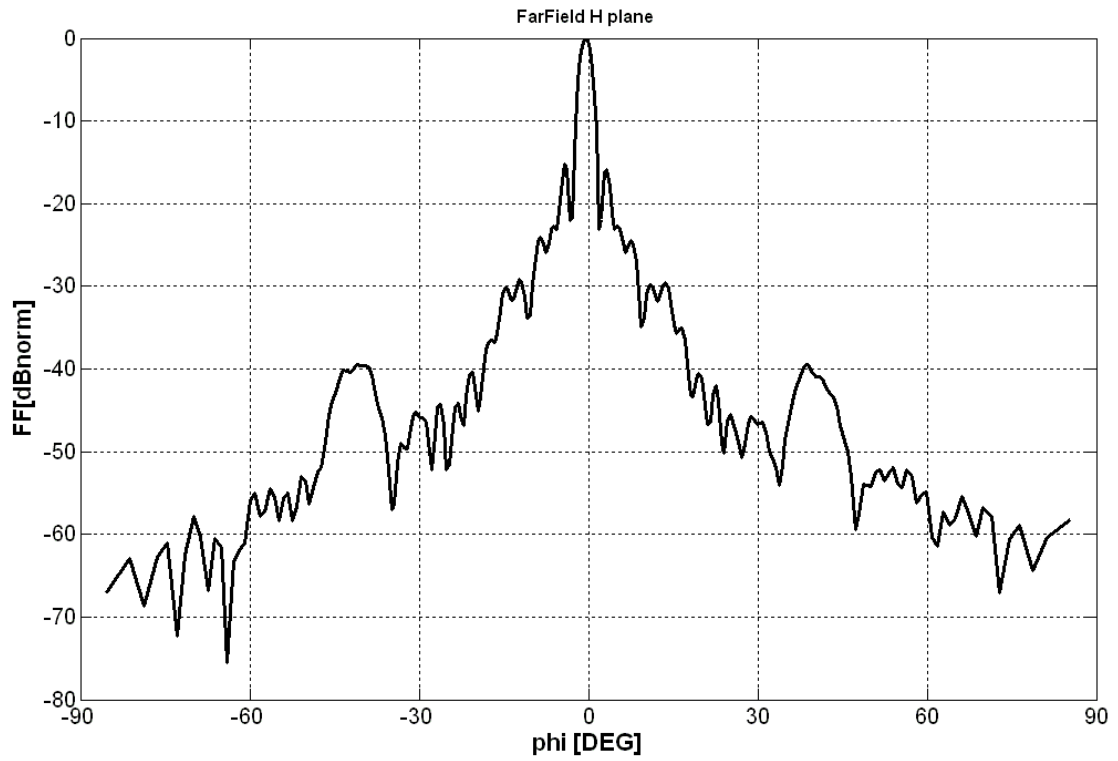
Fig. 3.7 Far-field of the dish antenna obtained by direct transformation of the measured complex near-field; H plane
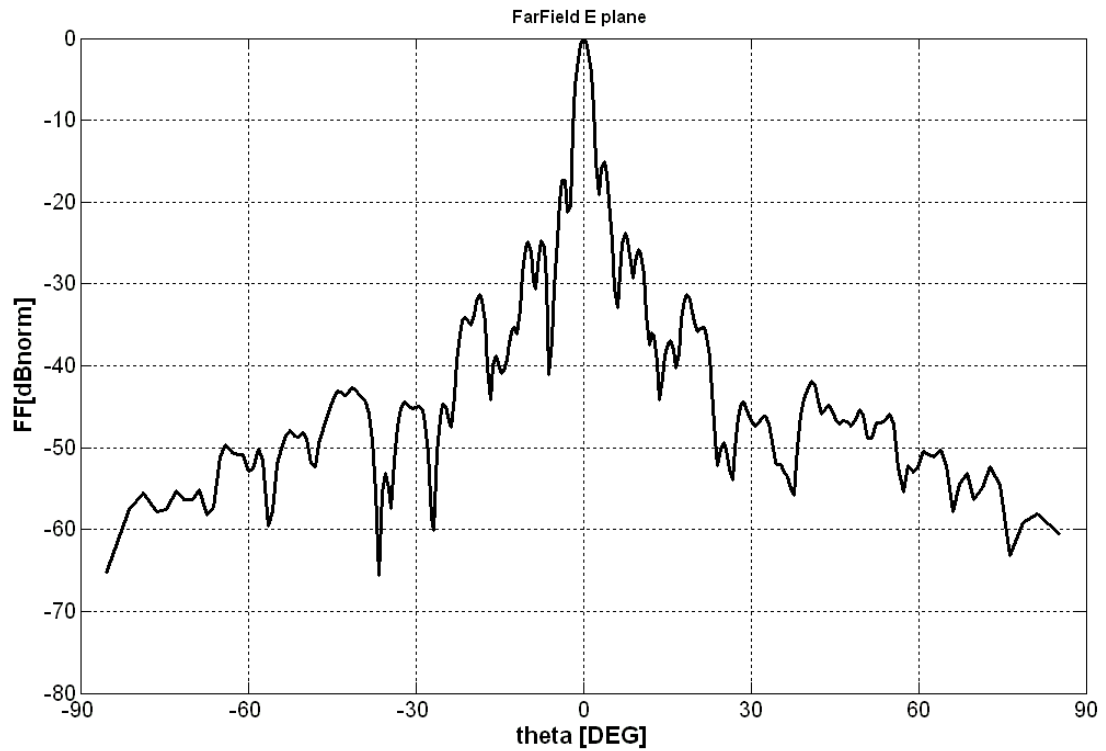
Fig. 3.8 Far-field of the dish antenna obtained by direct transformation of the measured complex near-field; E plane

The Teflon lens antenna

The measurements of the lens antenna for the analysis were carried out at Aalto University School of Science and Technology, Finland (formerly TKK Helsinki University of Technology). The lens antenna and the measurement setup are briefly described in [47]. 423 801

The lens antenna with the reflector diameter of 60 mm was analyzed at frequency 310 GHz. The measurement site is shown in Fig. 3.9. The waveguide WR-3 (0.864 mm×0.432 mm) was used as the scanning probe. The values of the electric field intensity component in discrete points were measured in the vertical and horizontal direction with the pitch of 0.46 mm at two scanning planes of the size 300×300 mm. Generally, 423 801 (651×651) values on each plane were obtained. The first plane was placed in the distance of 120 mm (~116.13λ), and the second one in the distance of 220 mm (~221.9λ). Since the aperture of the antenna is 60×60 mm (135 times 135 sampling points), the solution space contains 36 450 real parameters.
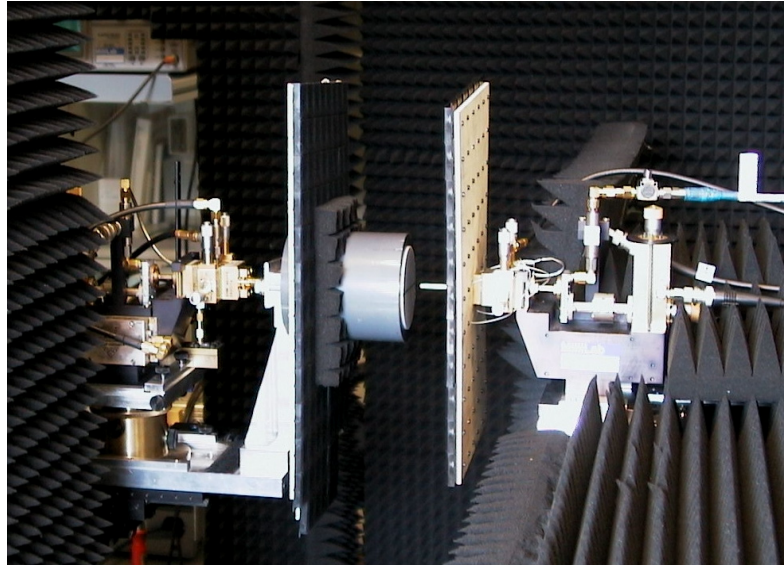
Fig. 3.9 Measurement site arrangement
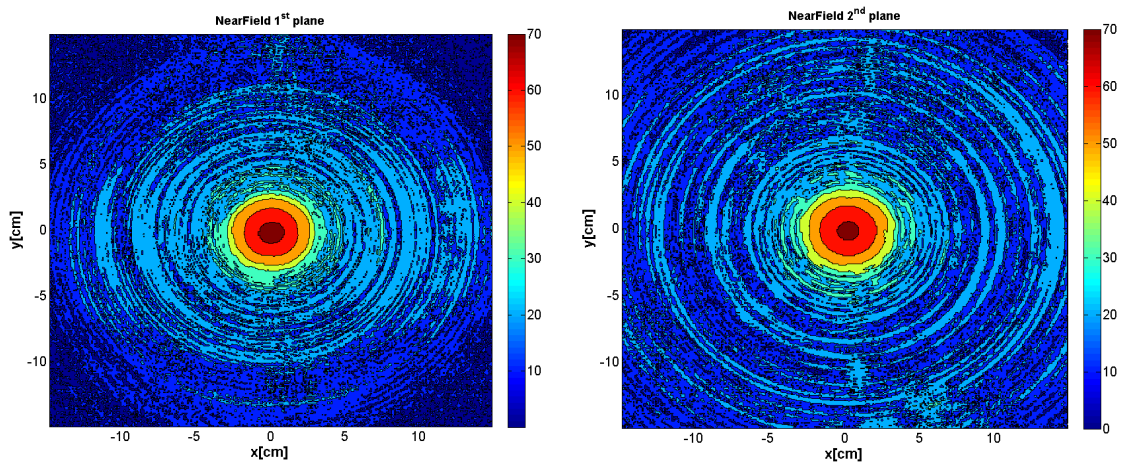
Fig. 3.10 Near-field amplitude on the first and second scanning plane

The contour plots of the near-field directly measured by the probe at frequency 310 GHz are depicted in Fig. 3.10 and far-field radiation patterns obtained by direct transformation of the measured complex near-field are shown in Figure 3.11 and 3.12.
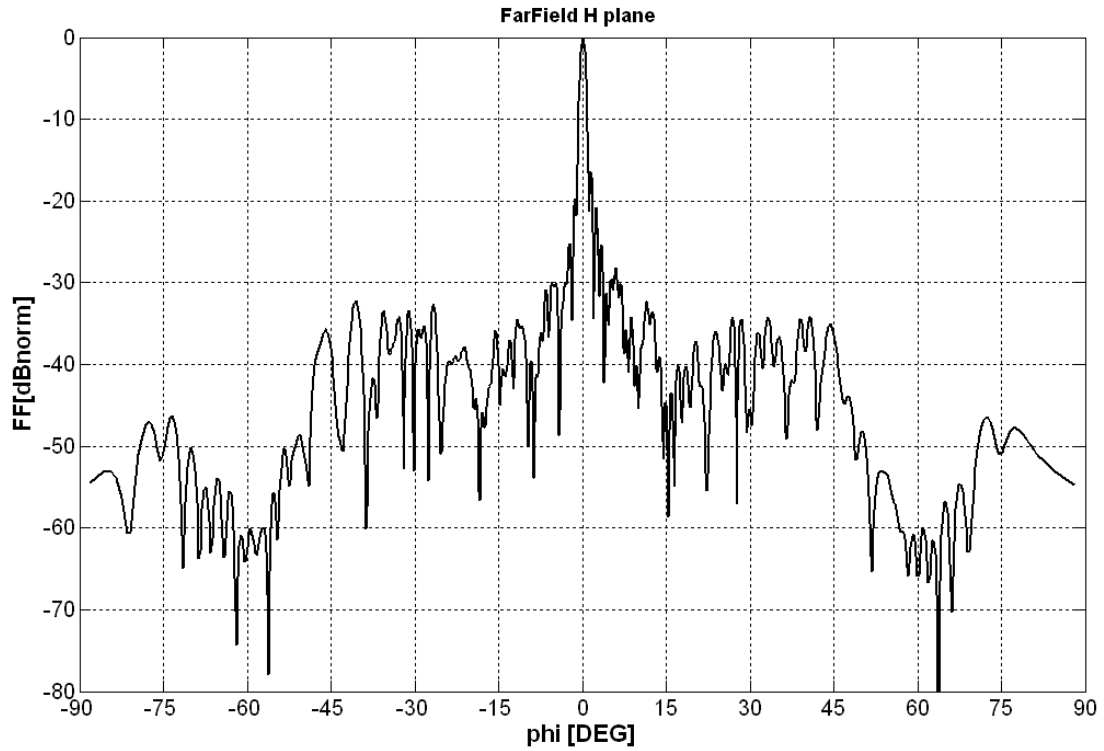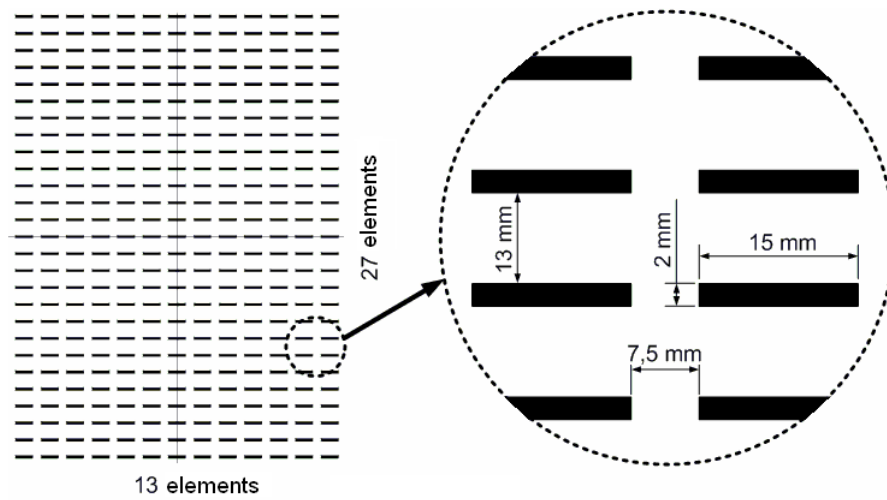

Fig. 3.11 Far-field of the lens antenna obtained by direct transformation of the measured complex near-field; H plane
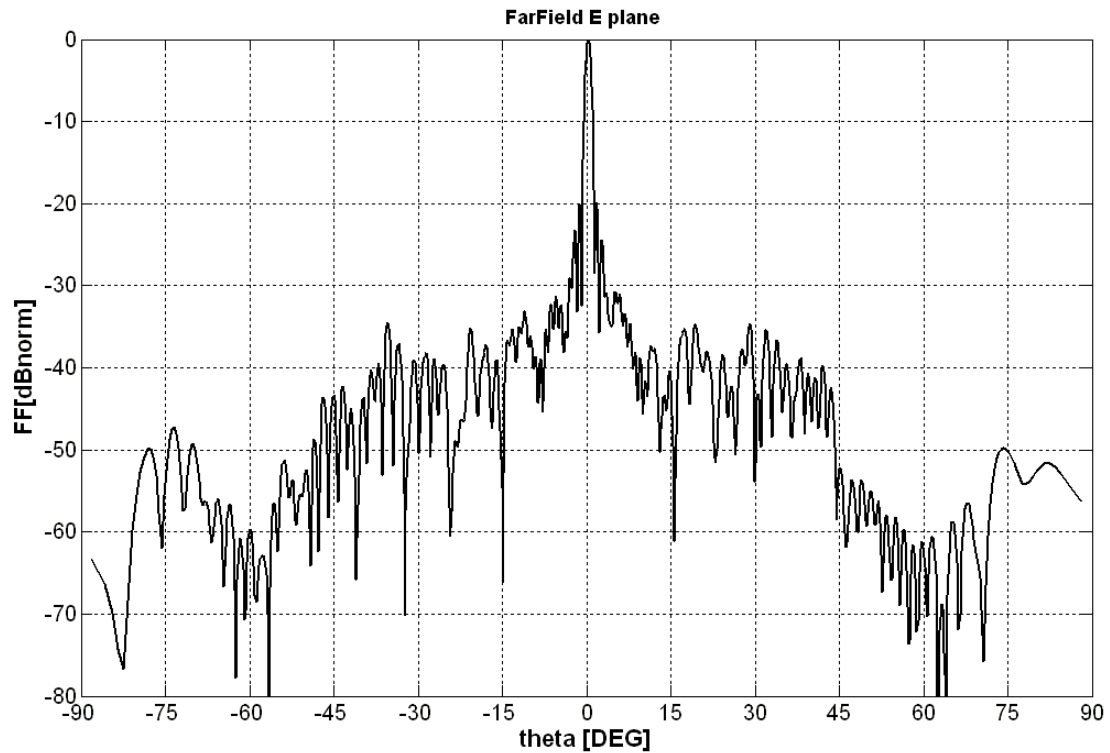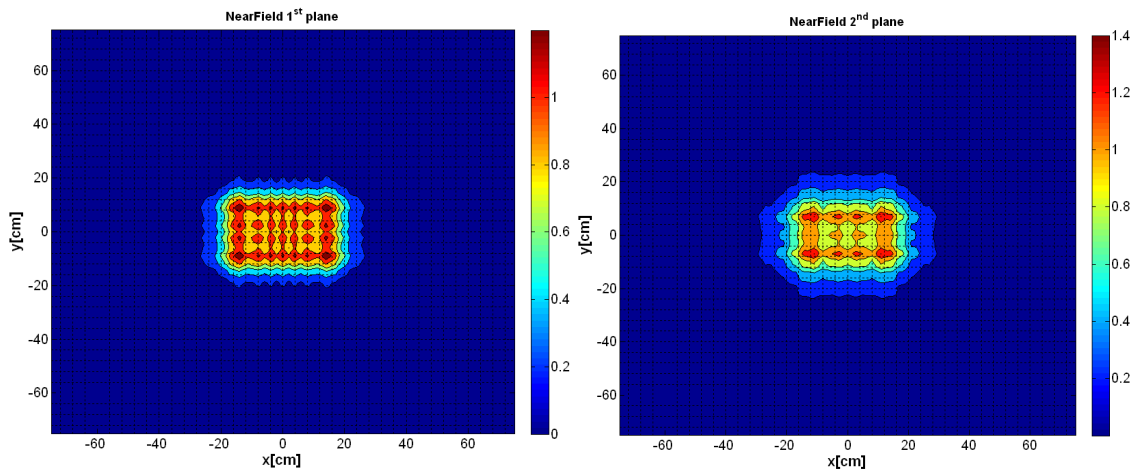

Fig. 3.12 Far-field of the lens antenna obtained by direct transformation of the measured complex near-field; E plane

The antenna array

The synthesized data were used for the radiation pattern reconstruction of the antenna array (13×27 elements) at 10 GHz [51]. Elements of antenna array were fed by unit electric current and in phase to get the radiation maximum in direction orthogonal to the antenna plane. Elements of dipole arrays were situated according the raster, see Fig. 3.13. The values of the horizontal electric field intensity component in discrete points were synthesized. The points were placed in the vertical and horizontal direction with the pitch of 10 mm (0.33λ) at two scanning planes of the size 1500×1500 mm with 22 801 (151×151) values on each plane. The first plane was placed in the distance of 150 mm (5λ), and the second one in the distance of 300 mm (10λ). With respect to the arrangement, the valid angle is $\theta_v = 60^o$ ($|k_x/k| = |k_y/k| = 0.86$). Aperture size in sampling points is 31×41 and the solution space contains 2 542 real parameters the optimal values of which are to be found.
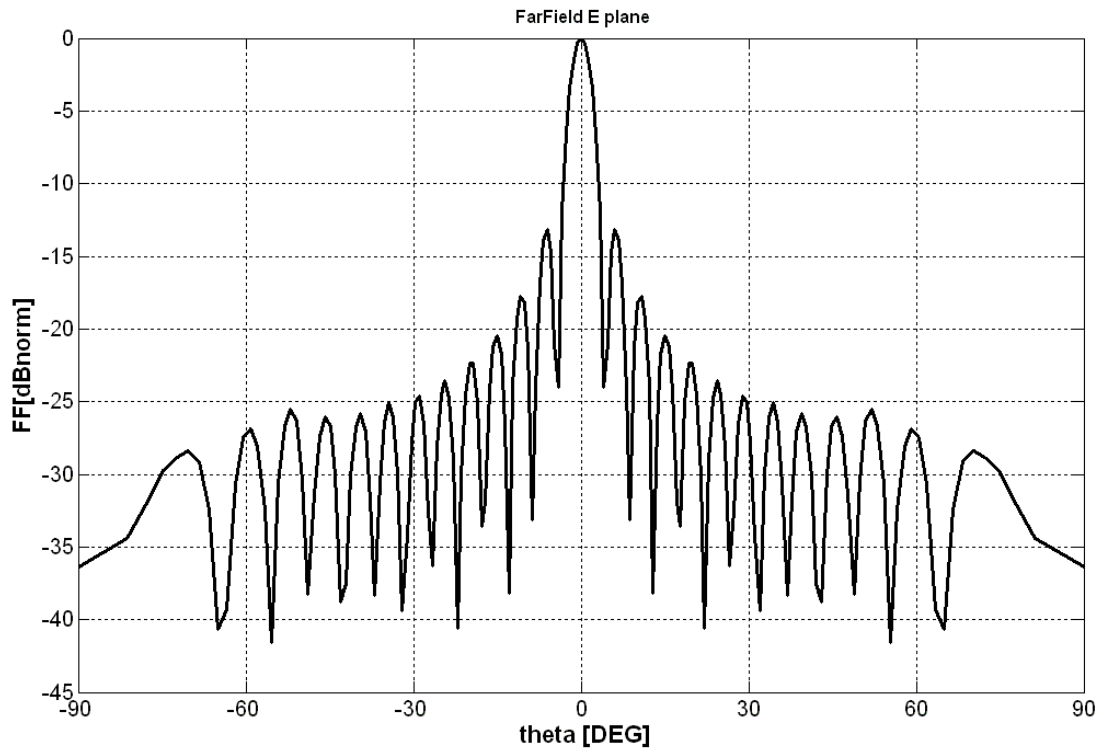

Fig. 3.13 Model of the antenna array

Fig. 3.14 Contour plot of the near-field amplitudes for both scanning planes; antenna array

The contour plots of the amplitude near-field are depicted in Fig. 3.14 for both scanning planes. The far-field radiation patterns of the antenna array obtained by direct

transformation of the synthesized complex near-field are shown in Figure 3.15 and Fig 3.16.
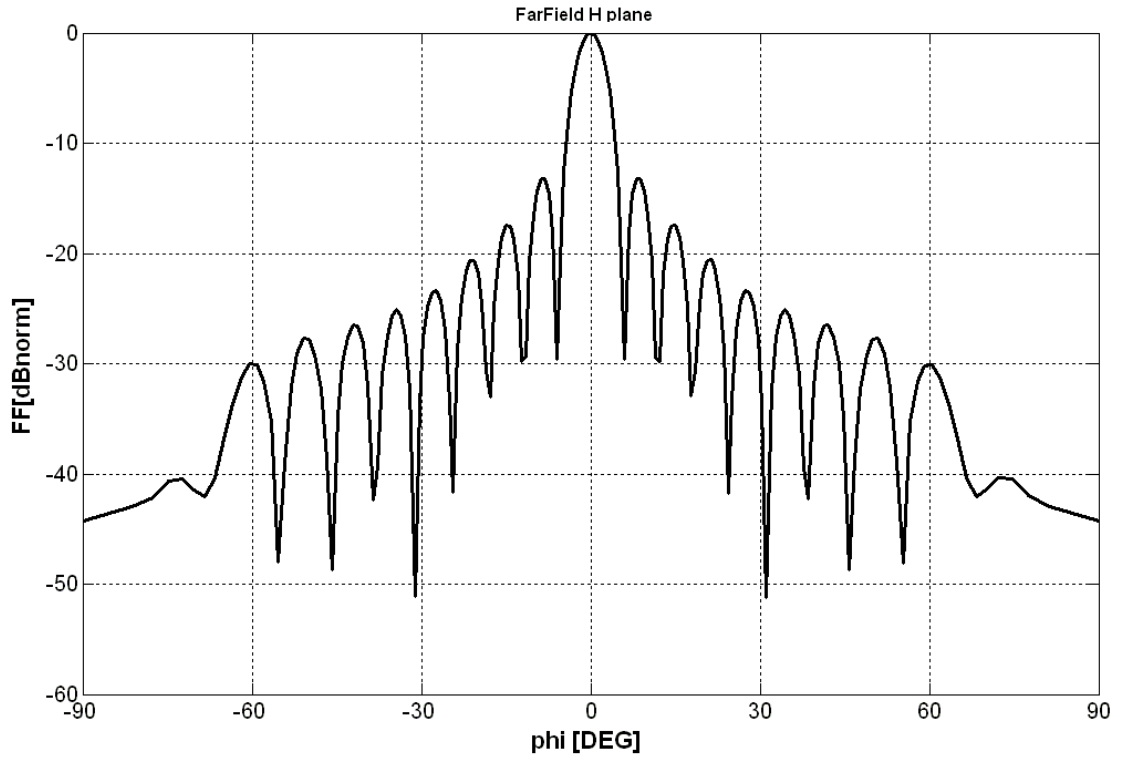
Fig. 3.15 Far-field of the antenna array obtained by direct transformation of the synthesized complex near-field; H plane

Fig. 3.16 Far-field of the antenna array obtained by direct transformation of the synthesized complex near-field; E plane

3.1.2 Comparison of the minimization approaches [63]

In this part, the comparison of two different approaches for reconstruction of radiation pattern is presented. The first classic approach is used in the contemporary minimization methods [7], [23]-[25] and the second one is a new approach based on the principle of Fourier iterative method [28], [30].

The classic approach used in the minimization methods is shown in Fig. 2.4. First, random initial estimate of the electric field distribution on the antenna aperture is performed. Zero padding is performed to get the same extension as the scanning surfaces have. After this operation, the initial electric field on the aperture is propagated by the propagation constant to the distance of the first and the second scanning plane. In the next step, the computed amplitudes are compared with the measured ones according to the fitness function (2.7), see Fig. 3.17.
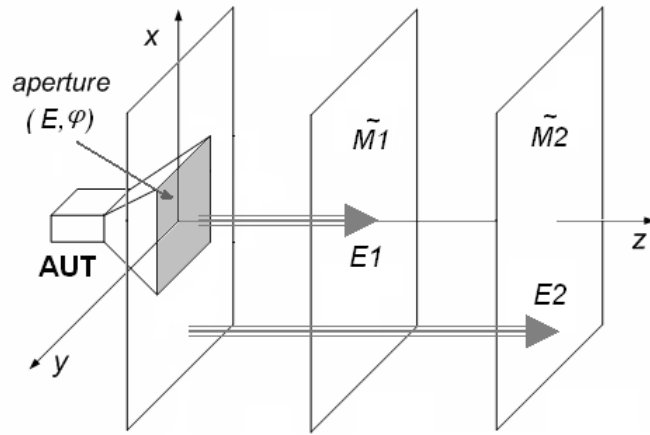
Fig. 3.17 Principle of the classic minimization approach

The second approach is based on the principle of Fourier iterative method, Fig. 3.18. Random aperture field distribution is chosen as the first initial estimate. This estimate is completed symmetrically with zeros and then it is propagated to the first plane. At this point, the calculated amplitudes of the first plane are replaced with the measured ones. The resulting field is then propagated to the next plane, and the calculated amplitudes of the second plane are again replaced with the measured ones. Field in the second plane is projected back to first plane and the error function is calculated according the same fitness function (2.7) but only for the first plane, see Fig. 3.19.
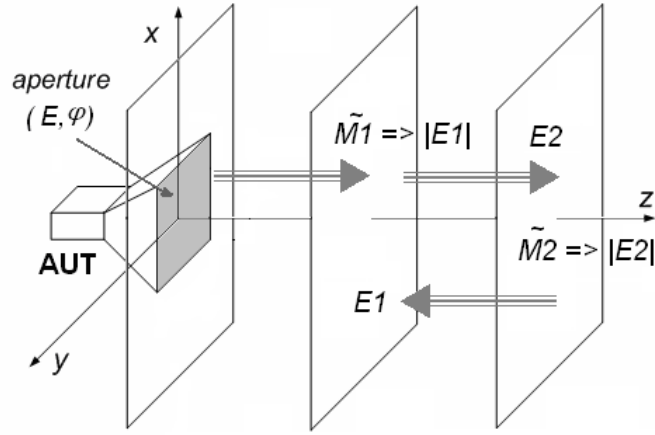
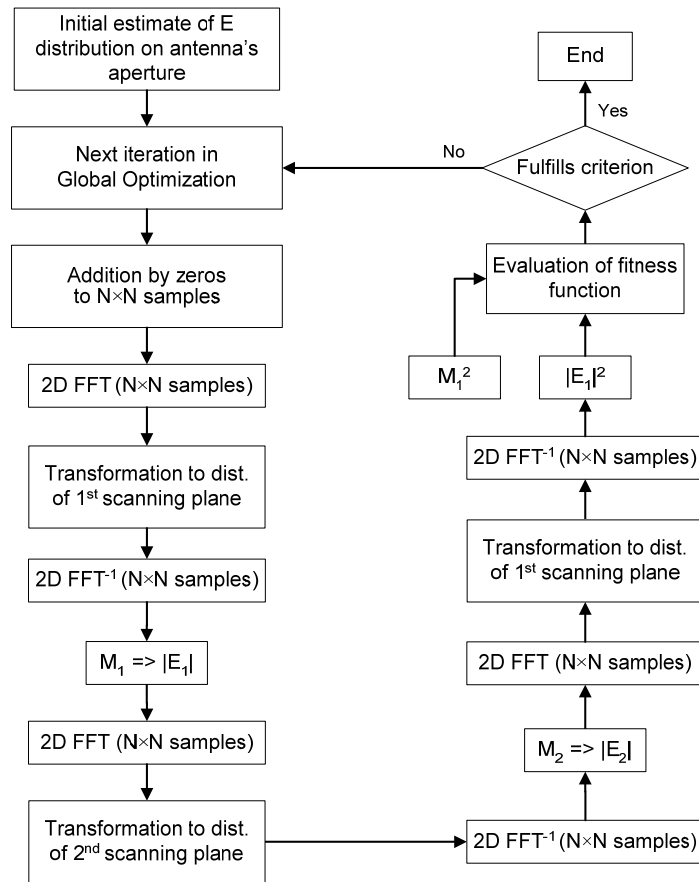**Fig. 3.18** Principle of the new minimization approach

Fig. 3.19 Flow chart of the algorithm exploiting the principle of Fourier iterative method

The comparison of minimization approaches was carried out on the radiation pattern reconstruction of the antenna array. In each case, ten repeats were performed and the optimization was stopped in the 500th iteration. The Particle Swarm Optimization (PSO) was used as a global optimization tool.

In Fig. 3.20, we can see the comparison of averaged convergence properties for both minimization approaches which were exploited in the minimization method.
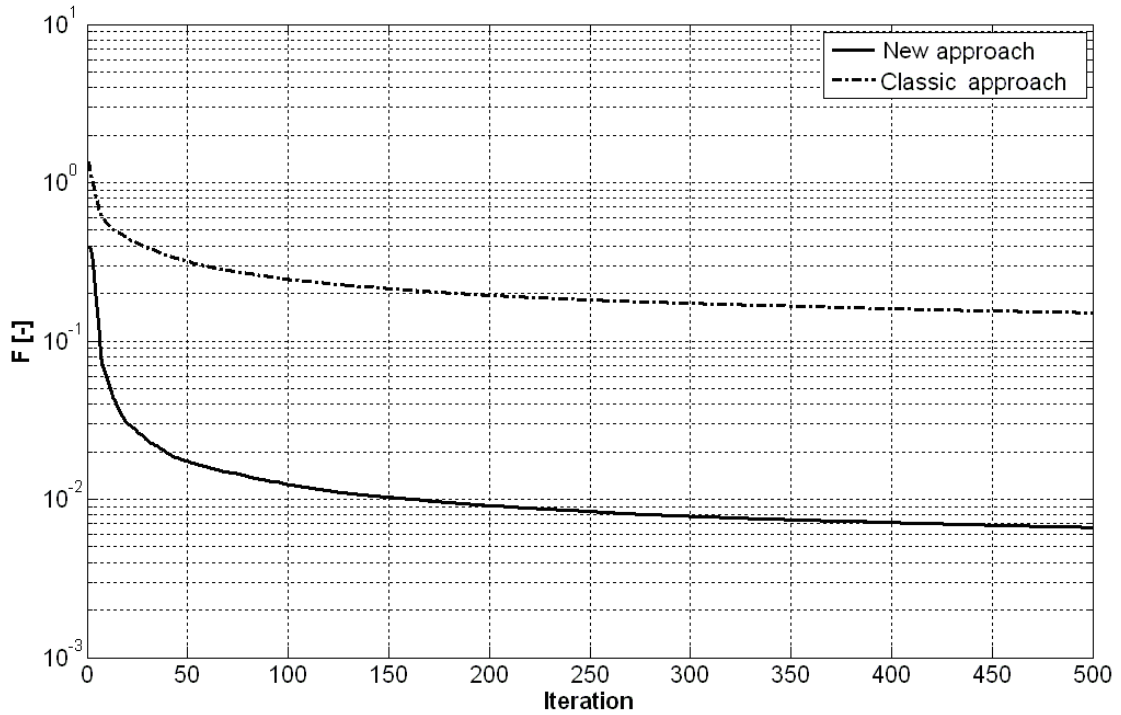
Fig. 3.20 Comparison of the convergence properties of both minimization approaches

Obviously, the algorithm using the new approach based on Fourier iterative method exhibits much better convergence properties than the classic approach. The novel approach reaches approximately twenty-three times better global minimum value than the classic one [7], [23]. The disadvantage of the new approach is that it is slightly more time-consuming compared with the classic one. As the computational costs of each optimization scheme are concerned, the classic approach saves up to 40 % of the CPU-time. Despite to it, new approach is able to obtain the same value of fitness function eighty times faster. Thus, the ratio fitness function F/Iteration is also in favor of new approach.

3.1.3 Application of the global optimization techniques to functional minimizing

Global optimization techniques are very useful in electromagnetic issues, when searching for the global maximum (minimum) in a multidimensional domain. In contrast to the local minimization, the use of the global algorithm is not conditioned by any choice of the initial estimate and an additional modification of the minimized functional. On the other hand, the convergence can slow down. The aim is to find the global approach that is able to find the area of the global minimum as efficiently as possible. To this end, most contemporary global optimizations were designed. Their advantages and disadvantages are investigated and reported in the following sections.

3.1.4.1 Global optimizations: PSO, DEA, BGA and RVGA

Four global optimizations were chosen for the functional minimization: the binary genetic algorithm (BGA), the real-valued genetic algorithm (RVGA), the particle swarm optimization (PSO) and the differential evolutionary algorithm (DEA).

Particle Swarm Optimization (PSO)

The PSO algorithm emerges as a powerful stochastic optimization method inspired by the social behavior of organisms such as bird flocking or fish schooling, in which individuals have memory and cooperate to move towards a region containing the global or a near-optimal solution [38], [39]. The particle swarm optimization algorithm was first described in 1995 by James Kennedy and Russell C. Eberhart.
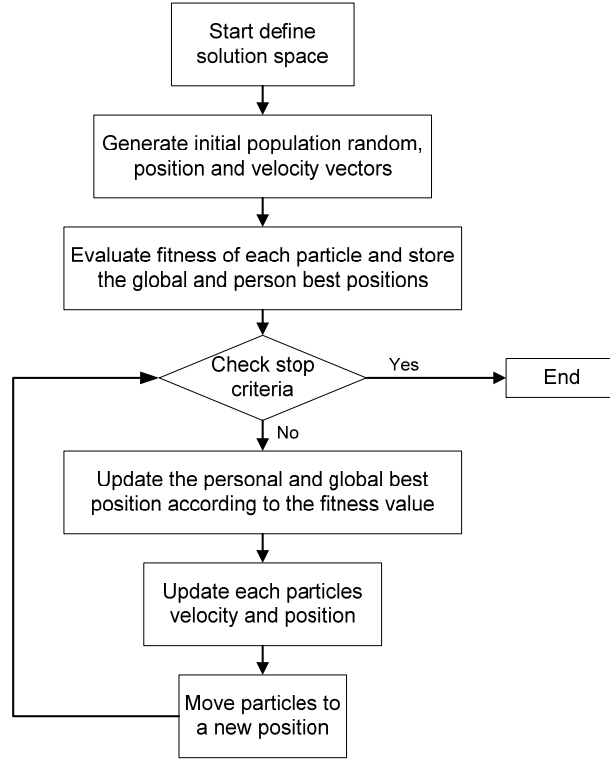
Fig. 3.21 Particle swarm optimization algorithm

The PSO is exploited to solve a multi-dimensional discontinuous problem and to search solution space limited from $-\pi$ to $+\pi$ for phases and from zero to an existing maximal value on the first sampling plane for amplitudes.

PSO is initialized with a group of random particles (solutions) and then searches for optima by updating generations. In each iteration, each particle is updated by following two "best" values. The first one is the best solution it has achieved so far. This value is called p_{best}. Another "best" value which is tracked by the particle swarm optimizer is the best value obtained so far by any particle in the population. This best value is a global best called g_{best}. After finding the two best values, the particle updates its velocity and positions with following equations [38]:

$$\mathbf{v}_n = K \left[\mathbf{v}_n + \varphi_1\, rand()\left(\mathbf{p}_n - \mathbf{x}_n\right) + \varphi_2\, rand()\left(\mathbf{g}_n - \mathbf{x}_n\right) \right],$$
(3.1)

$$\mathbf{x}_n = \mathbf{x}_n + \Delta t\, \mathbf{v}_n.$$
(3.2)

Here, $\mathbf{v}_n$ is the velocity vector of the nth agent, x_n denotes the position of the nth agent, $\mathbf{p}_n$ is the position of the personal optimum of the nth agent, and $\mathbf{g}_n$ is the position of the

global optimum of the whole swarm. Next, *rand*( ) denotes random numbers from 0 to 1, the factor K is known as a restriction factor, φ_1 and φ_2 are the acceleration constants.

PSO exhibits the best convergence properties if the restriction factor is chosen 0.729 and acceleration constants equal to 2.4 and 1.7, respectively [7], [48]. If a new velocity vector of the agent is known, its new position can be computed by (3.2) where Δt is a time step usually chosen to be one. Otherwise, the algorithm shows the best properties when absorbing walls were chosen as the border condition, and the swarm consisted of 30 agents [53].

Differential Evolutionary Algorithm (DEA)

The DEA is a new heuristic approach which works with real numbers as RVGA does [43]. The DEA is a population based algorithm like genetic algorithms using the similar operators; crossover, mutation and selection. The main difference is that genetic algorithms rely on crossover while DEA relies on mutation operation [40], [41].

The DEA is a parallel direct search method which utilizes Np (number of the individuals in population) D-dimensional parameter vectors $\mathbf{p}_{i,G}$, $i = 1, 2, 3, \ldots,$ Np as a population for each generation G. DEA generates new parameter vectors by adding the weighted difference between two population vectors to a third vector (3.4). This operation is called mutation. The parameters of the mutated vector are then mixed with the parameters of another predetermined vector, the target vector, to yield the so-called trial vector. Parameter mixing is often referred to as "crossover".

The DEA used for the phase reconstruction is described in the block diagram shown in Fig. 3.22. First, the parent population uniformly distributed in the parameter space is initialized. When the best parent meets the optimization criteria the process is terminated. At the beginning each iteration, the trial vectors **t** are generated or the parent becomes the child $\mathbf{c}_i$ on the base probability p_c [40]

$$c_{ji,G+1} = \begin{cases} t_{ji,G+1} & \text{if } (rand_j \leq p_c) \text{ or } j = rn_i \\ p_{ji,G} & \text{if } (rand_j > p_c) \text{ and } j \neq rn_i \end{cases} \tag{3.3}$$

where $j = 1, 2, \ldots,$ D; $rand_j \in |0,1|$ is the random number; p_c is crossover constant $\in |0,1|$ and $rn_i \in (1,2,\ldots,\mathrm{D})$ is the randomly chosen index. For each parent vector $\mathbf{p}_{i,G}$, $i = 1, 2, 3, \ldots,$ Np, the trial vector is generated according to [40]

$$\mathrm{t}_{i,G+1} = \mathbf{p}_{r1,G} + F \cdot (\mathbf{p}_{r2,G} - \mathbf{p}_{r3,G}), \tag{3.4}$$

where $i, r1, r2, r3 \in \{1, 2, \ldots, Np\}$ are randomly chosen and must be different from each other. In (3.4), F is the scaling factor $\in (0, 2)$. The parent vector is mixed with the mutated vector to produce a trial vector $t_{ji,G+1}$ [40]. If the trial vector yields a lower cost function value than the target vector, the trial vector replaces the target vector in the following generation. This operation is called selection. Finally, the winner x is mutated with a small probability p_m to become the child.

The parameters of the DEA used for evaluating new member were chosen similar to those used in [41]. Thus, for our specific case, we have used these parameters: the

probability of the mutation in mutant vector $p_m = 0.1$, the crossover rate $p_c = 0.9$ and the scaling factor $F = rand$. In [41], the scaling factor was set on value 1.2 but we were not able to find the global minimum area in this case. The number of population Np was chosen 24.
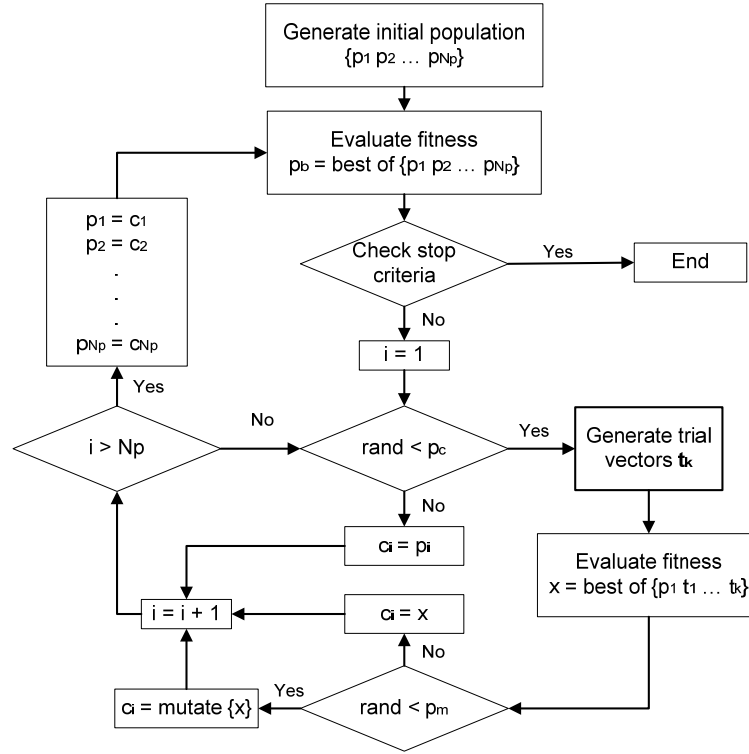

Fig. 3.22 Flow chart of the DEA using for reconstruction of the antenna radiation pattern

Binary Genetic Algorithm (BGA)

Genetic Algorithm (GA) is a stochastic search method widely used in electromagnetism to find the global minimum in a multidimensional domain. By analogy with natural selection and evolution, the set of parameters (genes) to be optimized defines an individual (chromosome). The set of individuals forms the population, which is evolved by means of the selection, the crossover, and the mutation genetic operators [42]. In this part, the classic binary encoding BGA scheme is investigated and implemented [42], [43].

The optimization strategy was selected according to the results of a preliminary parametric study [48], [49], [55] as follows. Thirty individuals were chosen to form a population. Each individual (chromosome) consisted of binary genes by 8 bits. The elitist strategy was taken into account. Thus, the half best individuals were propagated unchanged. The tournament was used for selecting parents. Parents were obtained by two rounds selection and were sorted by fitness function. Parents were selected to make 14 new offspring by the uniform crossover and the five new offspring were created by the mutation of the remained parents. 15 best offspring from this group completed the elitist. The probability of crossover was set to $p_c = 70$ %, and the probability of mutation to $p_m = 25$ %. The optimization scheme is depicted in Fig. 3.23.
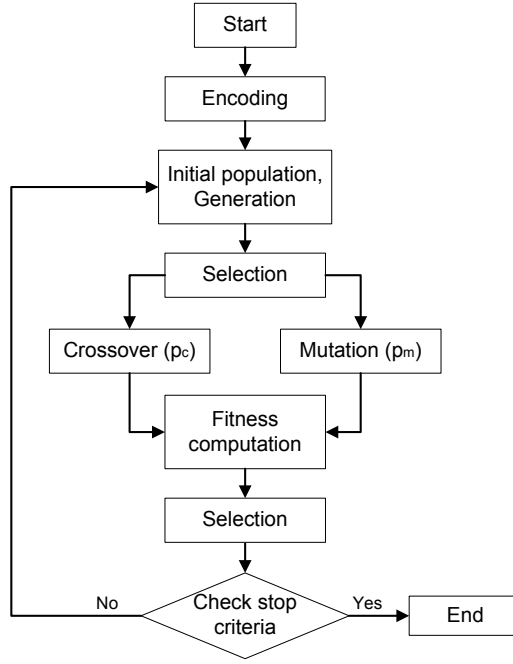
Fig. 3.23 Binary genetic algorithm

Real-Valued Genetic Algorithm (RVGA)

In the case of RVGA, the number of bits required to accurately encode a parameter does not need to be considered. Instead, the amplitudes and phases are encoded in terms of real numbers in between the given bounds.

For the proposed problem, the influence of the selection and crossover strategies and the influence of the population size on the accuracy of results were investigated in [50]. The tournament selection and the linear crossover were chosen and the population size of 24 individuals was chosen as optimum. For the analyses, two strategies were designed and combined:

- The crossing strategy: 20 parents were chosen by the tournament selection to make 60 offspring by the linear crossover and 2 offspring were created by the mutation of 2 random parents. 20 best individuals sorted by fitness function completed 4 elitist individuals.

- The mutation strategy: 4 parents were chosen by the tournament selection to make 12 offspring by the linear crossover and 20 offspring were created by the mutation of 20 random parents. 20 best individuals sorted by fitness function completed 4 elitist individuals.

In both cases, the probability of the crossover was set to $p_c = 100$ %, and the probability of the mutation to $p_m = 25$ %. The change in strategy occurs when the crossing strategy stagnates. Further, the formulas of the linear crossover from [43] were generalized to the form:

$$p_{new1} = b.p_{mn} + b.p_{dn}$$

$$p_{new2} = (b+1).p_{mn} - b.p_{dn}$$

$$p_{new3} = -b.p_{mn} + (1+b).p_{dn} \,.$$

<div align="right">(3.5a, 3.5b, 3.5c)</div>

Where p_{mn} is the nth parameter in the mother chromosome and p_{dn} is the nth parameter in the father chromosome. The constant b was chosen randomly or was set on the value 0.5 depending on the strategy chosen. For crossing strategy, b is random, and for mutation strategy, it is set to 0.5. Any parameter outside the bounds is replaced by the random number.

In short, the PSO, RVGA and DEA algorithms require fewer lines of code than BGA and are easier to implement. Moreover, PSO and DEA have a small number of the parameters to be tuned compared with GAs. In PSO, population size, restriction factor and acceleration constants, and in DEA, number of population, scaling factor and crossover rate summarize the parameters to be selected and tuned, whereas in GAs population size, selection, crossover and mutation strategies, as well as crossover and mutation rates influence the results.

3.1.4.2 Comparison of GO techniques [56]

In this section, the comparison of the global optimization techniques is presented. Their comparison was carried out on the radiation pattern reconstruction of the horn antenna and dish antenna. The difference between these reconstructions was in the number of the variables. In case of the horn antenna, we found out 390 variables whereas in case of the dish antenna, it was about 7400 variables. Classic optimization approach was used.

The configuration of the optimization schemes considered in the analysis is summarized in Table 3.1 and was selected according to the results of a preliminary parametric study carried out individually with each algorithm [7], [30], [48]-[50]. All optimizations minimize the same functional (2.7). Each optimization was repeated 10 times and was stopped in the 5000th iteration. The averaged realizations are shown in Fig. 3.24 for the horn antenna and in Fig. 3.26 for the dish antenna.

**Table 3.1.** Settings of the optimization algorithms

Optimization algorithm	Parameters
Real-Valued GA	Tournament selection; linear crossover $P_C = 1$; random mutation $P_m = 0.25$; elitism; PS = 24
Binary GA	Tournament selection; uniform crossover $P_C = 0.7$; random mutation $P_m = 0.25$; elitism; PS = 30; 8 bits to encode
PSO	Constant inertia: K =0.729, $\varphi_1 = 1.4$, $\varphi_2 = 2.4$; absorb wall; PS = 30
DEA	$p_m = 0.1$; $CR = 0.9$; $F = 1.2$; PS = 24

As Fig. 3.24 shows (390 parameters were optimized), the convergence of the DEA is less steep compared with the others. All optimizations reach approximately similar global minimum values except DEA after 5000 iteration steps, while the RVGA achieves the best possible result. For the DEA, the fitness function does not reach such global minimum value as other optimizations reach and begins to stagnate from about 200 iteration steps. In case of GAs, the fitness functions still fall slowly down in

contrast to PSO where the fitness function almost stagnates from about 2000 iteration steps, and is already without any significantly change.
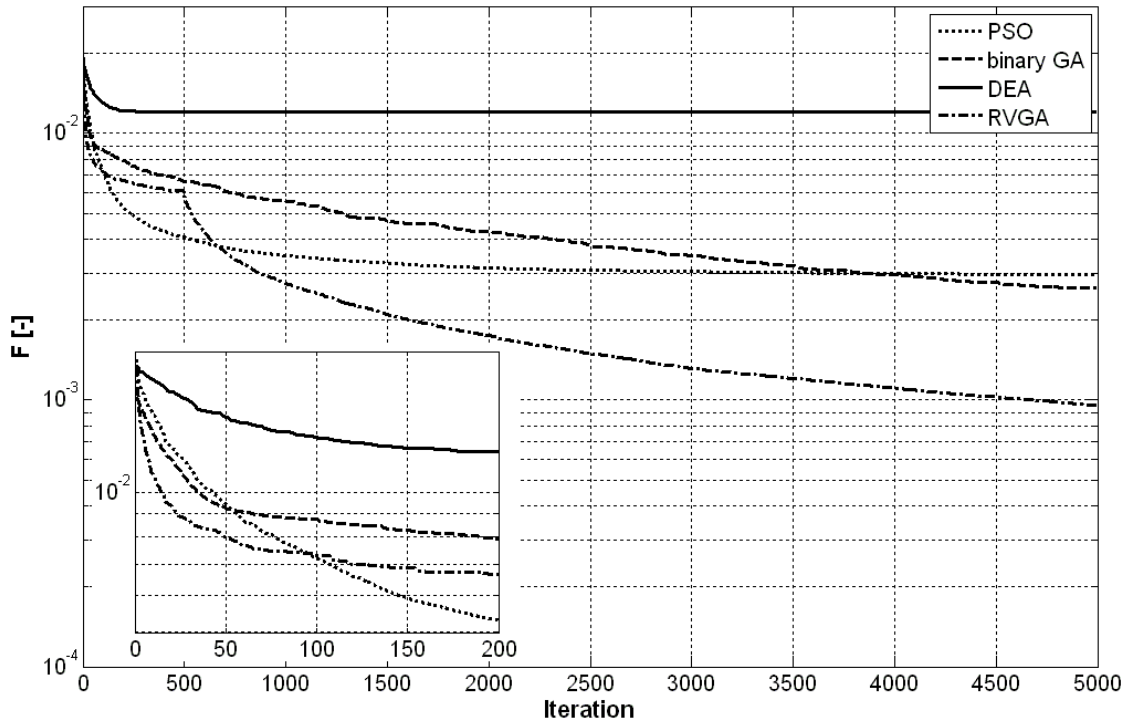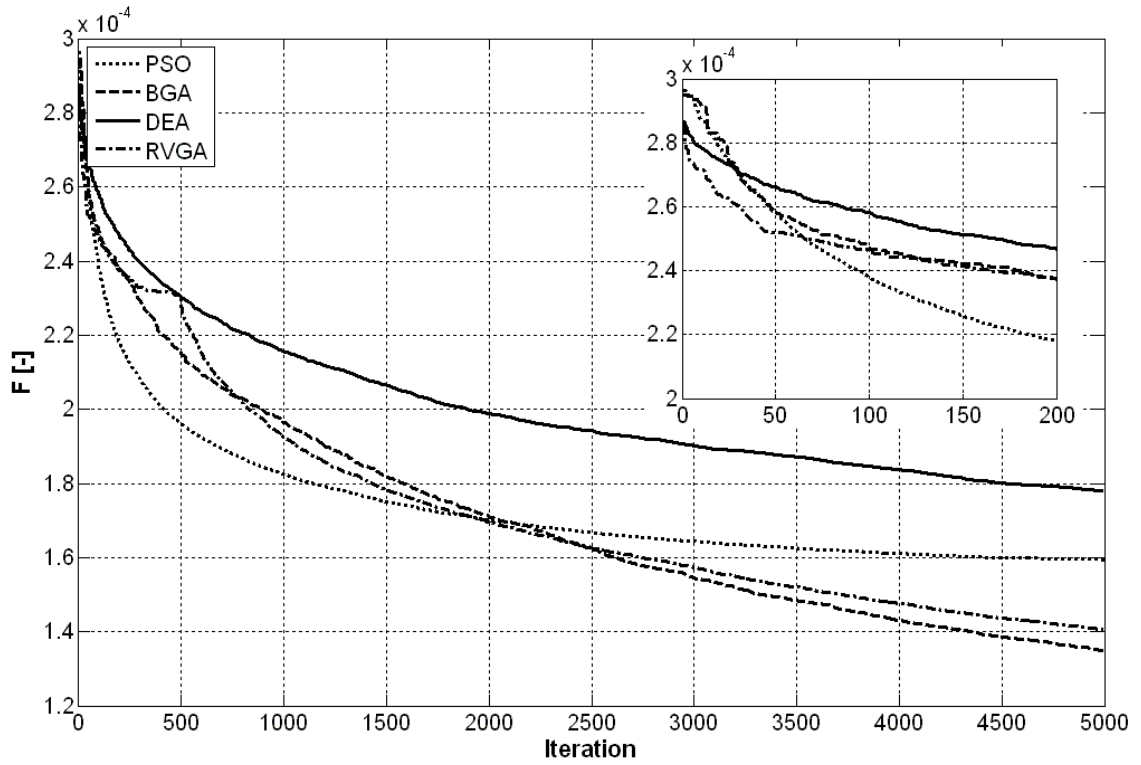

Fig. 3.24 The horn antenna; convergence behavior of the optimization algorithms
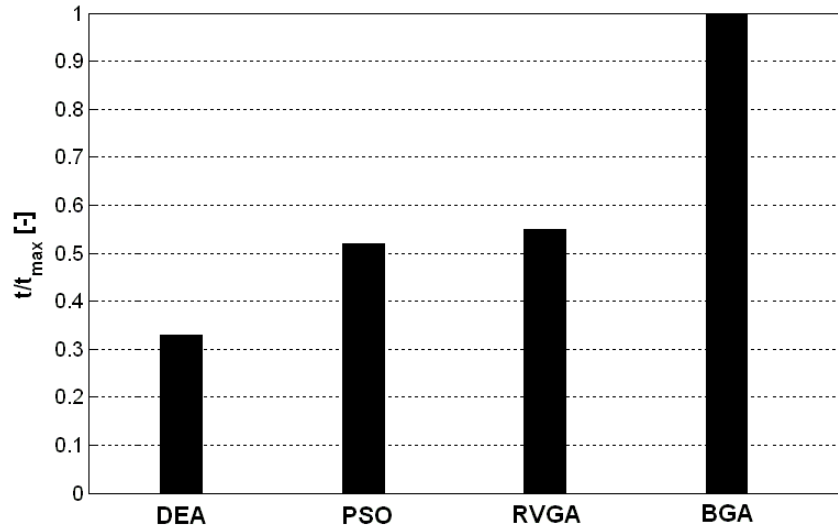
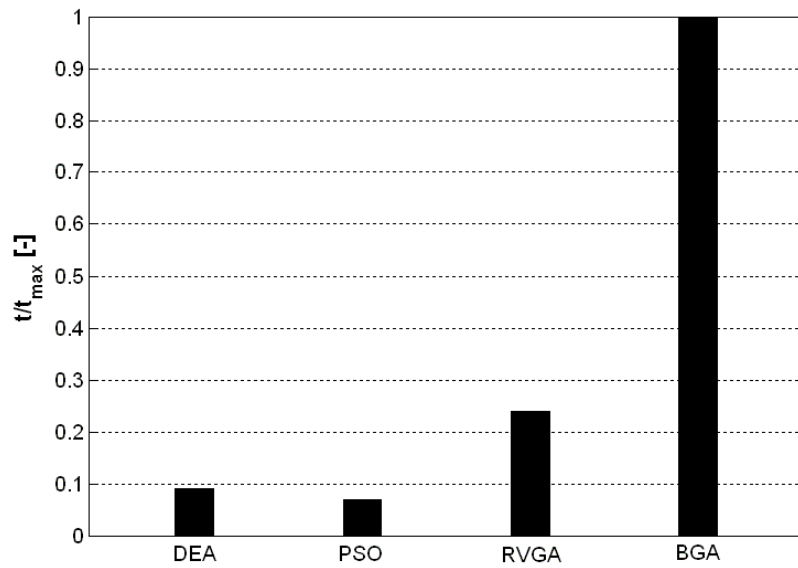**Fig. 3.25** Comparison of the computational efforts for horn antenna; averaged results for 10 independent runs carried out with each method

As Fig. 3.26 clearly shows (7 400 parameters were optimized), the GAs have the best convergence properties; on the other hand, the DEA has the worst one. It should be noted that neither of the optimization techniques stagnates after the 5000 iteration.

Fig. 3.26 The dish antenna; convergence behavior of the optimization algorithms

Fig. 3.27 Comparison of the computational efforts for dish antenna; averaged results for 10 independent runs carried out with each method

The real-valued genetic algorithm (RVGA) converges very quickly to the solution in the initial phase in both cases and then begins to stagnate. In this phase, stagnating crossing strategy is replaced by mutation strategy and the algorithm converges very quickly again. Only PSO exhibits a better behavior than RVGA in the initial phase but PSO is then overcome in the next phase of the minimizing process by other GAs.

Concerning the computational costs of each optimization scheme, Fig. 3.25 and 3.27 show the average CPU-time required by each method. Results demonstrate the

superiority of PSO, RVGA and DEA, which saves up to 50% of the CPU-time compared to BGA in the cases when we optimized less variables and 90% in the cases of larger number of optimized variables. With an increasing number of variables, the demand on the CPU-time increases especially for GAs.

In conclusion to global optimization techniques, the real-valued genetic algorithm has the best convergence properties, but if the optimization problem comprises more than one thousand of unknowns, CPU-time demands of the whole minimizing process are enormous compared to PSO. Therefore, RVGA is suitable for minimizing a small number of unknown variables (less than one thousand) and using PSO is appropriate for a large number of optimized variables particularly due to low CPU-time demands.

3.1.4 Choice of the functional [57]

Fitness function (functional) and its evaluation is usually time and computationally demanding operation in the minimization process, and therefore it is necessary to pay great attention to its appropriate choice. Since the global optimization technique is exploited for minimization of the functional, any form of the fitness function can be used. In this case, we do not need to worry that algorithm gets stuck in a local minimum. The algorithm minimizing functionals employed Real-Valued Genetic Algorithm (RVGA) and classic optimization approach was used.

The chosen fitness functions, comparison of which was carried out on the radiation pattern reconstruction of the horn antenna, are of the following form:

$$F = \sum_{i=1}^{N} \sum_{j=1}^{N} \left[\left| E_1(i,j) \right|^2 - \widetilde{M}_1(i,j)^2 \right]^2 + \sum_{i=1}^{N} \sum_{j=1}^{N} \left[\left| E_2(i,j) \right|^2 - \widetilde{M}_2(i,j)^2 \right]^2 \tag{3.6}$$

$$F = \sum_{i=1}^{N} \sum_{j=1}^{N} \left[\left| E_1(i,j) \right|^2 - \widetilde{M}_1(i,j)^2 \right]^2 \cdot \widetilde{M}_1(i,j) + \sum_{i=1}^{N} \sum_{j=1}^{N} \left[\left| E_2(i,j) \right|^2 - \widetilde{M}_2(i,j)^2 \right]^2 \cdot \widetilde{M}_2(i,j)$$

$$\tag{3.7}$$

$$F = \sum_{i=1}^{N} \sum_{j=1}^{N} \frac{\left[\left| E_1(i,j) \right|^2 - \widetilde{M}_1(i,j)^2 \right]^2}{\widetilde{M}_1(i,j)^2} + \sum_{i=1}^{N} \sum_{j=1}^{N} \frac{\left[\left| E_2(i,j) \right|^2 - \widetilde{M}_2(i,j)^2 \right]^2}{\widetilde{M}_2(i,j)^2} \tag{3.8}$$

$$F = \sum_{i=1}^{N} \sum_{j=1}^{N} \left[\left| E_1(i,j) \right| - \widetilde{M}_1(i,j) \right]^2 + \sum_{i=1}^{N} \sum_{j=1}^{N} \left[\left| E_2(i,j) \right| - \widetilde{M}_2(i,j) \right]^2 \tag{3.9}$$

In formulas, $E_1(i,j)$ and $E_2(i,j)$ are the computed complex electric field values in the point i, j on the first scanning surface and the second one, respectively. $\widetilde{M}_1(i,j)$ and $\widetilde{M}_2(i,j)$ are the measured amplitudes in the point i, j on the first scanning surface and the second one, respectively. The functional (3.6) is adjusted so that it does not get stuck in the local minima [23]. The functional (3.7) is my modification of (3.6). The functional (3.8) was used in [25] for obtaining more precise results. The functional (3.9) is used in Fourier iterative scheme [28]. The comparison of the averaged realizations of the normalized fitness functions is shown in Fig. 3.28.
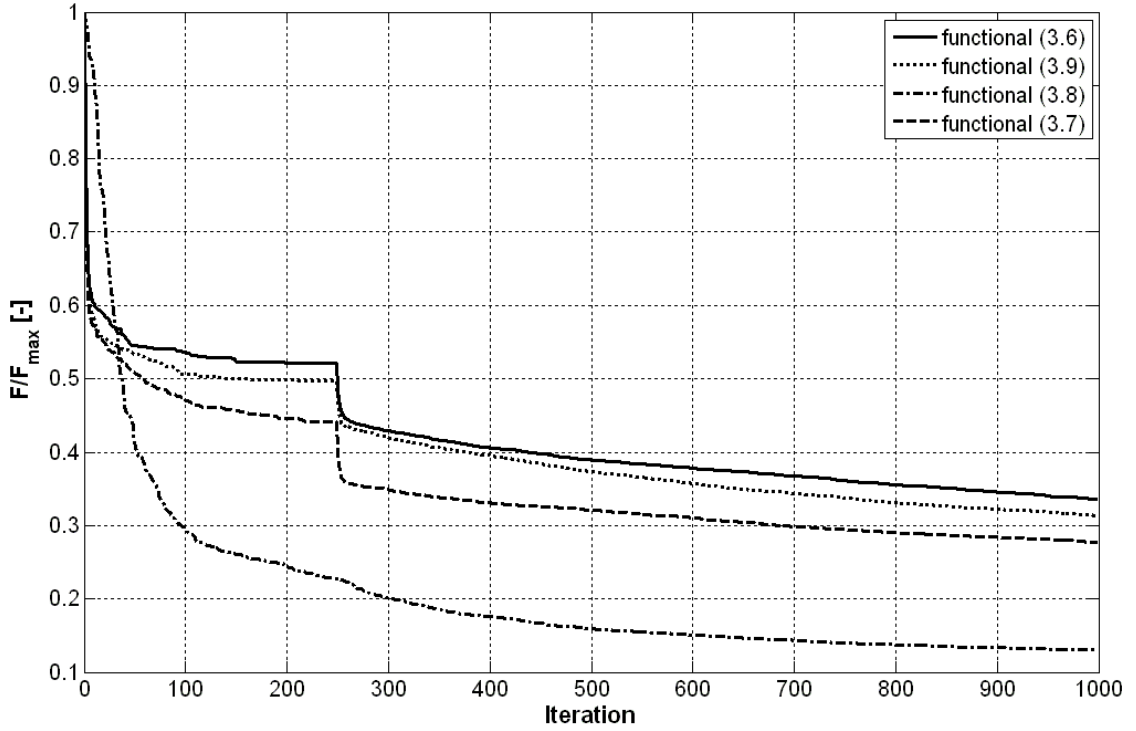
Fig. 3.28 Convergence of the different functionals; averaged results for 10 independent runs

Obviously, the fitness function (3.8) exhibits the fastest convergence compared to the others which exhibit comparable properties. But numerical analysis showed that the functional (3.8) caused problems with finding the global minimum area. That is why the functional (3.8) has to be combined with another one. It turns out that the best solution strategy is to consider first fitness function (3.6), (3.7), (3.9) from a completely random first guess of the near field distribution and then to switch to fitness function (3.8) starting from the obtained current estimate of the solution [57]. The combination of the fitness function (3.7) and (3.8) for reconstruction of the radiation patterns is discussed in Chapter 3.2.2.

The final result exhibits a faster convergence rate and slightly more accurate reconstructions compared to using only pure functional (3.6), (3.7) or (3.9) but reconstructed far-field radiation patterns still do not achieve accurate results, and another algorithm (local method, iterative algorithm) has to be applied to ensure the required precision of the radiation patterns. Under these circumstances and since functional (3.7) exhibits the second best convergence properties, it was chosen in the designed minimization algorithm

3.1.5 Choice of the initial estimate for acceleration of GO convergence speed

When hundreds and thousands of variables have to be optimized, the convergence speed of the global optimization is slow and time consuming. For this reason the section is focused on possibilities to speed up the convergence process [49], [54] and [63].

The optimization process has always begun from the random initial estimate of the electric field distribution on the antenna aperture [7]. So there is a possibility for

acceleration of global optimization speed by choosing the appropriate initial estimate. Table 3.2 summarizes the possibilities which were considered.

**Table 3.2** Initial estimates considered for acceleration of GO

aperture amplitude	aperture phase
the complex aperture field is optimized by GO	
random: max (max (M1)) * rand ( )	random: - π + 2π * rand ( )
	uniform: - π + k * (2π / number pop.); k = 1 … number pop.
uniform: max (max (M1)) * ones ( )	random: - π + 2π * rand ( )
	uniform: - π + k * (2π / number pop.); k = 1 … number pop.
from the first scanning plane: M1 → aperture plane: aperture constraint	random: - π + 2π * rand ( )
	uniform: - π + k * (2π / number pop.); k = 1 … number pop.
only phase on the aperture is optimized by GO, the amplitude remains	
uniform: max (max (M1)) * ones ( )	random: - π + 2π * rand ( )
	uniform: - π + k * (2π / number pop.); k = 1 … number pop.
from the first scanning plane: M1 → aperture plane: aperture constraint	random: - π + 2π * rand ( )
	uniform: - π + k * (2π / number pop.); k = 1 … number pop.

All analyses were performed for the dish antenna where the situation is more critical because we have to optimize more than seven thousand variables and optimization process is very lengthy.

First, we compared the convergence properties of complete random estimate on the antenna aperture with partial one. In this case, the phase distribution was chosen uniformly and amplitude randomly. Uniform phase distribution means that the phase was assumed constant on the whole antenna aperture. The phase in the range from $-\pi$ to $+\pi$ was divided uniformly according to the number of the population (agents in the swarm). Comparison of the completely random estimate and the estimate with the uniformly selected phase distribution on the antenna aperture is shown in Fig. 3.29 which shows also the comparison of the estimates with uniform amplitude on the antenna aperture combined with random phase distribution, and uniform phase distribution, respectively. The uniform amplitude distribution was obtained by multiplication of the maximum value on the first scanning plane with unit matrix.

Contrary to expectation, the uniform amplitude distribution achieves much worse results than random amplitude distribution. Even in case of the uniform distributions, both phase and amplitude, the results are without any improvement whereas the

improvement can be noticed when the random amplitudes are combined with uniform phase distribution.
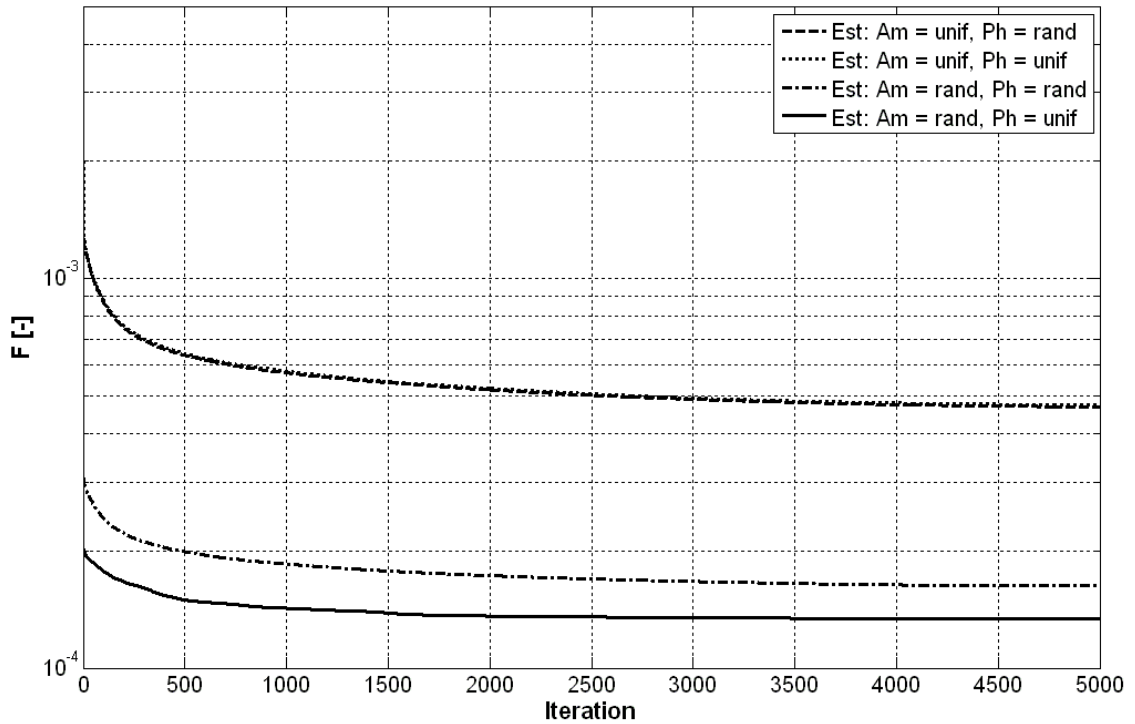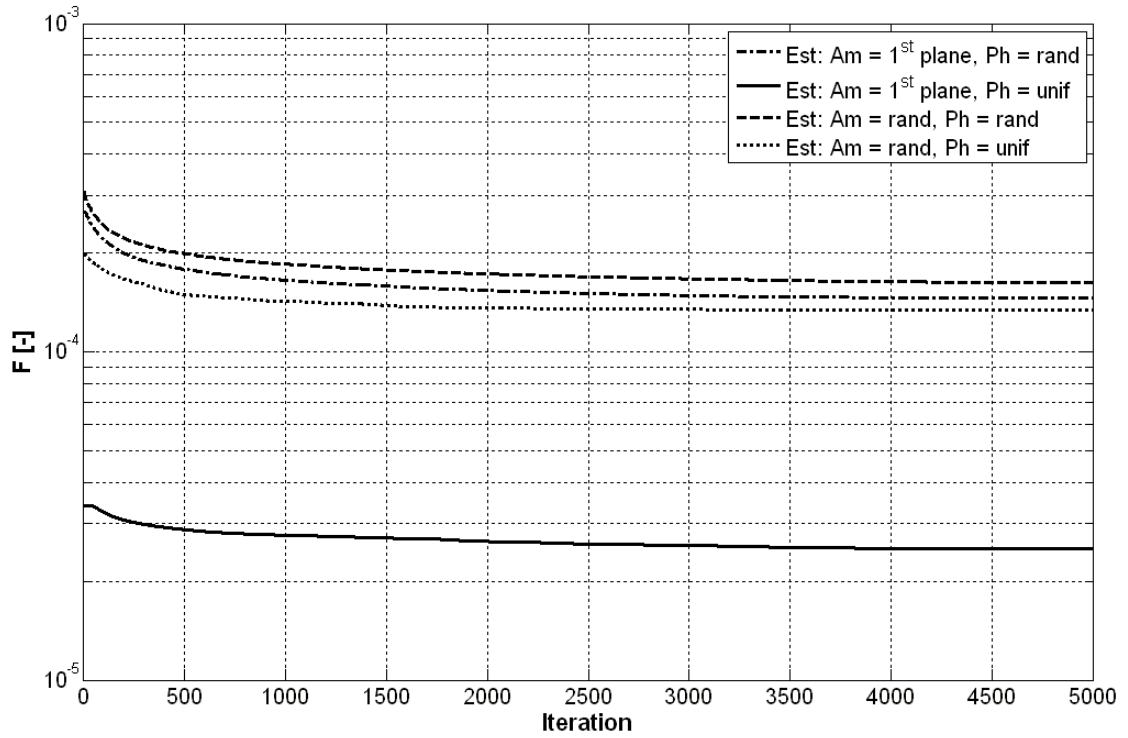

Fig. 3.29 Comparison of the convergence properties of completely random estimate with estimates which have uniformly chosen phase distribution and uniform amplitude distribution on the antenna aperture, respectively
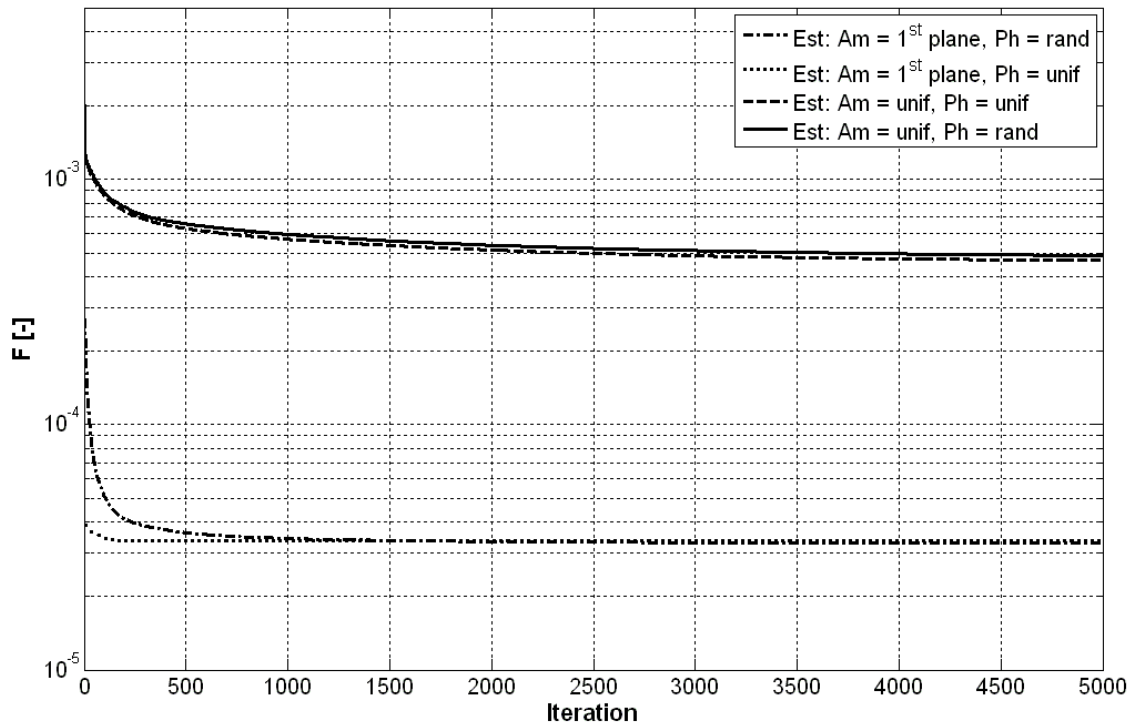
Fig. 3.30 compares the convergence properties of the completely random estimate or the partial one with estimate which has amplitude distribution obtained from the first scanning plane. It is obvious that estimate based on amplitudes from first scanning plane is the best one especially in case when we used the combination of amplitude distribution obtained from measured amplitude with uniform chosen phase distribution. Behavior of convergence curve does not change so rapidly but the fitness function reaches absolutely the best value.

Another comparison is done for using the estimate calculated from the measured amplitudes and the estimate created by uniform amplitude distribution, see Fig. 3.31. Unlike in the previous cases, only the antenna aperture phase distribution is optimized. So the number of unknowns is half and convergence speed is quicker.

As it is obvious from Fig. 3.31, the convergence curves stagnate much earlier and the fitness functions reach higher values than in cases when we optimize the complex electric field distribution on aperture. That is due to the fact that the estimate of the amplitude distribution obtained from the first scanning plane (uniform amplitude distribution) is worse than real amplitude distribution so the better results could not be obtained. Furthermore, it is clear that it does not matter if the phase distribution is chosen randomly or uniformly because the results are very similar.

Fig. 3.30 Comparison of the convergence properties of completely random estimate or partial one with estimate which have amplitude distribution obtained from the first scanning plane amplitudes

Fig. 3.31 Comparison of the convergence properties; only the phase information is optimized

In conclusion to the estimates, if we are looking for only a rough estimation lying in the area of the global minimum, it does not matter if the initial estimate is used or not in cases of small numbers of variables (less than 100) because the global optimization is

able to find it relatively very quickly. But in cases of large numbers of unknowns (more than 100), it is better to use some of the proposed estimates to achieve acceleration. The best solution is to choose the amplitude distribution obtained from the first plane and search only for the phase distribution. If it is necessary to achieve the best possible accuracy, it is better to use the estimate based on the first plane amplitude and uniform phase distribution and optimize the complex electric field distribution on antenna aperture. The possibility of using these estimates is discussed in chapter 3.2.2 for reconstruction of the antenna radiation patterns.

3.2 Design of the minimization method

On the basis of the previous analysis, the minimization algorithm was designed. Unlike [7], the new minimizing approach is exploited in minimization method. This approach based on the principle of Fourier iterative algorithm shows much better convergence properties. Due to exploitation of the global optimization, the algorithm is not conditioned by any choice of the initial estimate lying in the area of the global minimum but the convergence can slow down. From this point of view, two optimization techniques were chosen, RVGA and PSO. Which method will be used depends on the number of optimized variables. The choice of the minimizing functional is also very important. According to the analysis the fitness function was selected and has the following form (3.7):

$$F = \sum_{i=1}^{N}\sum_{j=1}^{N}\left[\left|E_1(i,j)\right|^2 - \widetilde{M}_1(i,j)^2\right]^2 \cdot \widetilde{M}_1(i,j) + \sum_{i=1}^{N}\sum_{j=1}^{N}\left[\left|E_2(i,j)\right|^2 - \widetilde{M}_2(i,j)^2\right]^2 \cdot \widetilde{M}_2(i,j)$$

The flow chart of the designed minimization algorithm is depicted in Fig. 3.32.

In the next part, designed algorithm is used for calculation of the far-field radiation patterns from retrieved phase distribution. Different reconstruction strategies are considered for this purpose.
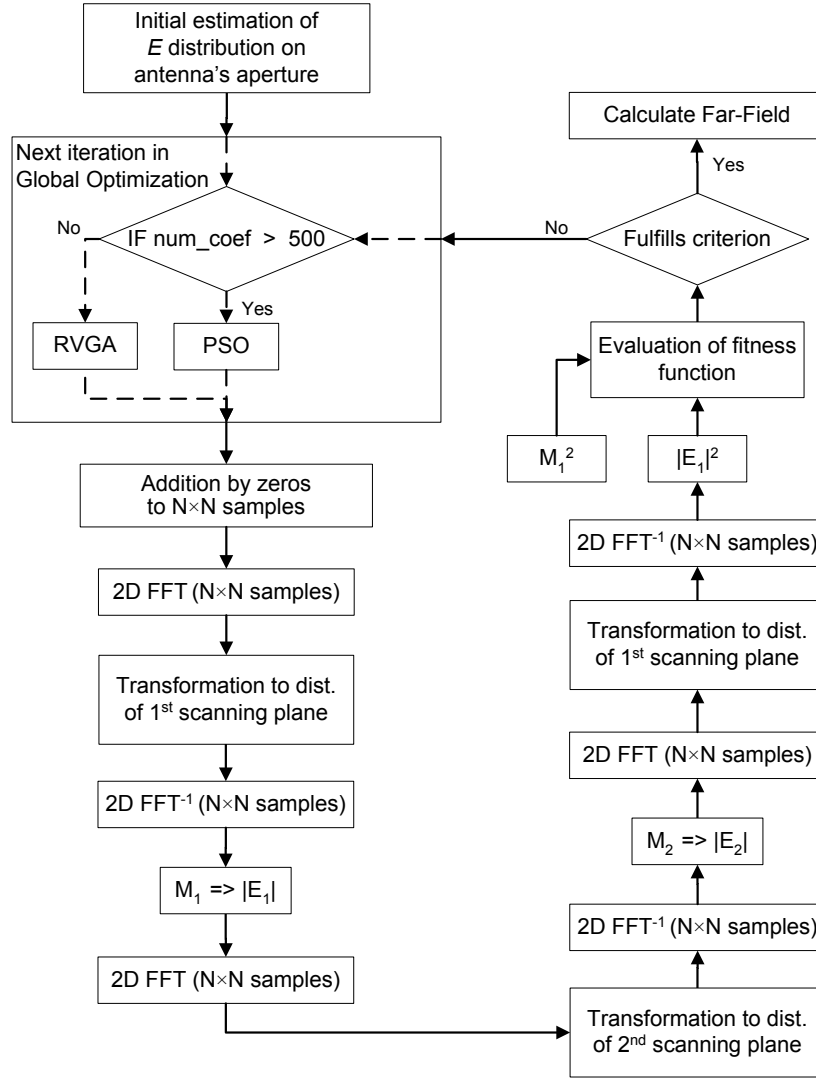
Fig. 3.32 Flow chart of the designed algorithm minimizing the functional

3.2.1 Comparison of designed minimization algorithm with others

Most current algorithms use the local methods to minimize the functional purely [23] - [26], eventually a simple iteration [28], [29]. But, they require appropriate choice of the initial estimate, or they have certain restrictions on the minimum distance between scanning planes, etc. The use of global optimization techniques to find the initial estimate is relatively new and it brings considerable simplification and acceleration of the whole minimization [7], [30]. Their implementation is very simple and takes only a few lines of the source code. Moreover, because the field distribution on the antenna aperture is minimized (not the field on some of the scanning planes), the minimization is computationally inexpensive and faster. At the same time, the use of GOs reduces the number of Fourier transformations performed to a half compared with the algorithm presented in [24]. This speeds up the whole minimization significantly again.

Fig. 3.33 compares the published minimization method exploiting PSO [7] with the designed one. Comparison is carried out for data of the horn antenna, so only 390

unknown were optimized. In this case RVGA was used and it is obvious that much better convergence behavior compared with minimization algorithm in [7] can be obtained by suitable choice of minimization algorithm parameters.
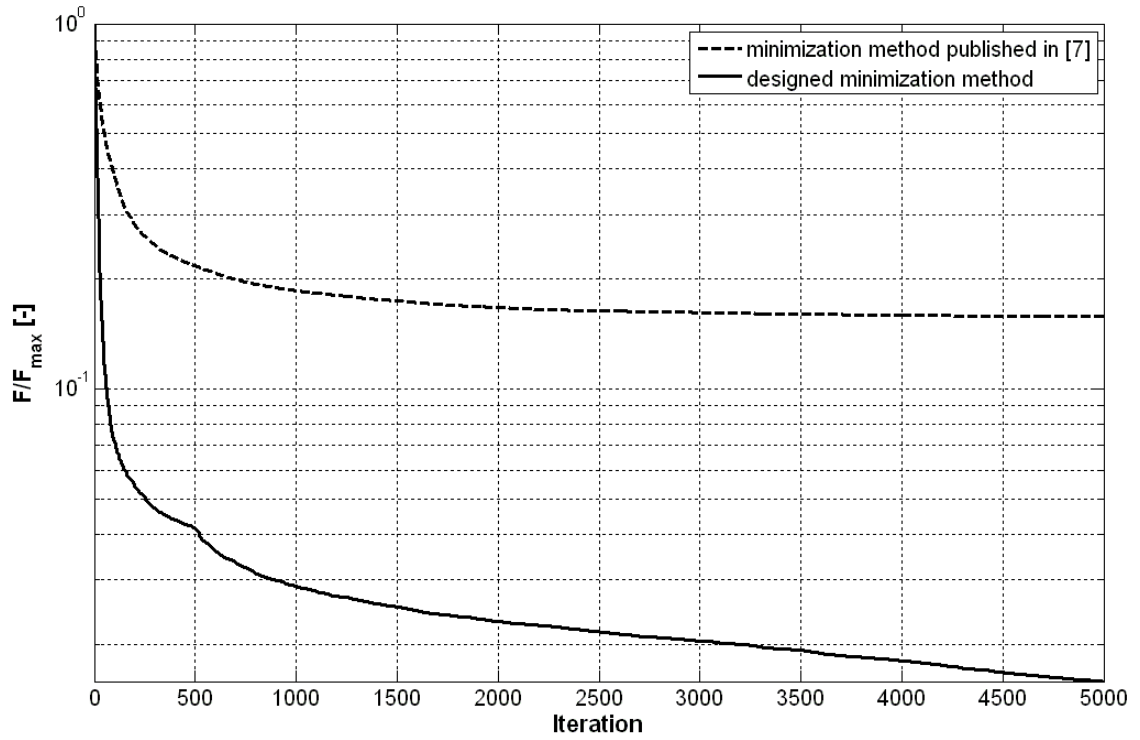
Fig. 3.33 Comparison of the till now published algorithm and designed one

3.2.2 Application of the designed minimization method for reconstruction of radiation patterns

The application of the described method was carried out on the radiation pattern reconstruction of the horn antenna and the antenna array (chapter 3.1.1). First, the designed minimization method based on global optimization is used. The FIA is only used consequently if the desired accuracy is not obtained.

The possibility of using initial estimate and the combination of different functionals will be investigated for accelerating the radiation pattern reconstructions in minimization method. The initial estimate consisting of amplitude obtained from the first scanning plane and uniform phase distribution (chapter 3.1.5) and the combination of the fitness function (3.7) and (3.8) (chapter 3.1.4) will be considered.

The horn antenna

For the horn antenna we have 390 unknown variables. That is why RVGA is used as global approach in minimization algorithm. As mentioned above, initial estimate obtained from the first scanning plane is used and radiation patterns calculated from this estimate are depicted by dotted line in Fig. 3.34 and Fig. 3.35. This initial estimate was improved by the designed method. The results obtained after 1000 iterations are shown also in Fig. 3.34 and Fig. 3.35 by dashed line. The reconstructed far-field radiation patterns show that the designed algorithm does not achieve accurate results yet but what is more important the obtained results are not much more accurate than the initial

estimate. So it seems that when the antenna is not so complex (antenna has relatively simple radiation pattern which is perpendicular to scanning plane) we can use initial estimate as estimate lying in the area of the global minimum.
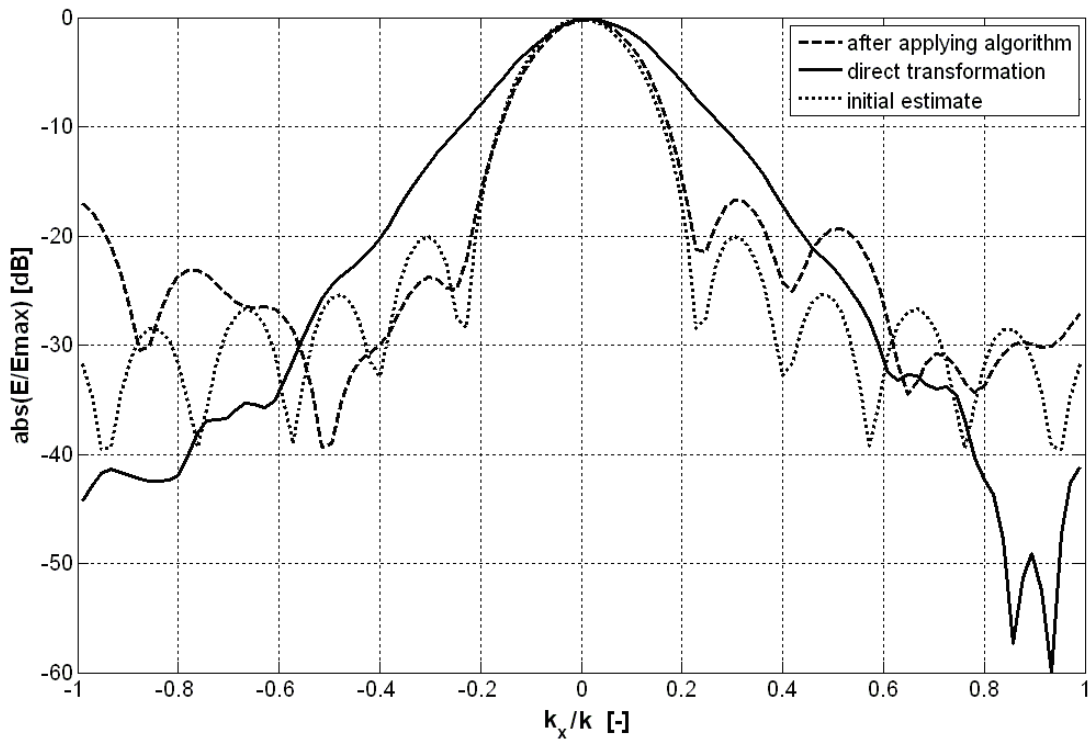
Fig. 3.34 Reconstructed H plane radiation pattern of the horn antenna after applying the designed algorithm
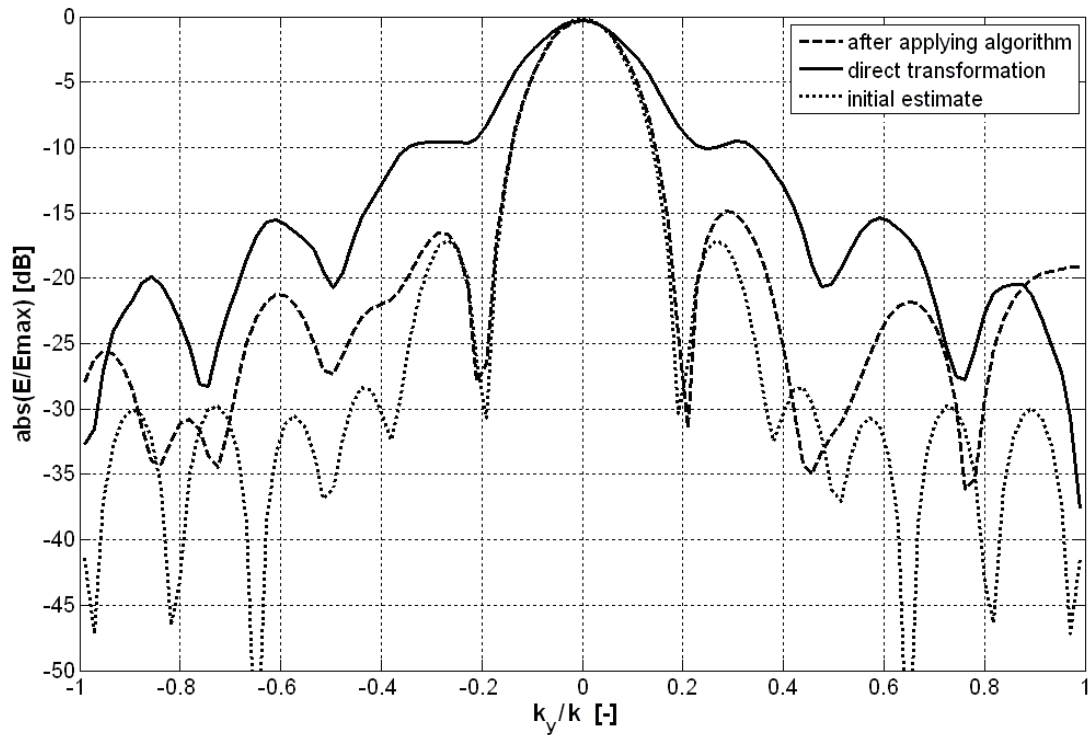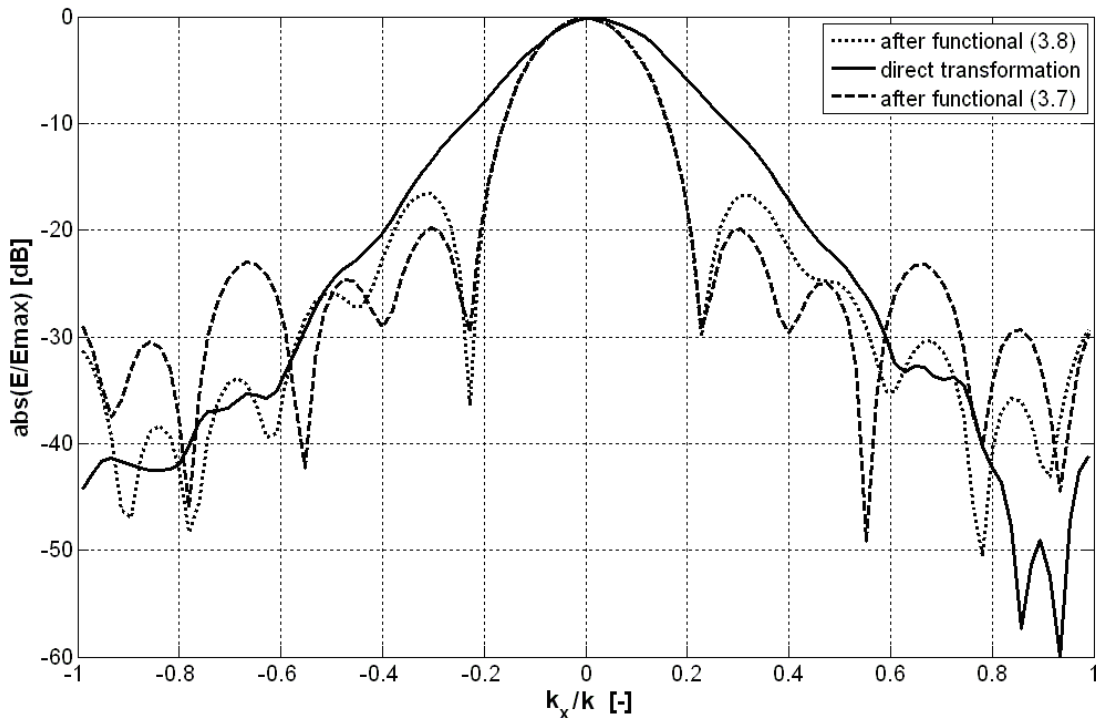

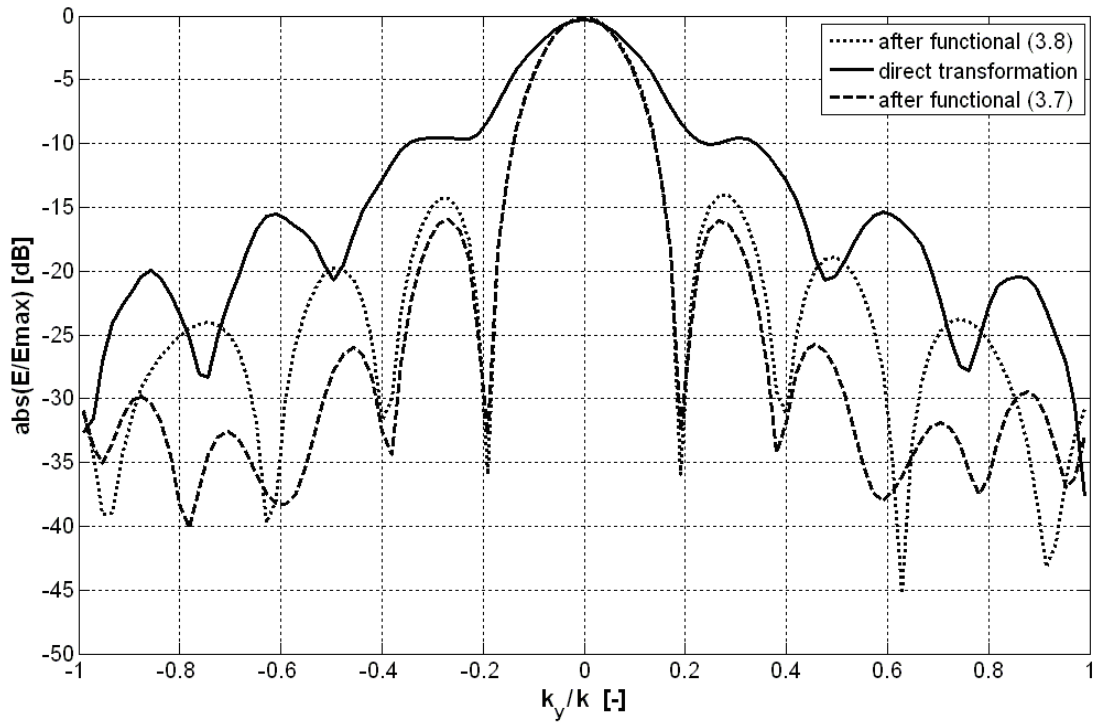**Fig. 3.35** Reconstructed E plane radiation pattern of the horn antenna after applying the designed algorithm

Now let us pay attention to using a combination of two functionals for reconstruction of radiation patterns. In chapter 3.1.4, it was found out that the functional (3.8) exhibits the fastest convergence properties but has problem with finding the global minimum area. It turned out that the possible solution is to consider functional (3.7) from the start and then, when the algorithm begins to stagnate, to switch to functional (3.8). The combination of the functional (3.7) and (3.8) is used for reconstruction of the horn antenna radiation patterns, Fig. 3.36 and Fig. 3.37.

The radiation patterns achieved by exploiting the functional (3.7) are shown in Fig. 3.36 and Fig. 3.37 by dashed line. They were obtained after 250 iterations then the functional was changed in the minimization algorithm and after 250 iterations the resulted radiation patterns were obtained, dotted line in Fig. 3.36 and Fig. 3.37.

So it was proved that the combination of the functionals is able to find global minimum. Moreover, it exhibits faster convergence rate and more precise reconstructions than in case where only the functional (3.7) is used. But the reconstructed far-field radiation patterns obtained only by functional (3.7) or combination of the functionals (3.7) and (3.8) still have not reached the required accuracy. For this purpose the local method or iterative algorithm has to be applied to ensure the required precision of the radiation patterns. The far-field results obtained after using the FIA are shown in Fig. 3.38 and Fig. 3.39. The reconstructed radiation patterns are in good agreement with the pattern gained by the direct transformation. This illustrates the correct result, thus finding a global minimum by the designed algorithm.

Fig. 3.36 Reconstructed H plane radiation pattern of the horn antenna after applying combination of two functionals

Fig. 3.37 Reconstructed E plane radiation pattern of the horn antenna after applying combination of two functionals
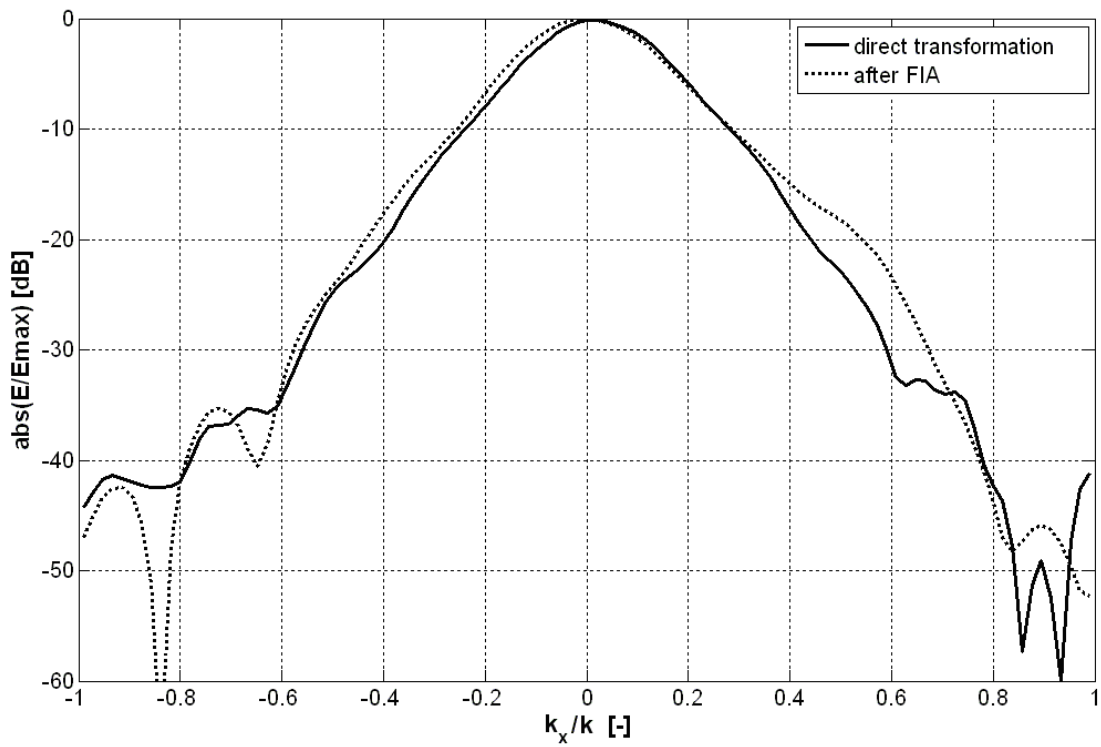
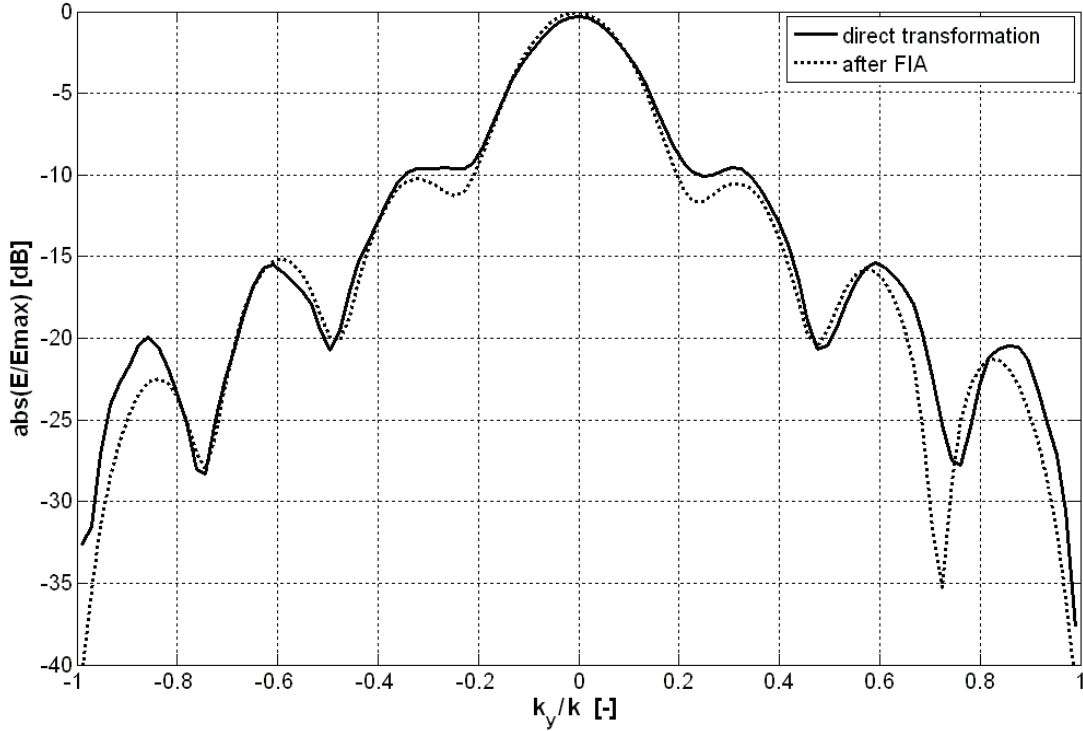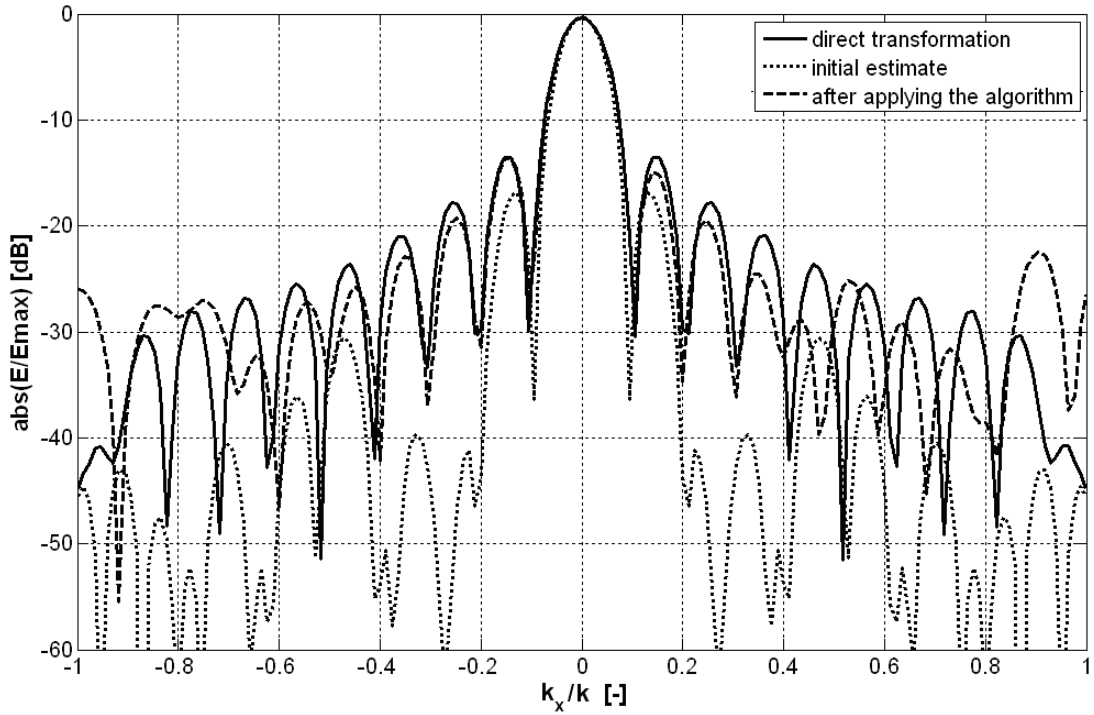**Fig. 3.38** Reconstructed H plane radiation pattern of the horn antenna after applying FIA

Fig. 3.39 Reconstructed E plane radiation pattern of the horn antenna after applying FIA
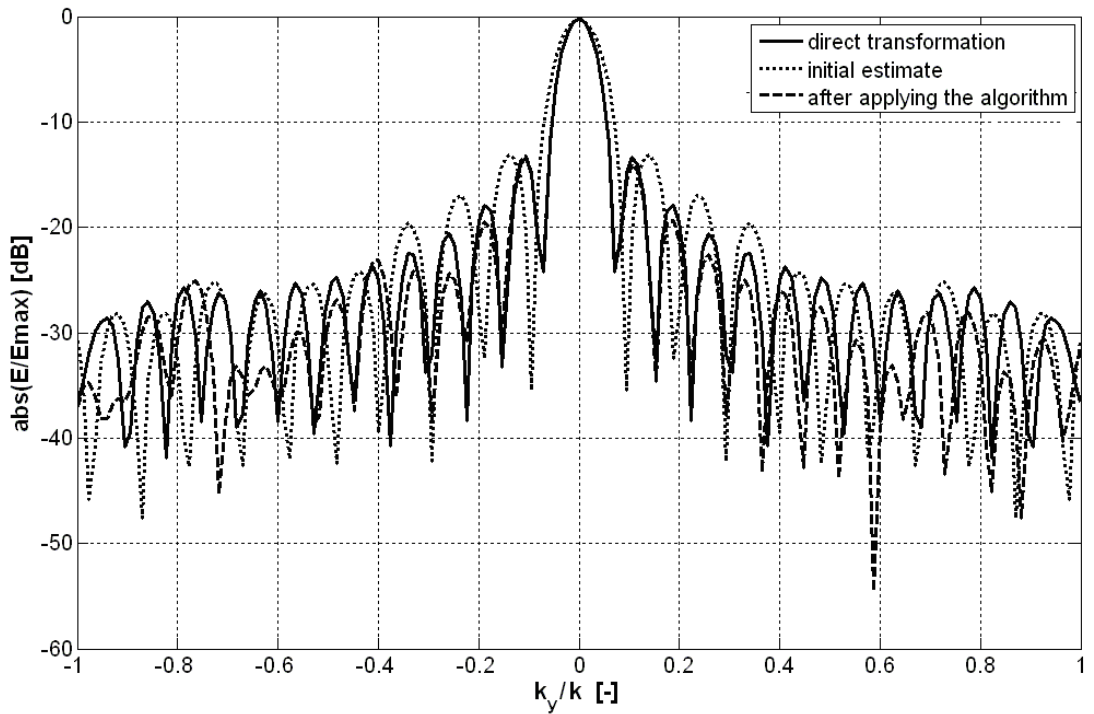
The antenna array

The verification of the previous considerations was made also for antenna array. The initial estimate obtained from the first scanning plane and the combination of the functionals is also considered. Since the number of the unknowns is about 2500 the PSO is used as global optimization technique.

The radiation patterns calculated from the initial estimate are depicted by dotted line and the radiation patterns from improved initial estimate (after 2000 iterations) are depicted by dashed line, see Fig. 3.40 and Fig. 3.41. Unlike the horn antenna, the antenna array has more complex electric field distribution on antenna aperture and radiation patterns. It is obviously from the figures that the initial estimate can lie in the area of the global minimum but also does not have to. Furthermore, more precise reconstruction after applying the algorithm was obtained. The agreement between the far-fields obtained by minimization algorithm and far-fields obtained by direct transformation is excellent in domain $|k_{x(y)}/k| = 0.2$. The results are fully satisfying when we are interested in only the main lobe area and highest level of the side-lobe (i.e. most important properties characterizing the antenna). Nevertheless, if we require higher accuracy, the FIA has to be used to improve it (Fig. 3.44 and Fig. 3.45).

When the functionals are combined, the results are shown in Fig. 3.42 and Fig. 3.43. The first functional (3.7) was used for the initial 500 iterations (dashed line) and the functional (3.8) for the other 500 iterations (dotted line). We can observe some improvements in reconstructed radiation patterns but accuracy is still insufficient even after applying the functional (3.8). So the local minimization method for their refinement must be used.
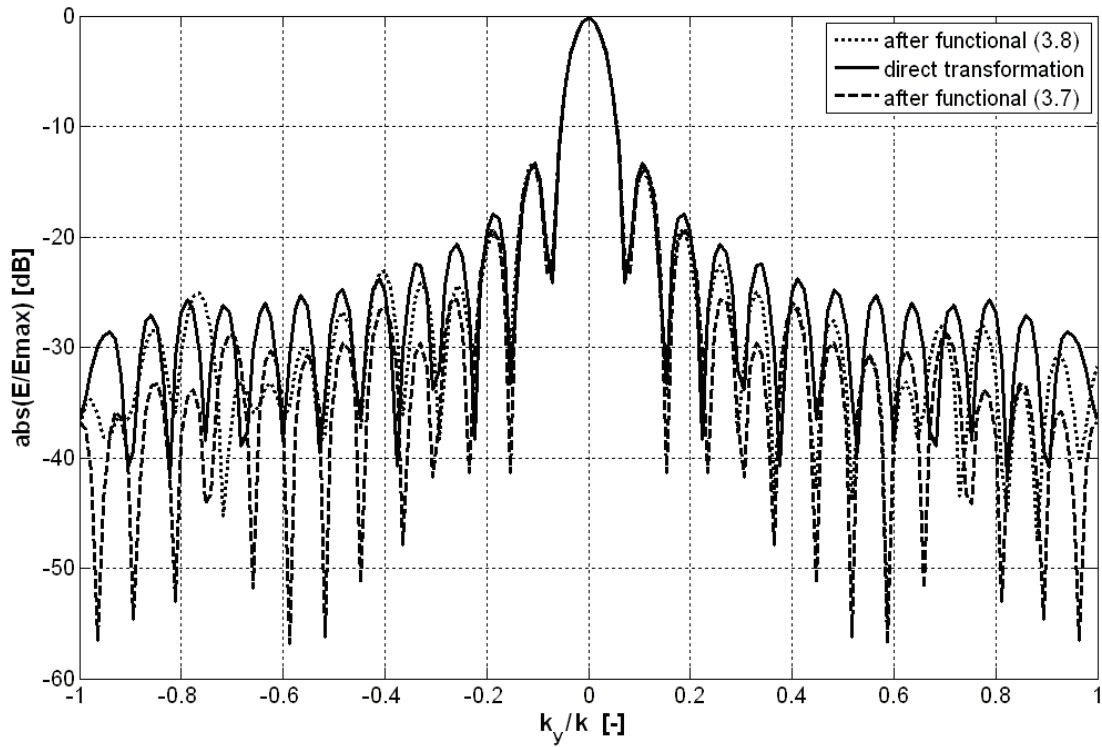
Fig. 3.40 Reconstructed H plane radiation pattern of the antenna array after applying the designed algorithm

Fig. 3.41 Reconstructed E plane radiation pattern of the antenna array after applying the designed algorithm
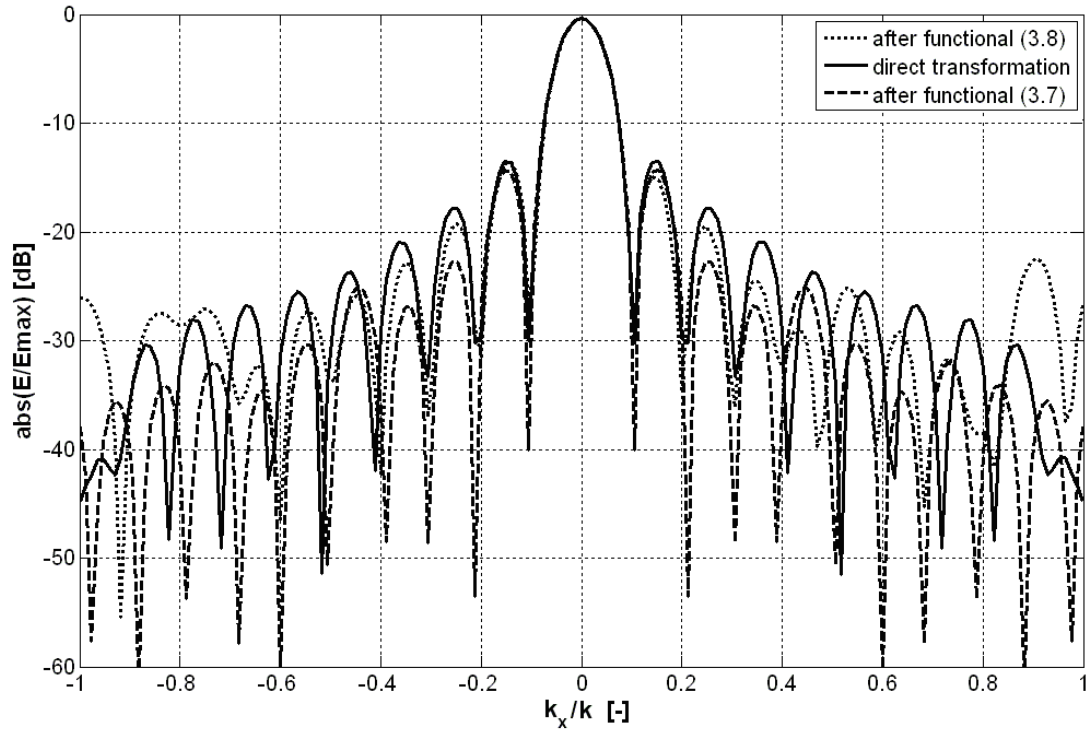
Fig. 3.42 Reconstructed H plane radiation pattern of the antenna array after applying combination of two functionals

Fig. 3.43 Reconstructed E plane radiation pattern of the antenna array after applying combination of two functionals
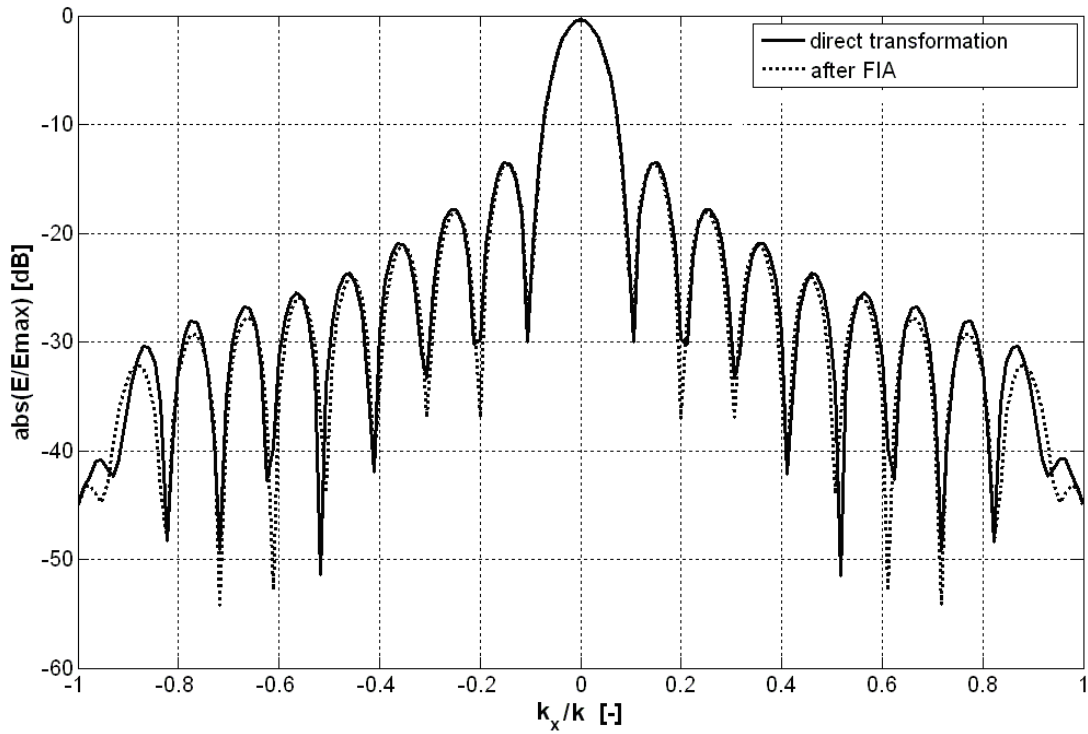
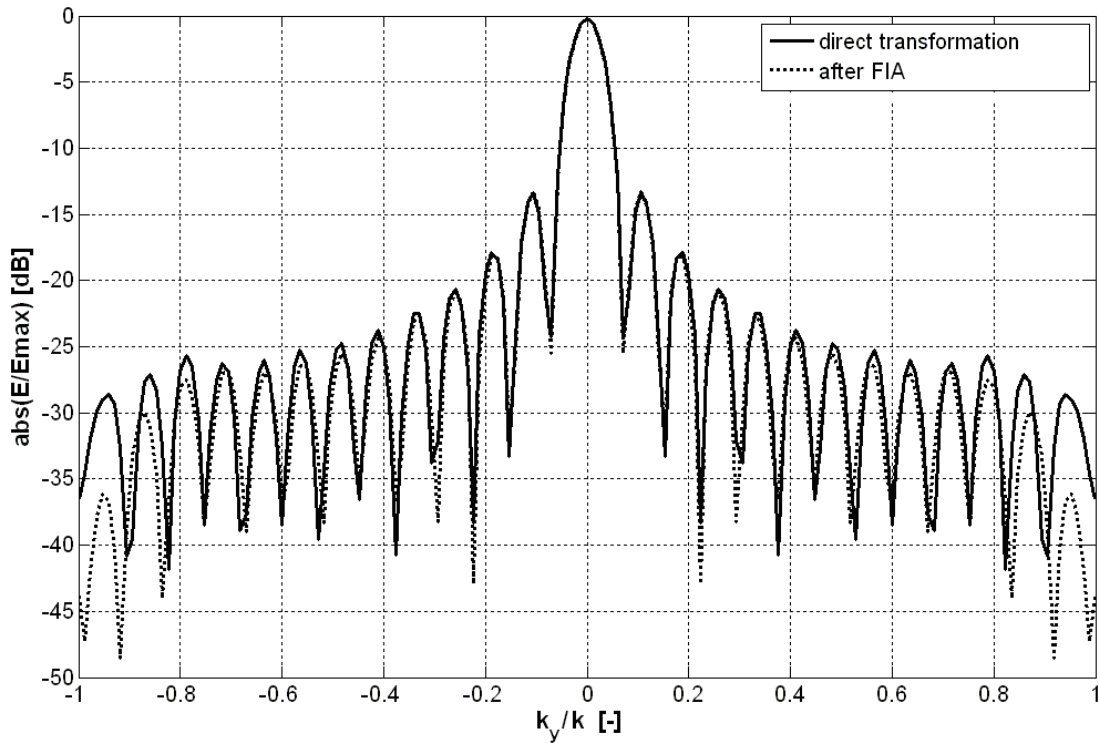**Fig. 3.44** Reconstructed H plane radiation pattern of the antenna array after applying FIA

Fig. 3.45 Reconstructed E plane radiation pattern of the antenna array after applying FIA

To conclude, it was found out that if we reconstruct the radiation patterns of antenna having relatively simple electric field distribution on antenna aperture and the radiation pattern perpendicular to the scanning plane, we can use initial estimate obtained from the first scanning plane as estimate lying in the area of the global

minimum. If the antenna has more complex electric field distribution on antenna aperture, the application of the designed minimization method is preferable.

It was also found out that the designed algorithm using combination of functionals (3.7) and (3.8) exhibits faster convergence rate and more precise reconstructions than in the case where only the functional (3.7) is used but the accuracy obtained by minimizing algorithm is not sufficient in most cases. So if the precise knowledge of the antenna radiation patterns is required, it is necessary to use the local minimization method (FIA) for their refinement.

The first part of the designed algorithm uses global optimization to find the initial estimate, which lies in the area of global minimum. The use of global optimization to minimize the functional brings a significant simplification and acceleration of the whole minimization. The implementation of the global optimization is very simple and takes only a few lines of source code. Since the minimized field distribution on the antenna aperture is always smaller than the electric field distribution on the scanning plane, the algorithm is faster and computationally less expensive. The second part of the minimizing algorithm is Fourier iteration algorithm which improves the initial estimate obtained by the global optimization. The attainable accuracy of the obtained radiation patterns after applying the designed algorithm with FIA is comparable with other published methods, especially with methods based on local minimization of functional [10], [11], [23] - [26], [28].

An algorithm designed in this way works very effectively for electrically small antennas. But especially when we have to analyze radiation properties of electrically large antennas, the problem description comprises several thousands of unknowns, and CPU-time demands of the minimizing process are enormous. Under these circumstances, the unknown electric field distribution can be represented by a few coefficients.

In the following section of the work, a novel method combining a global optimization with an image compression method is presented. It is in fact the previously designed minimization method complemented by an image compression method.

3.3 Novel phase retrieval algorithm

The novel method combining global optimization with compression method is also based on amplitude measurements in two different distances from AUT. The global optimization method (GO) is used for minimizing the fitness function (functional) and compression method (CoM) is used for reducing the number of unknown variables [64], [65].

In the next sections, the novel phase retrieval algorithm exploiting the CoM is described. For this purpose, two image compression methods are compared and their properties are investigated for the solution of our problem. The Discrete Cosine Transform (DCT) and the Discrete Wavelet Transform (DWT) are considered for reducing the number of unknown variables. Finally, the verification of the novel method is carried out on the radiation pattern reconstruction of the dish antenna (chapter 3.1.1) and lens antenna. In both of these cases we have to optimize thousands of unknown variables.

3.3.1 GO/CoM/FIA method

The goal of the algorithm is the same as the goal of the previous method: to reveal the minimal function representing the complex intensity of the electric field distribution on the aperture of the measured antenna. If the phase distribution on the aperture is known, both, phase distribution on both scanning planes and the antenna radiation patterns can be determined. The algorithm assumes also knowledge of amplitude sets on two scanning planes, scanning planes distances from the AUT and dimensions of the AUT (shown in Fig. 3.46).
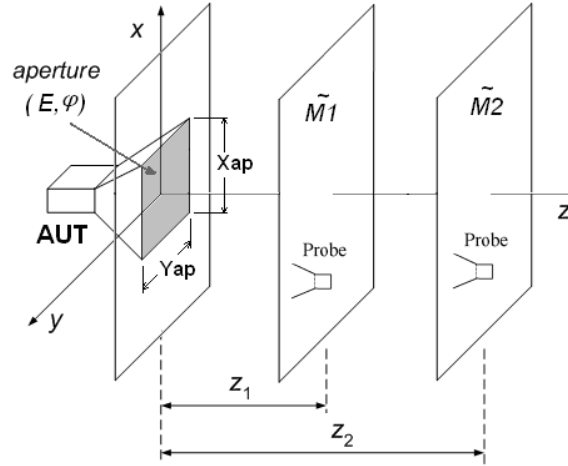

Fig. 3.46 Principle of the GO/CoM/FIA method

The flow chart of the minimization algorithm exploiting global optimization and compression method is depicted in Fig. 3.47. First, random initial guess of the DCT (DWT) coefficients is made. After the inverse DCT (DWT) is carried out, we obtain electric field distribution on the antenna aperture. Zero padding is applied to the distribution to get the same extension as the scanning surfaces have. After this operation, the initial electric field on aperture is transformed (using 2D FFT) to the plane wave spectrum (PWS) and moved by the propagation constant to the distance of the first scanning plane. In the next step, the calculated amplitudes of the first plane are replaced with the measured ones. The resultant field is then propagated to the next plane, and the calculated amplitudes of the second plane are again replaced with the measured ones. Electric field in second plane is projected back to first plane and the error is calculated according the same fitness function (3.7) but only for first plane.

We have to take into account that the lossy compression methods are used so the accuracy of retrieved far-field may not be sufficient in some cases. Then the accuracy of the retrieval scheme can be improved by a local method. So, in the next phase, Fourier iterative algorithm which minimizes the same functional is chosen to improve the initial estimate obtained by minimization method.

The selection of the optimization approach, global optimization technique and the choice of the minimizing functional was made in previous chapters. In the next section, two image compression methods for reducing the number of unknown variables are considered and compared.
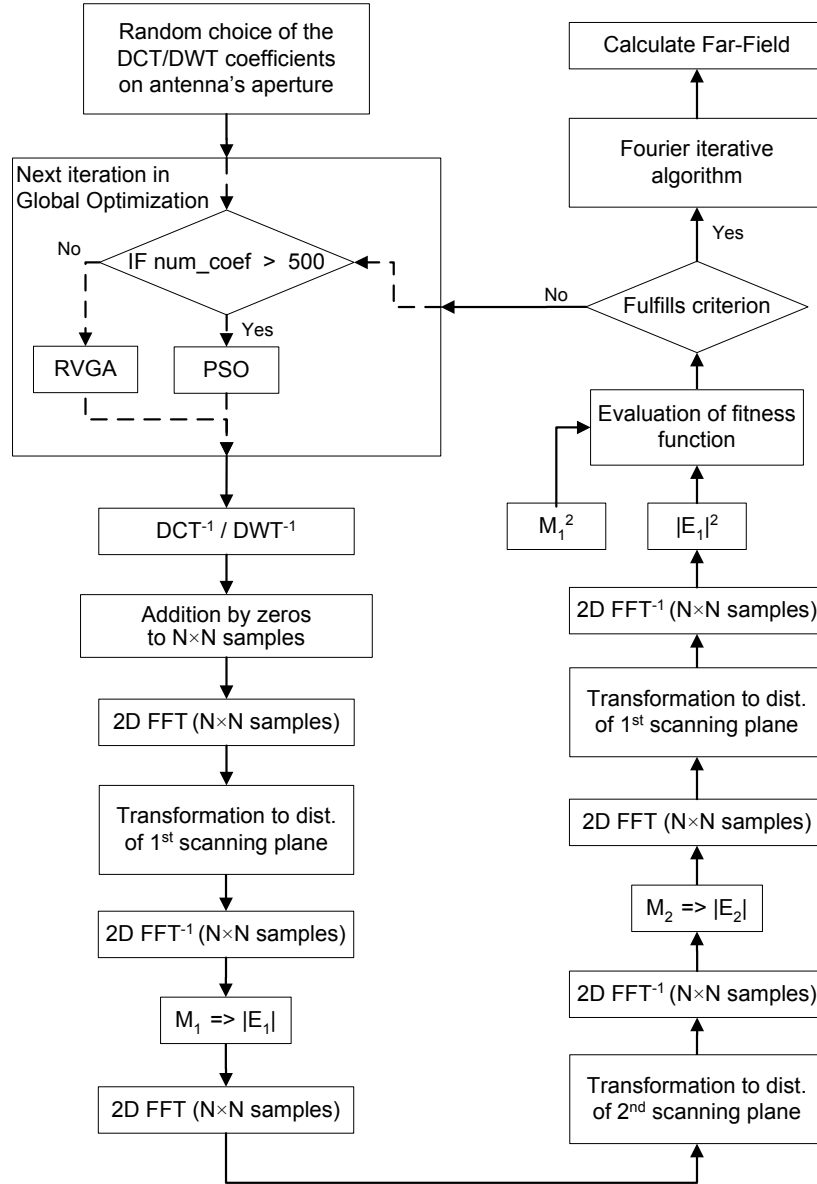
Fig. 3.47 Flow chart of the minimization algorithm exploiting global optimization and compression method

3.3.2 Compression methods: DCT and DWT

Two image compression methods were applied in order to reduce the number of unknowns – the 2D Discrete Cosine Transform and 2D Discrete Wavelet Transform. Properties of both methods are investigated, and their advantages/disadvantages for the reconstruction of the antenna near field are discussed [64].

3.3.2.1 The discrete cosine transform DCT

In 1974, the discrete cosine transform (DCT) was first introduced by Ahmed, Natarajan, and Rao [44]. In particular, the DCT was categorized into four slightly different transformations named DCT-I, DCT-II, DCT-III, and DCT-IV. DCT-II is concerned in this paper. The DCT is often used in signal and image processing,

especially for lossy data compression. The DCT converts data into sets of frequencies. The first frequencies in the set are the most meaningful, the latter are the least. To compress data, the least meaningful frequencies are stripped away based on allowed resolution loss. The definition of the 2D DCT-II for an input data A and output data B is

$$B_{pq} = \alpha_p \alpha_q \sum_{p=0}^{M-1} \sum_{q=0}^{N-1} A_{mn} \cos \frac{\pi(2m+1)p}{2M} \cos \frac{\pi(2n+1)q}{2N}$$ (3.10)

$$\alpha_p = \begin{cases} 1/\sqrt{M}, & p = 0 \\ \sqrt{2/M}, & 1 \le p \le M\text{-}1 \end{cases} \quad \alpha_q = \begin{cases} 1/\sqrt{N}, & q = 0 \\ \sqrt{2/N}, & 1 \le q \le N\text{-}1 \end{cases}$$ (3.11a, 3.11b)

where M and N are the row and column size of A, respectively. The inverse transform is defined:

$$A_{mn} = \sum_{p=0}^{M-1} \sum_{q=0}^{N-1} \alpha_p \alpha_q B_{pq} \cos \frac{\pi(2m+1)p}{2M} \cos \frac{\pi(2n+1)q}{2N}$$ (3.12)

Further on, the influence of the number of coefficients which are used for reconstruction of unknown field distribution and its error is analyzed.
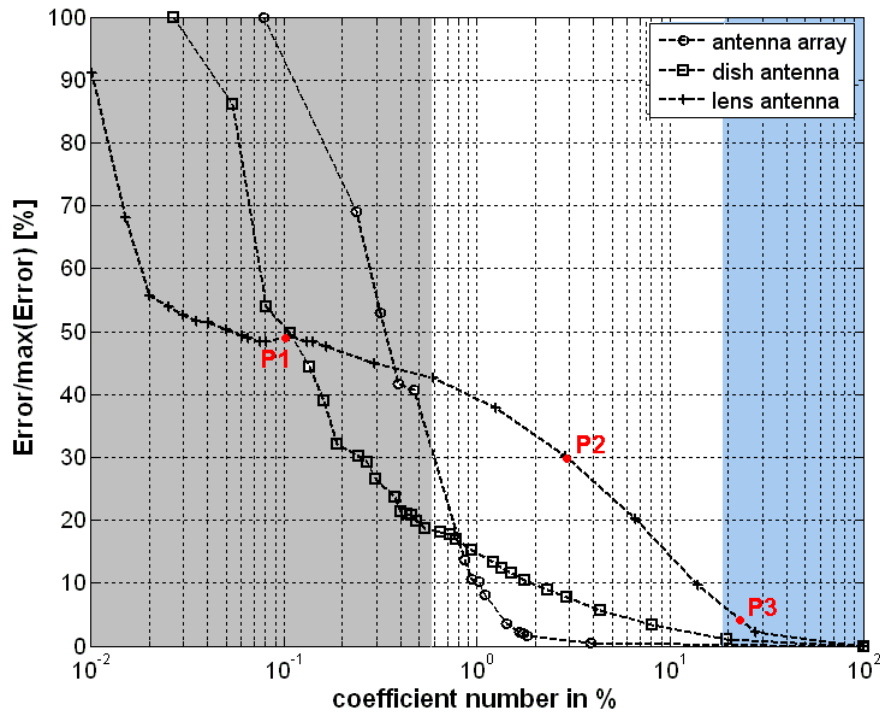
Fig. 3.48 Dependences of the coefficient number on calculated error from different electric field distribution

The analyses of the coefficient number influence were performed on data of electric field intensity of the lens antenna, dish antenna and antenna array (chapter 3.1.1). In Fig. 3.48, dependences of the coefficient number which are taken into account for reconstruction of the fields on calculated error are depicted. Since all curves have different progress, we are not able to generalize dependence of the number of

coefficients on error exactly. But it can be noticed that if we required precise results, we have to take into account more than 20 % of coefficients (blue area). On the other hand, if very rough estimate is needed, we can consider only a fraction of coefficients, less then 0.5 % (grey area).

For the lens antenna, the dependence of the electric field distribution error on the number of coefficients was analysed. The principle of the analysis is shown in Fig. 3.49. We examined three different numbers of coefficients (Fig. 3.48): P1 = 19 coefficients (0.1% of all coefficients), P2 = 397 coefficients (2%), P3 = 4 373 coefficients (22%). Then, we made the inverse discrete cosine transform IDCT and calculated the radiation patterns (Fig. 3.49).
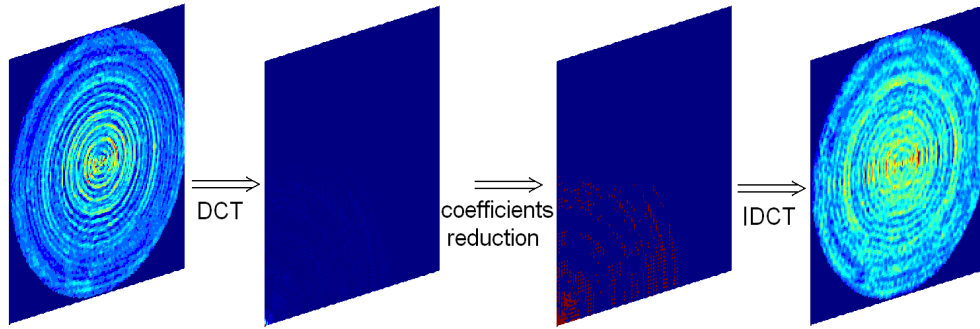

Fig. 3.49 Principle of the analysis of the coefficient number influence
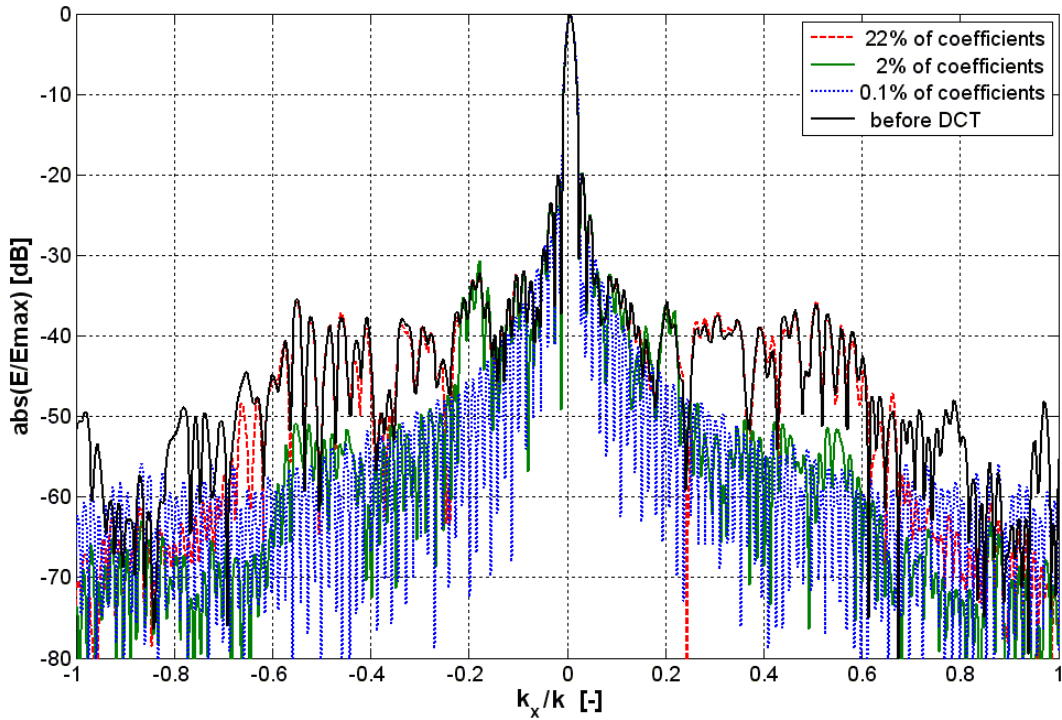

Fig. 3.50 Calculated radiation patterns of the lens antenna for different numbers of coefficients

As it is obvious from Fig. 3.50, high frequency terms relate to the far side-lobes, which are at lower level and therefore they are not taken into account. 22 % of the coefficients relates to $k_x/k \leq \pm 0.6$ and 2% of the coefficients to $k_x/k \leq \pm 0.2$. Thus, a large number of coefficients ensures a good agreement between the required pattern and

the reconstructed one. On the other hand, if a fraction of variables is used, a rough estimate of the radiation pattern is obtained, and the agreement is achieved in the domain of the main lobe only.
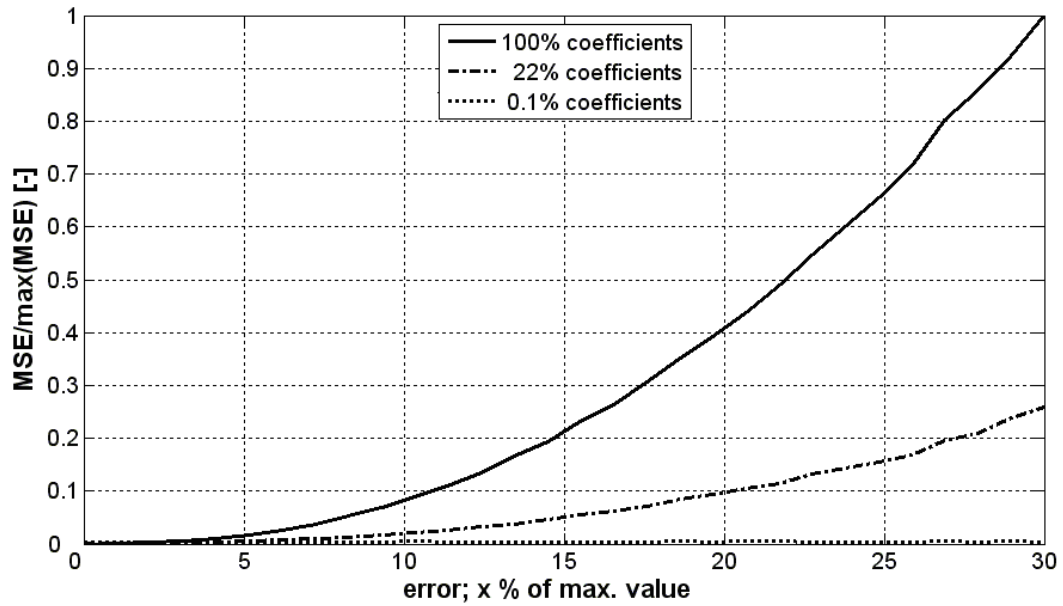

Fig. 3.51 Analyses of the influence of the coefficient error

Fig. 3.51 depicts the analyses of the influence of the coefficient error. We loaded the coefficients by random error of size up to 30% of maximum value of the coefficient. Clearly, calculated mean square error (MSE) from reconstructed electric field distribution grows exponentially with the coefficient error. Further it is obvious, that error dependence is more expressive with increasing number of coefficients. So if we optimize a very large number of coefficients and we come out from a random initial guess, the finding of solution will be very lengthy. From this point of view it is better to use the DCT only for finding the global minimum area.

In case of the DCT, precise results require a large number of coefficients. But, a very strong influence of errors is a disadvantage. We therefore have to use an initial estimate calculated from the electric field distribution on the first scanning plane. If only a rough estimate is needed, a random guess of a fraction of coefficients can be used. For that reasons, a compromise between these two cases should be chosen.

3.3.2.2 The discrete wavelet transform DWT

The discrete wavelet transforms are based on the use of recurrence relations to generate progressively finer discrete samplings of an implicit mother wavelet function [45]. The DWT has a large number of applications in science and it is primarily used for data compression.

The principle of DWT

The DWT analyzes the signal at different frequency bands with different resolutions by decomposing the signal into a coarse approximation and detail information. The DWT employs wavelet functions, which are associated with low pass and high pass filters, respectively. For images, two-dimensional wavelets are exploited.

The resulting 2D array of coefficients contains four bands of data, the approximation CA, and the details in three orientations (horizontal CD$^{(h)}$, vertical CD$^{(v)}$, and diagonal CD$^{(d)}$), corresponding to the first level of image decomposition. The CA band can be further decomposed in the same manner for the second level of decomposition. This can be done up to any level, resulting in a pyramidal decomposition. The filter bank structure of 2D DWT decomposition is shown in Fig. 3.52 (left) and the two levels decomposed scheme is depicted in Fig. 3.52 (right). In my case, Biorthogonal wavelets were chosen as decomposition and reconstruction filters.
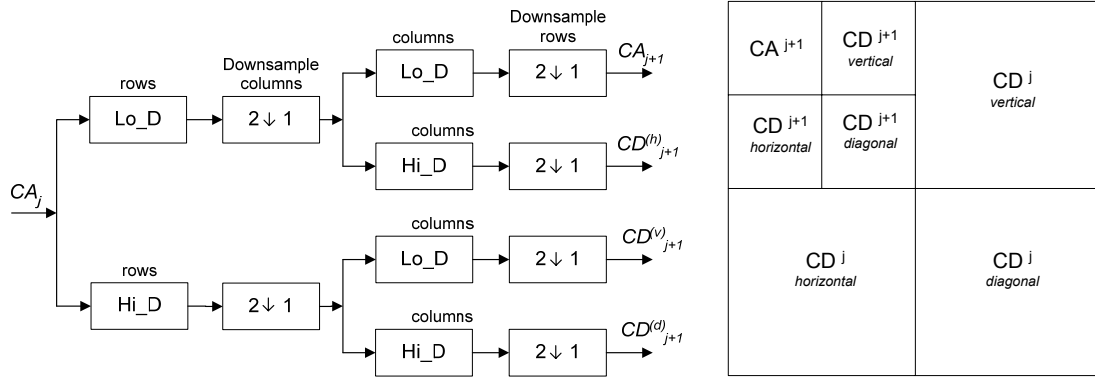

Fig. 3.52 DWT: Filter bank structure for one level of image decomposition; two levels decomposition scheme

In case of DWT, the influence of the number of the decomposition steps and the influence of random errors is analyzed. Analyses were also made for the lens antenna.

The influence of decomposition steps is documented in Fig. 3.53 and Fig. 3.54. Each decomposition leads to a fourfold reduction of variables, so that after three decompositions the number of unknowns is reduced 64 times. Electric field distribution and calculated radiation patterns are depicted for three decomposition steps.
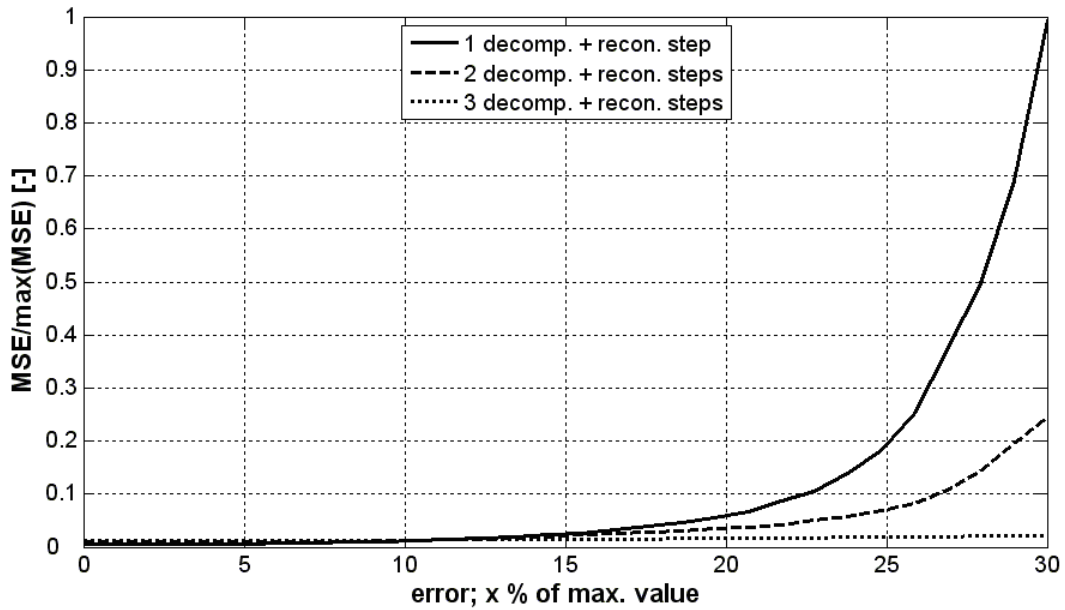
In Fig. 3.54 we can observe an agreement in domain $|k_x/k| = 0.15$ for all decompositions. But the agreement in wide range can be observed only in case of one decomposition step.
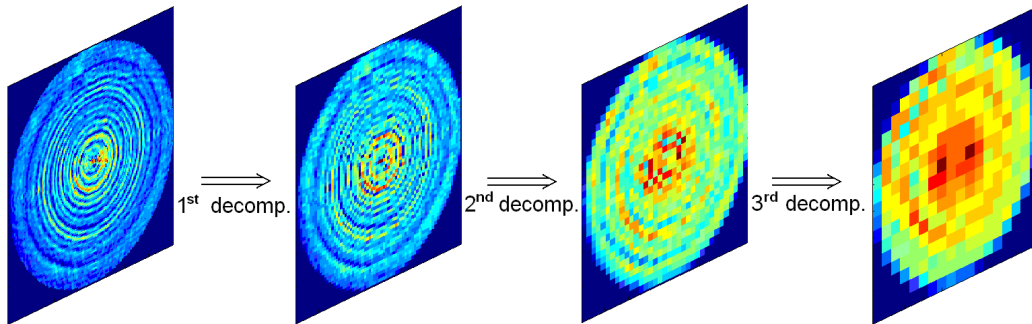
Fig. 3.53 Principle of analysis of the decomposition steps influence
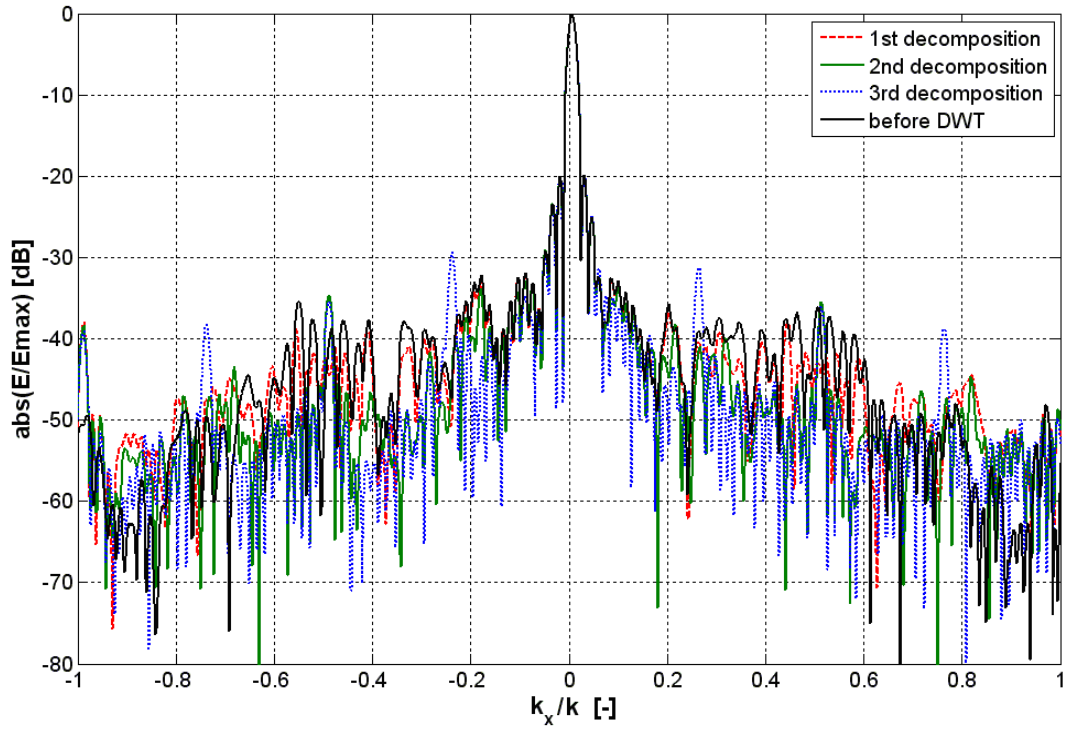
Fig. 3.54 Calculated radiation patterns of the lens antenna for different numbers of the decompositions

Fig. 3.55 Analyses of the influence of the random error

Fig. 3.55 analyzes the effect of random error in decomposed electric field distribution. Clearly, error in reconstructed electric field distribution also grows exponentially with increasing random error and error effect is more significant in cases when we have to optimize a larger number of unknowns.

Dealing with DWT, only one decomposition step (fourfold reduction) can be considered to obtain accurate results, but the influence of errors is very significant then.

Therefore, we are looking for estimation only. Using more than a single decomposition is more useful. Further it was found out that the DWT is less sensitive to random error than DCT and we can always come out from random initial guess.

Shortly, the DCT and the DWT are easy to implement. The DCT provides better reduction of the number of optimized variables. If more than rough estimate is required, the initial estimate calculated from the electric field distribution on the first scanning plane has to be used. Since the DWT is less sensitive to the random error than the DCT, the initial guess can be chosen randomly. The advantages and disadvantages of the image compression methods are summarized in Table. 3.3.

Table 3.3 The advantages and disadvantages of the image compression methods

Method	**DCT**	**DWT**
Implementation	Easy	Easy
Compression ratio	$4 \div 200$ (and more)	$4 \div 64$
Sensitive to the random error	DCT is more sensitive than DWT	
Initial guess (low compression ratio)	Yes	No
Initial guess (high compression ratio)	No	No

For its better compression properties (number of the optimized variables can be reduced a hundred times and more), the DCT is used for reconstruction of the radiation patterns.

3.3.3 Comparison of algorithms with and without compression method

In Fig. 3.56, we can see the comparison of convergence properties for minimization algorithm without the DCT and with the DCT. In each case, ten repeats were performed and the optimization was stopped in the 2000th iteration. The convergence properties were investigated for the dish antenna.

As it is obvious, the algorithm using the DCT exhibits better convergence properties. Although the implementation of the compression method is a quite time-consuming operation, the algorithm brings remarkable optimization time savings. The algorithm with the DCT is approximately eight times faster than without it. It is because only a fraction of the coefficients representing searched electric field on antenna aperture is optimized.
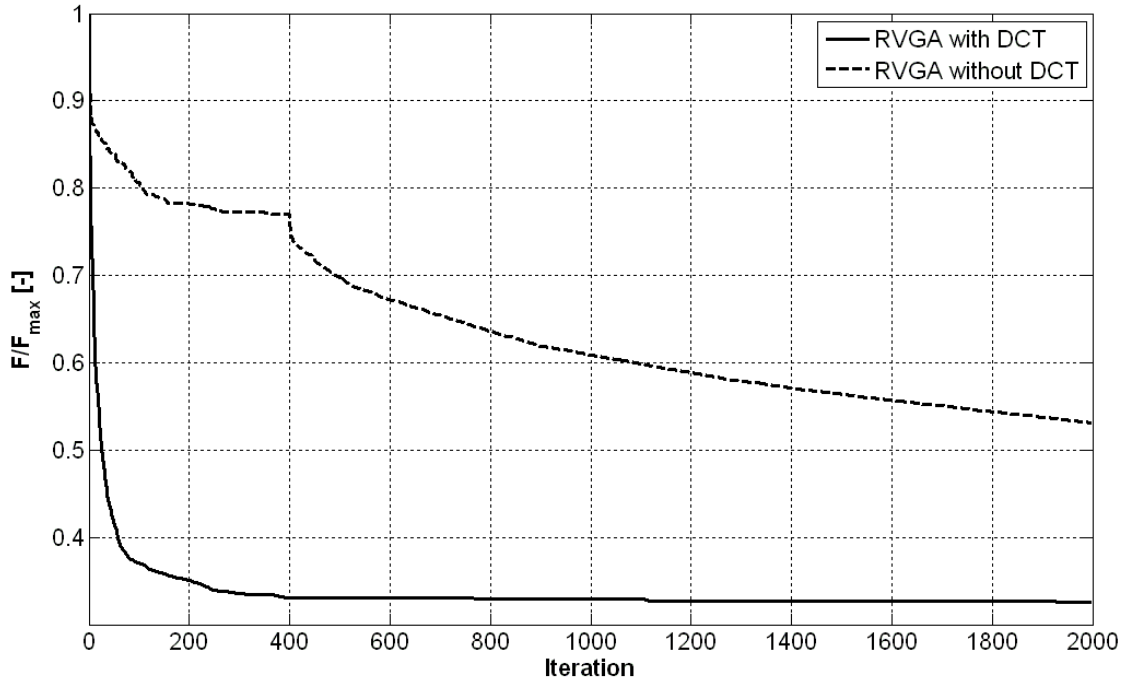
Fig. 3.56 Comparison of convergence properties for algorithms without and with the DCT

3.3.4 Application of GO/CoM/FIA method for reconstruction of radiation patterns

The verification of the described novel method was carried out on the radiation pattern reconstruction of the dish antenna and the lens antenna (chapter 3.1.1). In both cases the number of the optimized variables is in thousands, dish antenna has 3 721 complex unknowns and lens antenna has 18 225 complex unknowns.
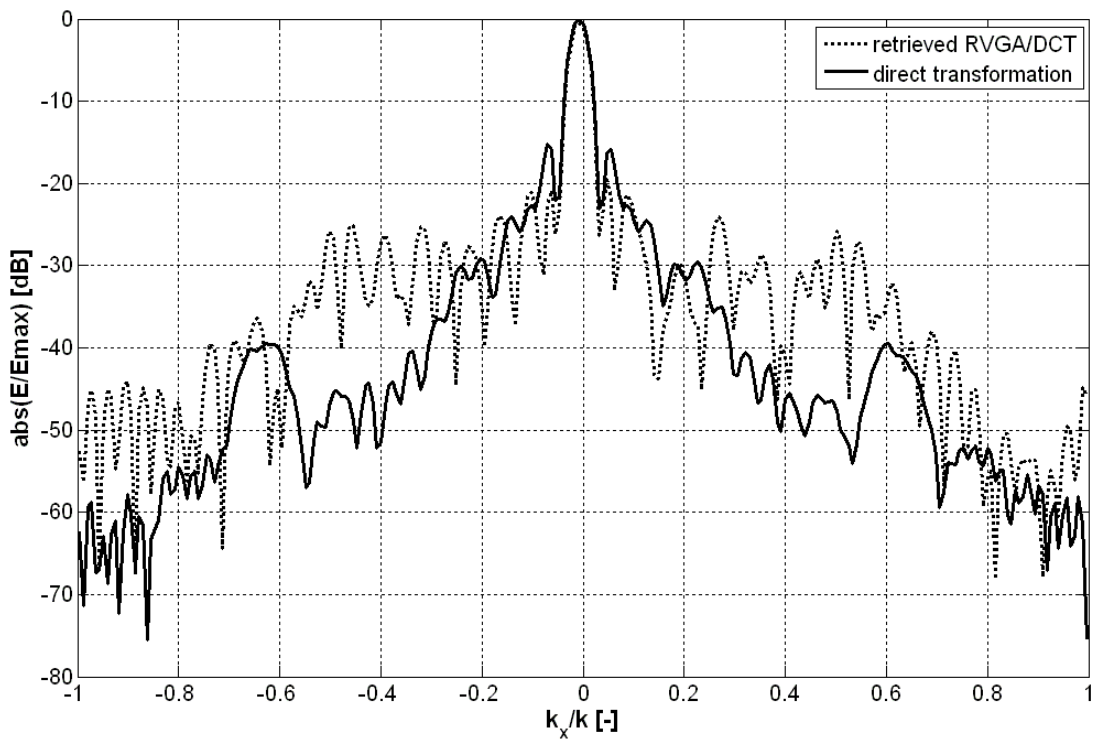
The dish antenna

The contour plots of the amplitude near-field directly measured by the probe at frequency 14.4 GHz are depicted in Fig. 3.6 for both scanning planes.

First global optimization with compression method was used for the initial reconstruction of the phases and amplitudes on the antenna aperture. Approximately 40 coefficients (1 % of all the coefficients) were used for the reconstruction that is why RVGA is used as the global approach. The far-field results obtained by the methods RVGA/DCT after 50 iterations are shown in Fig. 3.57 and 3.58 respectively. The reconstructed far-field radiation patterns prove that obtained initial estimate lies in area of the global minimum. After this, we applied the FIA to ensure the required precision of the radiation patterns. The far-field results obtained after applying the FIA are shown in Fig. 3.59 and 3.60. The agreement between the far-field obtained from the retrieved and directly measured near-field amplitude and phase is excellent.
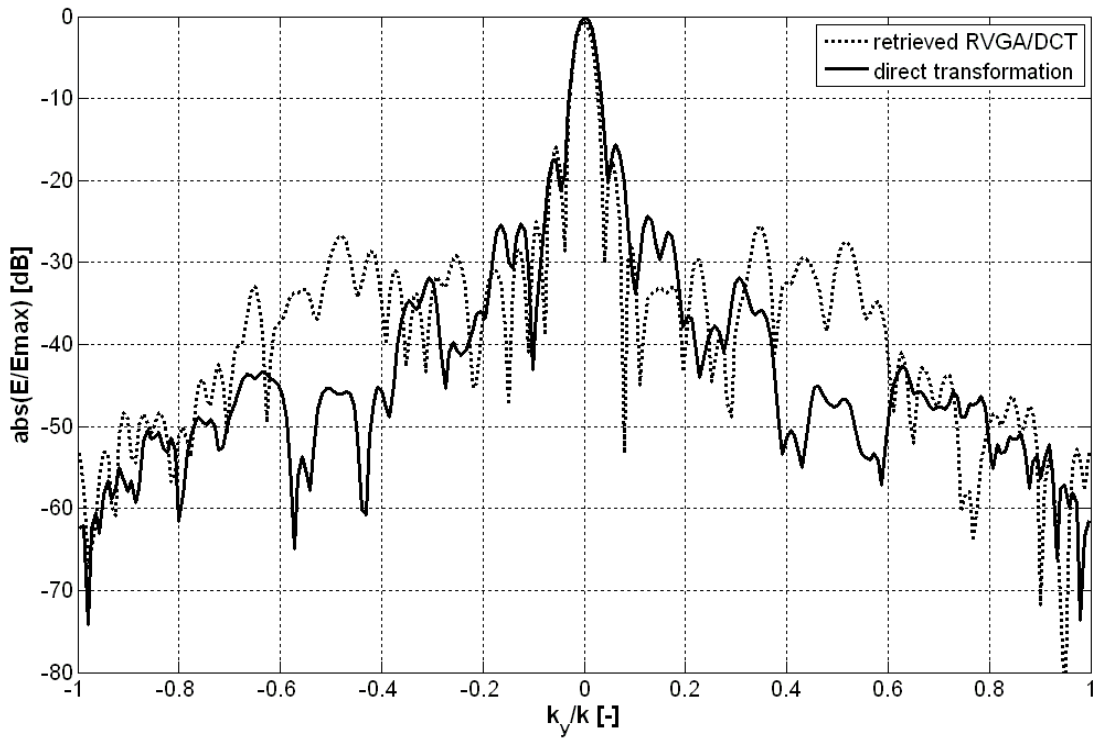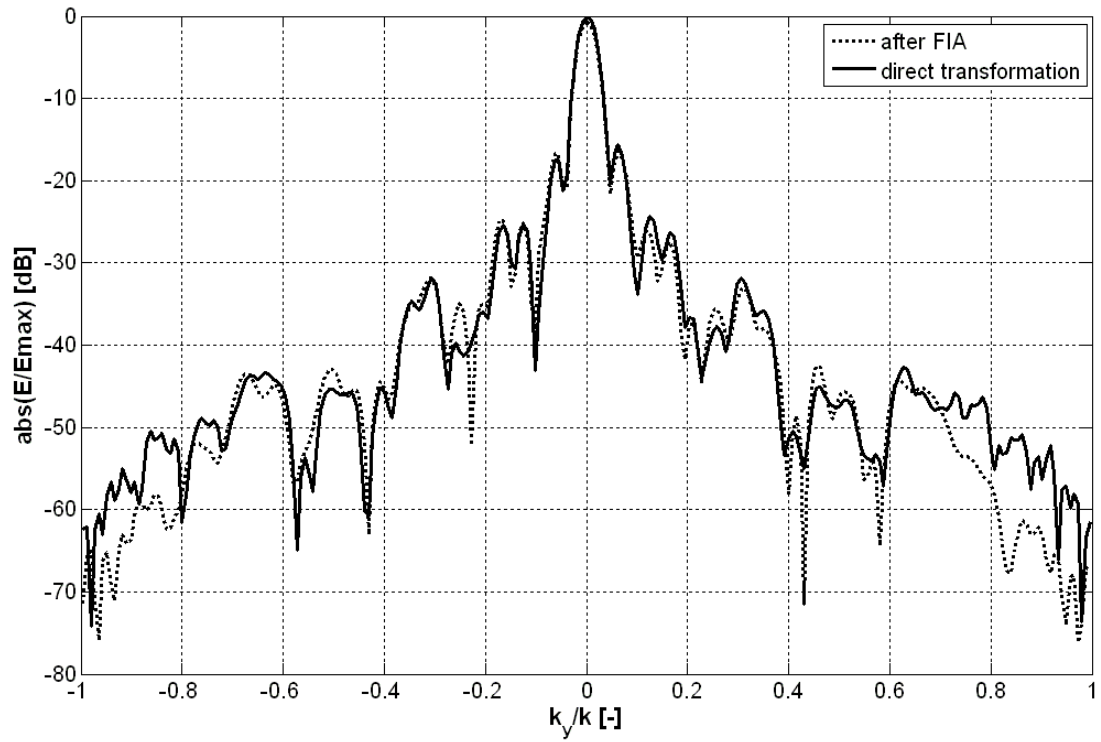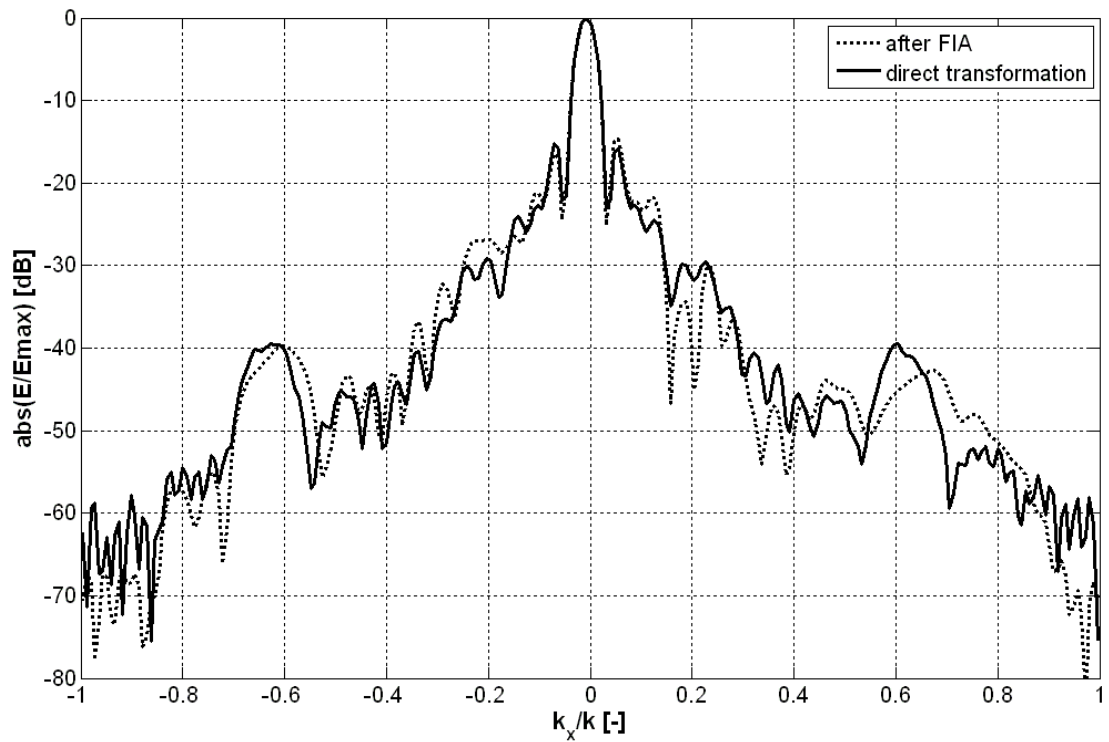
Fig. 3.57 Reconstructed E plane radiation pattern of the dish antenna after applying RVGA/DCT; E plane.

Fig. 3.58 Reconstructed E plane radiation pattern of the dish antenna after applying RVGA/DCT; H plane.

Fig. 3.59 Comparison of the far-field obtained from the accurate and retrieved near-field phase; E plane
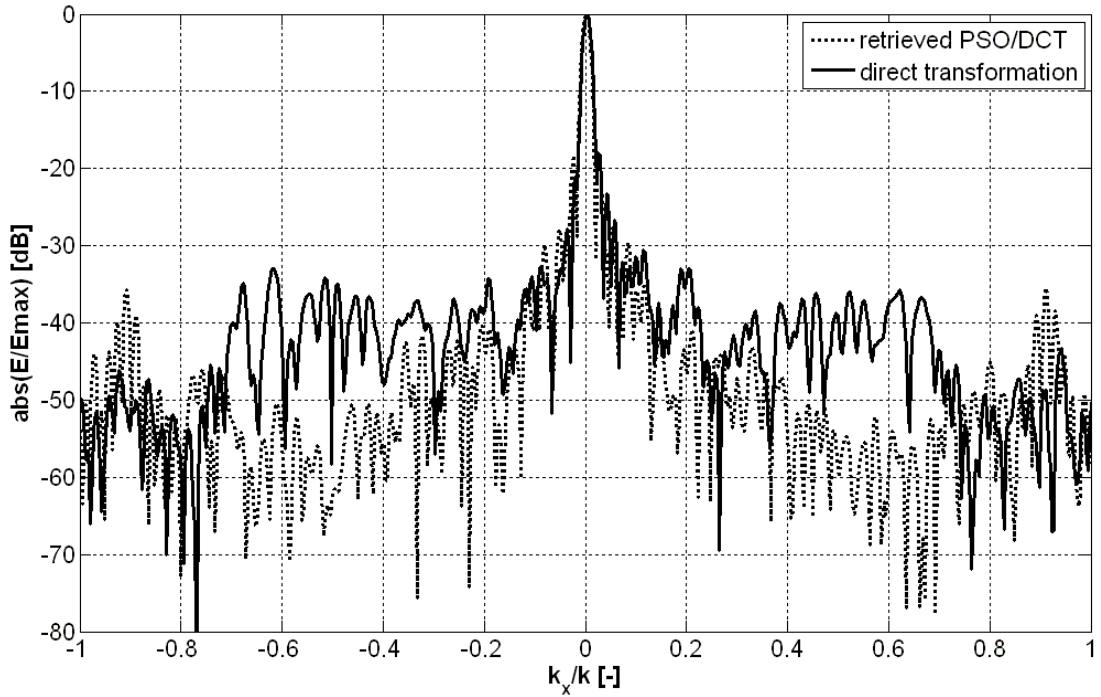

Fig. 3.60 Comparison of the far-field obtained from the accurate and retrieved near-field phase; H plane

The Teflon lens antenna

In case of the lens antenna the solution space contains 18225 complex parameters which optimal values should be found out. The contour plots of the measured amplitudes are depicted in Fig. 3.10. Since approximately 900 coefficients (5 % of all the coefficients) were used for the reconstruction, the PSO was used in combination with the DCT.

The PSO/DCT method was used for the initial reconstruction of the phases and amplitudes on the antenna aperture. The far-field results obtained after 100 iterations are shown in Fig. 3.61 and Fig. 3.62, respectively. The agreement between the retrieved far-field and the directly measured one is excellent in domain of above 30 dB. We can observe that the retrieved far-field becomes less accurate approximately below -30 dB. Therefore, radiation pattern is improved by FIA. The far-field results obtained after applying the FIA are shown in Fig. 3.63 and Fig. 3.64. The agreement between the far-field obtained from the retrieved and directly measured near-field amplitude and phase is excellent in domain k_x/k $(k_y/k) = \pm 0.4$.

Fig. 3.61 Initial reconstruction of H plane radiation pattern of the lens antenna and comparison with radiation pattern obtained from measured complex near field
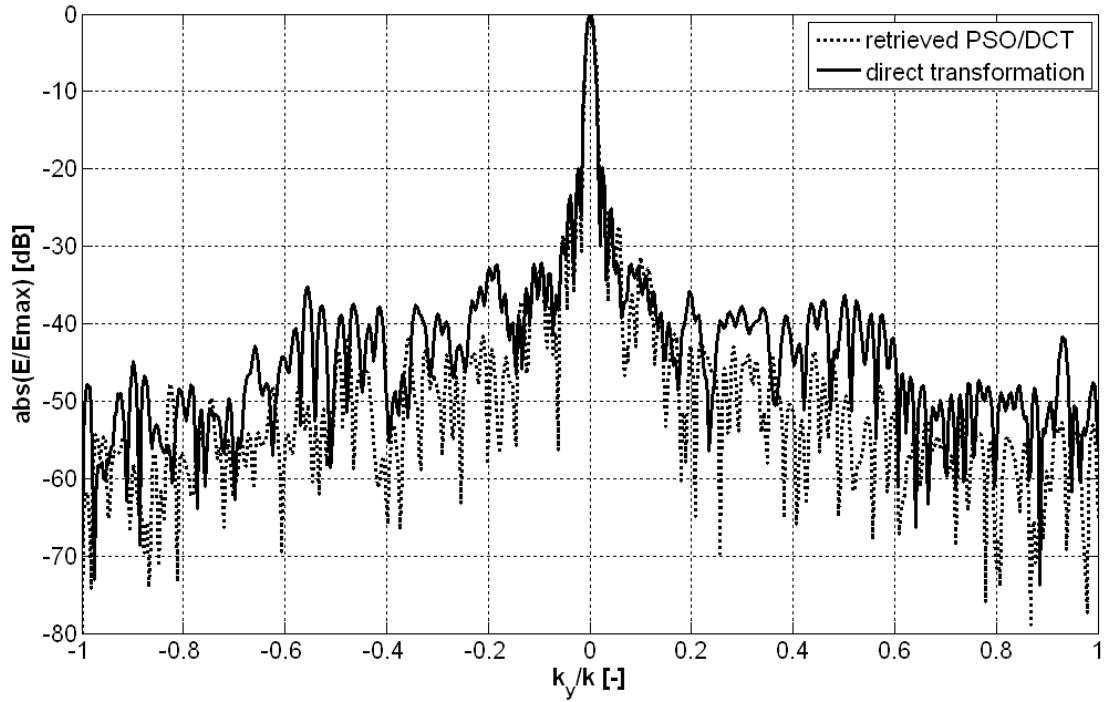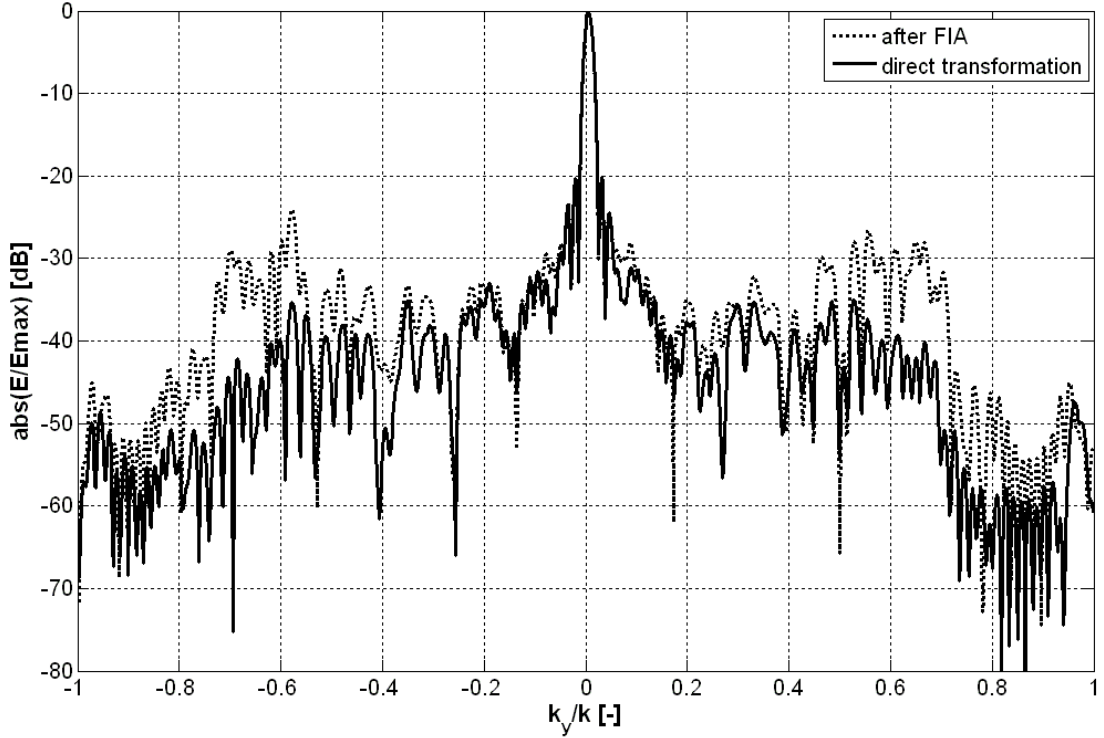
Fig. 3.62 Initial reconstruction of E plane radiation pattern of the lens antenna and comparison with radiation pattern obtained from measured complex near field
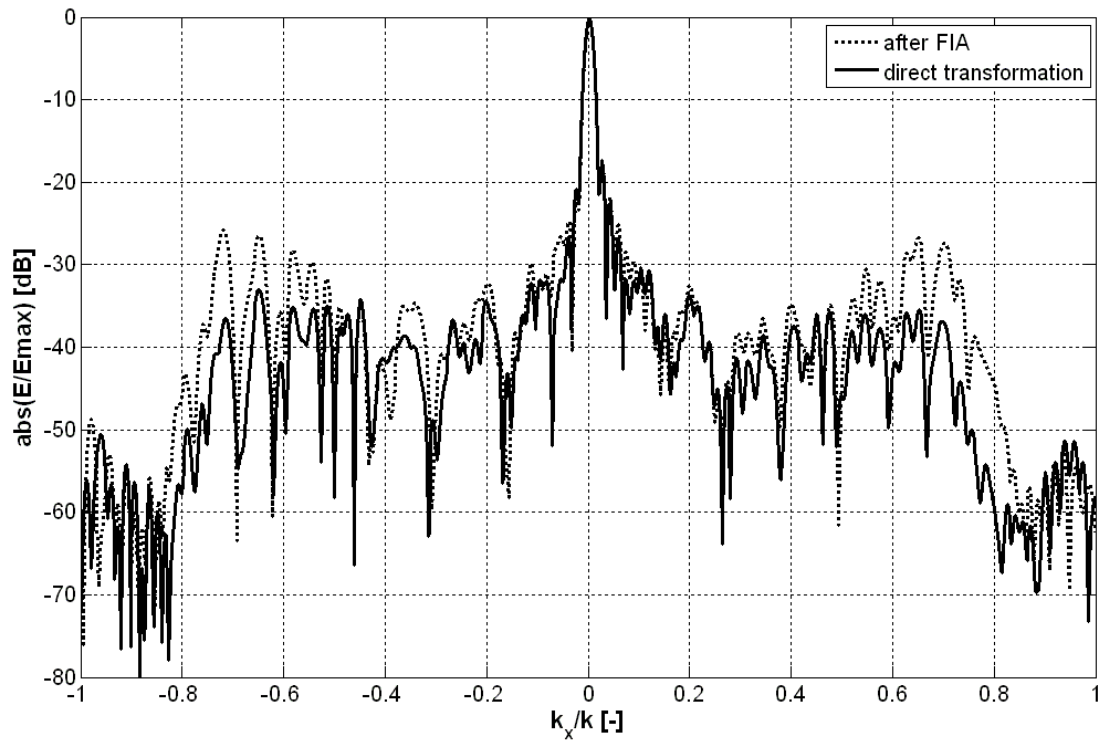
Fig. 3.63 Reconstructed H plane radiation pattern of the lens antenna and comparison with radiation pattern obtained from measured complex near field

Fig. 3.64 Reconstructed E plane radiation pattern of the lens antenna and comparison with radiation pattern obtained from measured complex near field

The novel near-field phaseless approach for the antenna far-field characterization was presented in this chapter. The method combines the global optimization, the compression method and the local method in conjunction with conventional two-plane amplitude measurements. The global optimization method is used to minimize the functional, the compression method is used to reduce the number of unknown variables, and the FIA is used to improve the estimate achieved by GO/CoM.

The proposed algorithm is very robust and faster than minimization algorithms published so far. The algorithm does not require any initial guess in the region of the global minima or any additional information about the AUT. Initial estimate is obtained very quickly in a few tens of iterations. The described algorithm was applied for the phase reconstruction of two electrically large antennas (dish antenna and lens antenna). The accuracy of the far-field patterns obtained by the novel phase retrieval algorithm is comparable with other minimization methods.

3.4 Possibility of single amplitude measurements

The classic minimization methods are based on the minimization of the difference between the calculated amplitudes and the measured ones on two plane surfaces (or on a single surface with two different probes) in the near field region. In this section of the thesis, the possibility of using amplitudes from only one scanning plane in functional based method is discussed and compared with two-plane algorithm.

3.4.1 Single-plane functional based algorithm

The principle of this method is the same as of the previous ones and exploits combination of the global technique with local one. Since only one set of the measured amplitudes is used, the minimization process is simplified and speeds up compared with the two-plane algorithm. The single-plane algorithm of the functional minimization assumes knowledge of the amplitudes on one plane, scanning plane distance from the AUT and dimensions of the AUT (shown in Fig. 3.65).
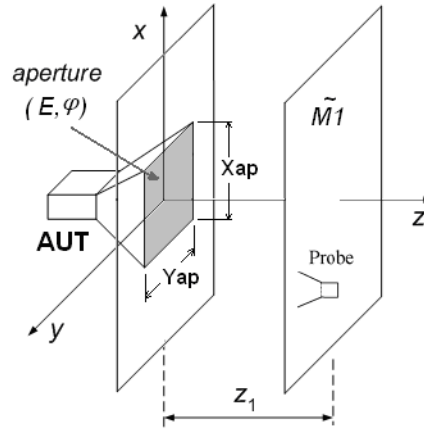

Fig. 3.65 Principle of the single-plane minimization method

The flow chart of the first part of the algorithm is shown in Fig. 3.66. First, random initial estimate of the DCT coefficients is performed. After the inverse DCT, we obtain electric field distribution on the antenna aperture. This distribution is completed symmetrically with zeros to the sample number of the amplitude distribution in the scanning plane. PWS is computed from the electric field distribution by 2D FFT and moved to the scanning plane by the propagation constant. After applying 2D FFT^{-1}, the electric field distribution is obtained back and fitness function (3.7) is calculated.

In the next phase, the initial estimate obtained by global optimization is improved by the simple iterative algorithm minimizing the same functional (3.7) and using also the amplitudes from a single plane. The flow chart is depicted in Fig. 3.67.

Iterative scheme begins from the initial estimate of the electric field distribution on the measured antenna aperture obtained by the minimization method. Zero padding to the sample number of the amplitude distribution in the scanning plane is performed. The PWS is computed and transformed by propagation to the distance of the scanning plane. The electric field distribution is obtained back and fitness function is calculated from the extracted amplitude and the measured one. If the condition is not satisfied, calculated amplitudes $|E1|^2$ are replaced by measured ones and complex electric field distribution is moved back to the plane of the aperture where the aperture constraint is applied. This way, the initial estimate is refined in every step. The whole cyclus is finished if the difference between the actual value and the previous one is smaller than the defined value or if the difference between the measured amplitudes and the estimated ones is better than the required accuracy.
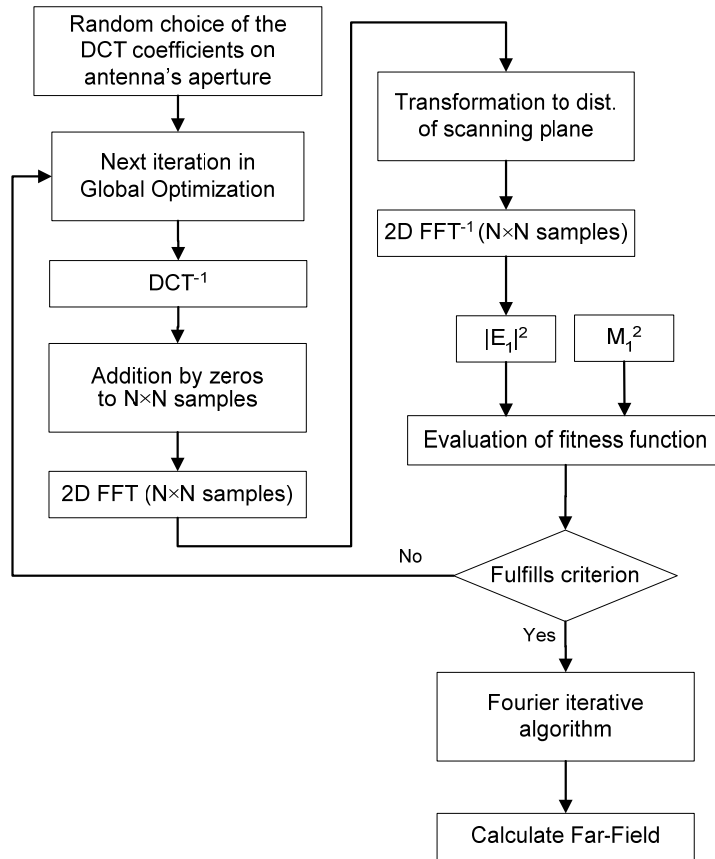
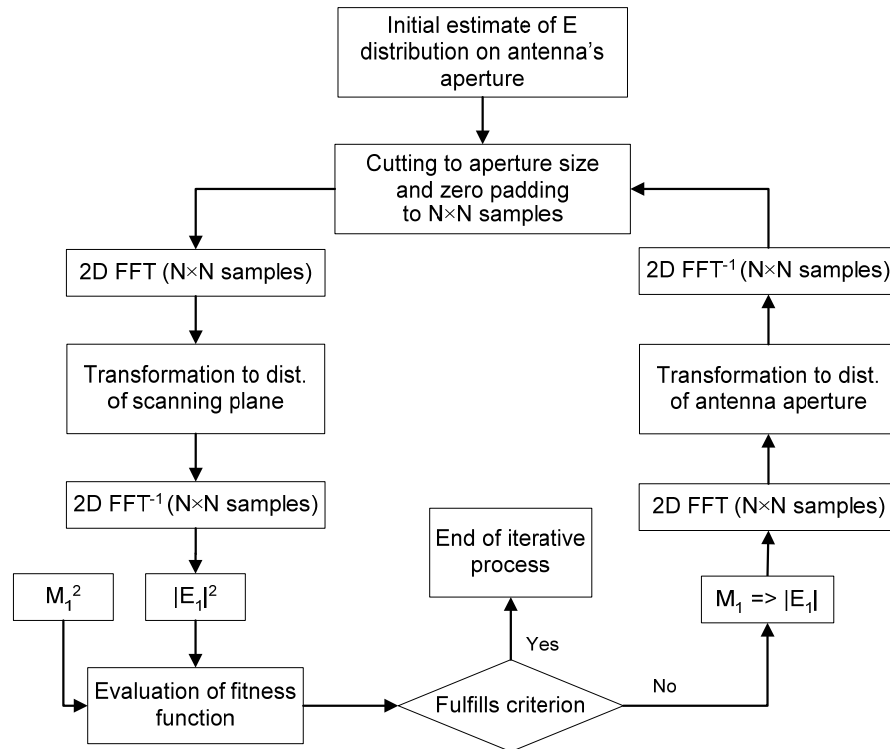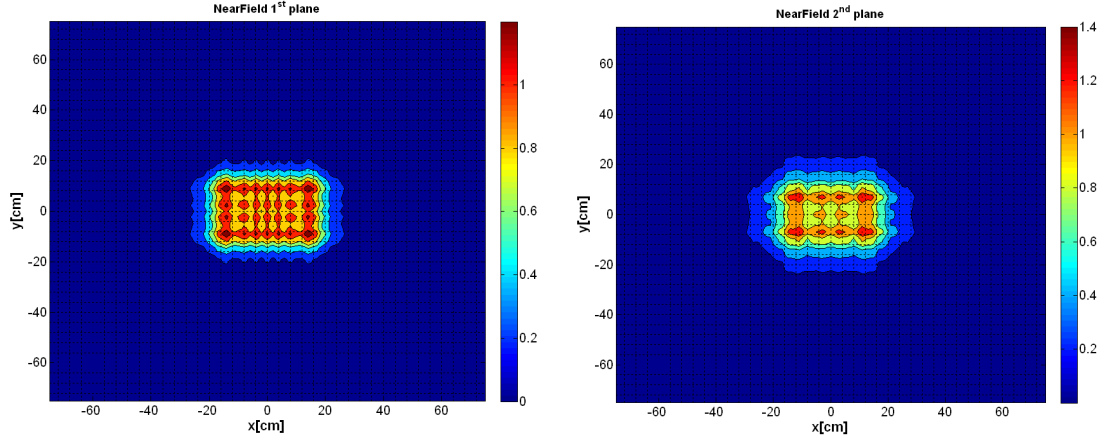**Fig. 3.66** Flow chart of the single plane minimization algorithm

Fig. 3.67 Single plane Fourier iterative algorithm.

3.4.2 Comparison of the single-plane and two-plane algorithms [63]

The comparison of the single-plane and two-plane algorithms is done on synthesized data of the antenna array (chapter 3.1.1). The contour plots of the near-field amplitudes are depicted in Fig. 3.68 for both scanning planes ($z_1 = 5\lambda$, $z_2 = 10\lambda$). In this case, solution space contains 1271 complex parameters defining the aperture field the optimal values of which have to be found out.

Fig. 3.68 Contour plot of the near-field amplitudes for both scanning planes; antenna array

The single-plane minimization algorithm exploiting a global optimization and compression method (Fig. 3.66) was used for initial reconstruction of the phases and amplitudes on the antenna aperture. Since we are looking for a rough estimate only which lies in the area of the global minimum only 18 coefficients of the DCT representing searched electric field on antenna aperture were optimized.

The far-field results obtained by this approach are shown in Fig. 3.69 and Fig. 3.70, dotted blue line. The estimate was obtained after 20 iterations of the minimization method. The agreement between the retrieved far-fields and the theoretical one is excellent in domain $\left| k_{x(y)} / k \right| = 0.2$ (main lobe and two side lobes).

Fig. 3.69 and Fig. 3.70 also show improved radiation patterns achieved after using one/two planes FIA. The reconstructed far-field of the antenna array shows that the FIA based on one plane amplitudes has achieved results with good accuracy but compared to the FIA based on two plane amplitudes, the accuracy is slightly worse.

Fig. 3.69 Reconstructed radiation patterns of the antenna array; E plane
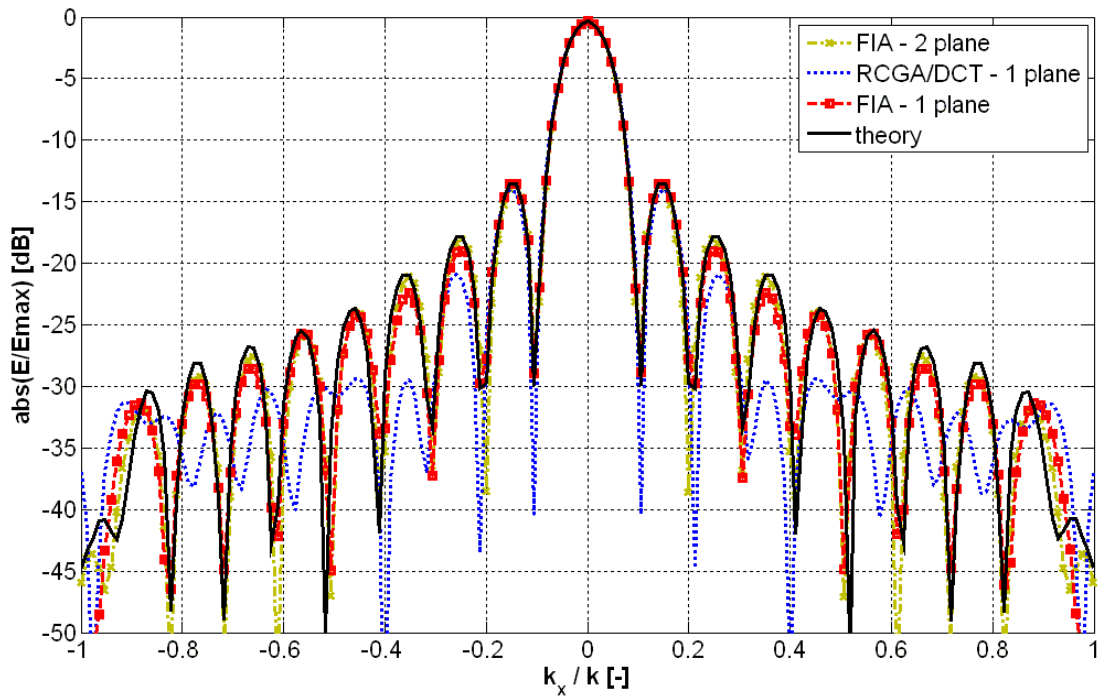
Fig. 3.70 Reconstructed radiation patterns of the antenna array; H plane

Far-field reconstruction of the phased antenna array where the aperture phase distribution is markedly non-uniform was also made for verification of these considerations. This phased antenna array has the same physical parameters as the previous antenna array but it differs in the feeding of individual elements. They are fed so that the phase is changed linearly along the axis x and y, the resulting phase change in the axis was equal to 65.3°. This resulted in a deflection of the main lobe in the

direction $\theta = 14°$ and $\phi = 14°$. Synthesized near-field amplitudes ($z_1 = 5\lambda$, $z_2 = 10\lambda$) are depicted in Fig. 3.71.
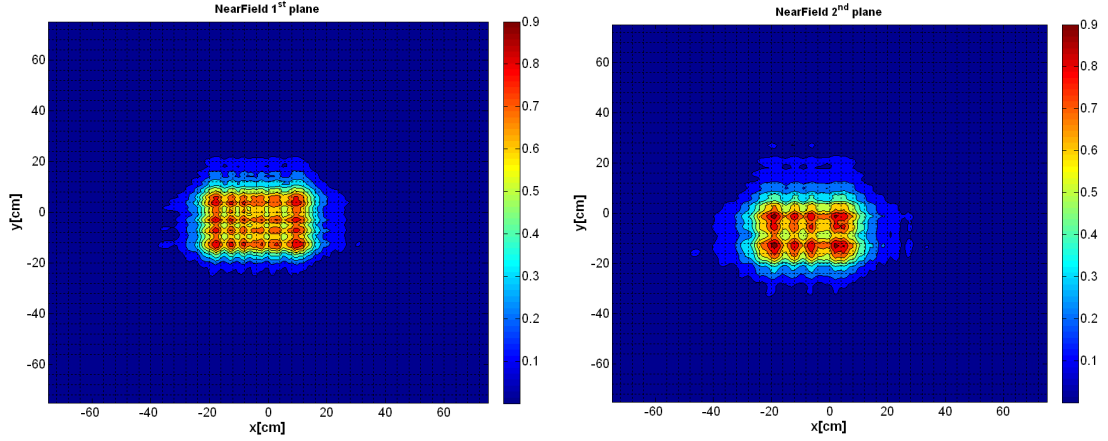
Fig. 3.71 Contour plot of the near-field amplitudes for both scanning planes; phased antenna array

Initial estimate was obtained by the RCGA/DCT method after 20 iterations, dotted blue line in Fig. 3.72 and Fig. 3.73. At first sight it may seem that the initial estimate does not lie in the global minimum area but the reconstructed far-field obtained after applying two-plane iterative algorithm proves the opposite, see Fig. 3.72 and Fig. 3.73. We can observe a good agreement with theoretical radiation pattern in this case. On the other hand, the single-plane FIA is not able to achieved results with required results.
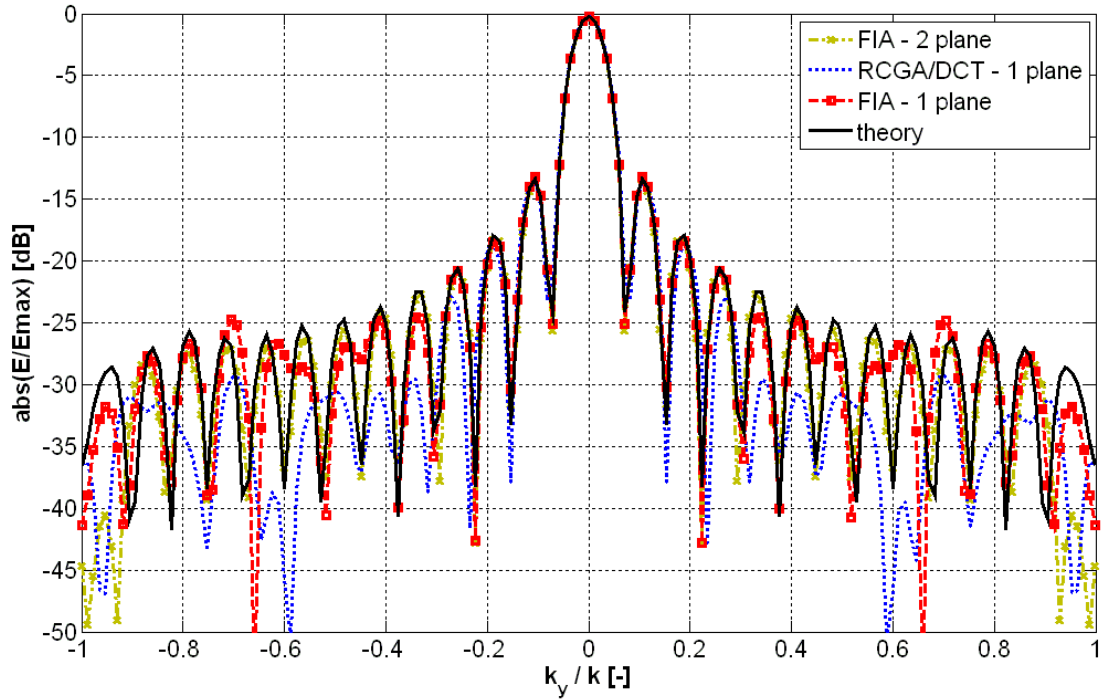

Fig. 3.72 Reconstructed radiation patterns of the phased antenna array; E plane

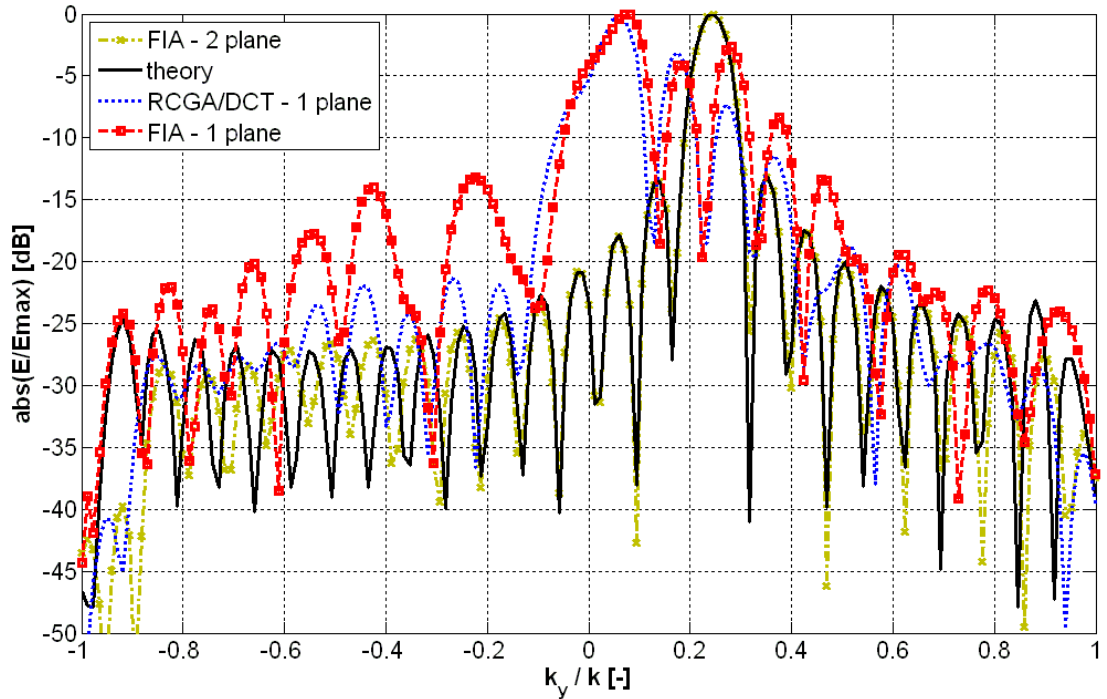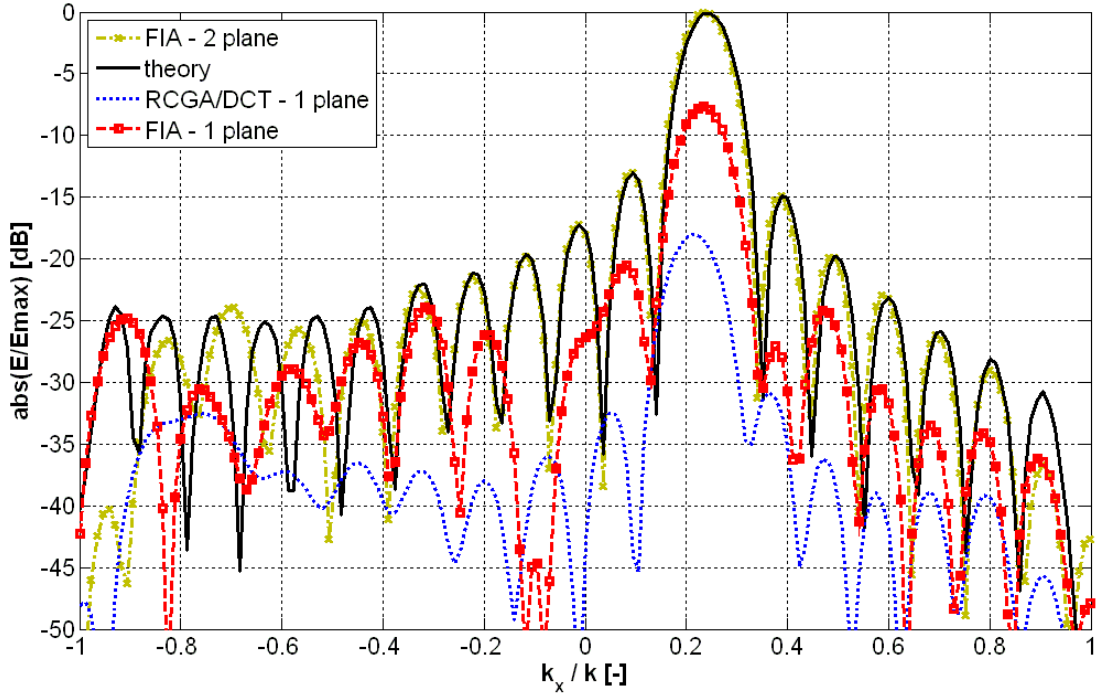**Fig. 3.73** Reconstructed radiation patterns of the phased antenna array; H plane

To conclude, the antenna pattern reconstructions of the antenna arrays confirm that the estimates obtained after 20 iterations of the minimization method (GO in combination with the DCT) are in the area of the global minimum and there is no risk that the subsequently used FIA gets stuck in a local minimum. Furthermore, it was found that knowledge of the amplitudes on one plane is sufficient for getting the initial estimate which lies in the global minimum area. Thus, the process of obtaining the initial estimate can be simplified and speeded up compared with the two-plane algorithm. These considerations were also confirmed for the phased antenna array. The single-plane FIA can be used only if the main lobe is perpendicular to the plane of the antenna, but radiation patterns obtained in this way are less accurate than the results of the two-plane algorithm.

The experimental verification of using amplitudes from one scanning plane in functional based method is also discussed in the next section where the designed algorithm is compared with other phase retrieval technique.

3.5 Comparison of GO/CoM/FIA method with others

There are several phase retrieval techniques which reconstruct the phase information from the knowledge of near-field amplitude over one or more testing surfaces; see chapter 1.2.2. Generally, two different approaches were developed: interferometric and functional.

In our case, the designed functional method is based on global optimization technique which is very robust when searching for the global minimum in a multidimensional domain. In contrast to the local minimization, use of the global algorithm is not conditioned by any choice of the initial estimates lying in the area of the global minimum and an additional modification of the minimized functional [23],

[25]. On the other hand, minimizing process is not able to reach precise results and also the convergence is relatively very slow. That is why the GO is completed by the DCT to reduce the number of unknown variables and decrease the computational efforts and also by the FIA for refinement of the obtained results [65]. Another difference is that only amplitudes collected on only a single surface are assumed.

A functional based method designed in this way will be compared with the hybrid method which stands at the top of the current phase retrieval techniques. Hybrid procedure for far-field reconstruction from phaseless near-field data was proposed by scientists from university of Calabria in 2005 exploiting the benefits of interferometric and functional methods [35]. Basically, the interferometric approach is adopted, but avoiding the use of a reference antenna as in standard interferometry. The phase reference is directly obtained from the field radiated by the AUT, which is collected by two probes on two different points along the scanning curve to interfere by means of a simple microstrip circuit [37]. The proposed methodology leads in principle to the evaluation of the near-field phase on the scanning surface from an inessential phase constant.

3.5.1   Hybrid technique

In principal, the hybrid approach is somewhere in between the interferometric techniques and the functional based ones. In particular, it exploits the interferometric approach for a notable reduction of the number of unknowns in the phase retrieval algorithm. Due to a lower number of unknowns, given by the phase shifts, the functional allows an accurate and fast convergence to the solution. Another important advantage of the proposed procedure is related to the absence of a reference antenna. This is due to two integrated probes in combination with a simple microstrip circuit used to perform near-field only-amplitude measurements, see Fig. 3.74. This gives a simpler and more compact measurement setup.
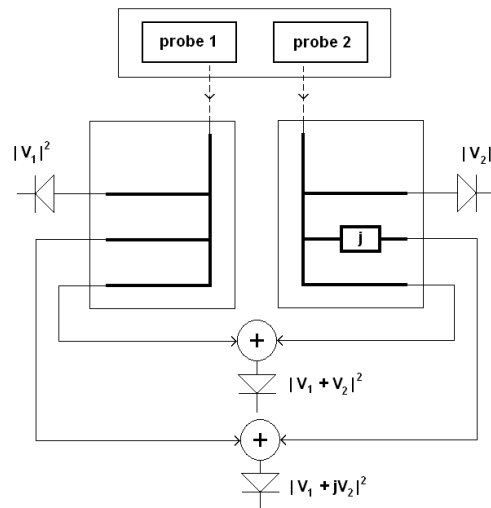
Fig. 3.74 Probe architecture

The architecture of the scanning probe allows the evaluation of the near-field phase (from a constant phase shifts) by an interferometric algorithm. The unknown phase shifts are subsequently computed by a minimization procedure involving only a

few unknowns and therefore requiring small computational effort. The algorithm block "j" represents the phase shift 90° in probe architecture.
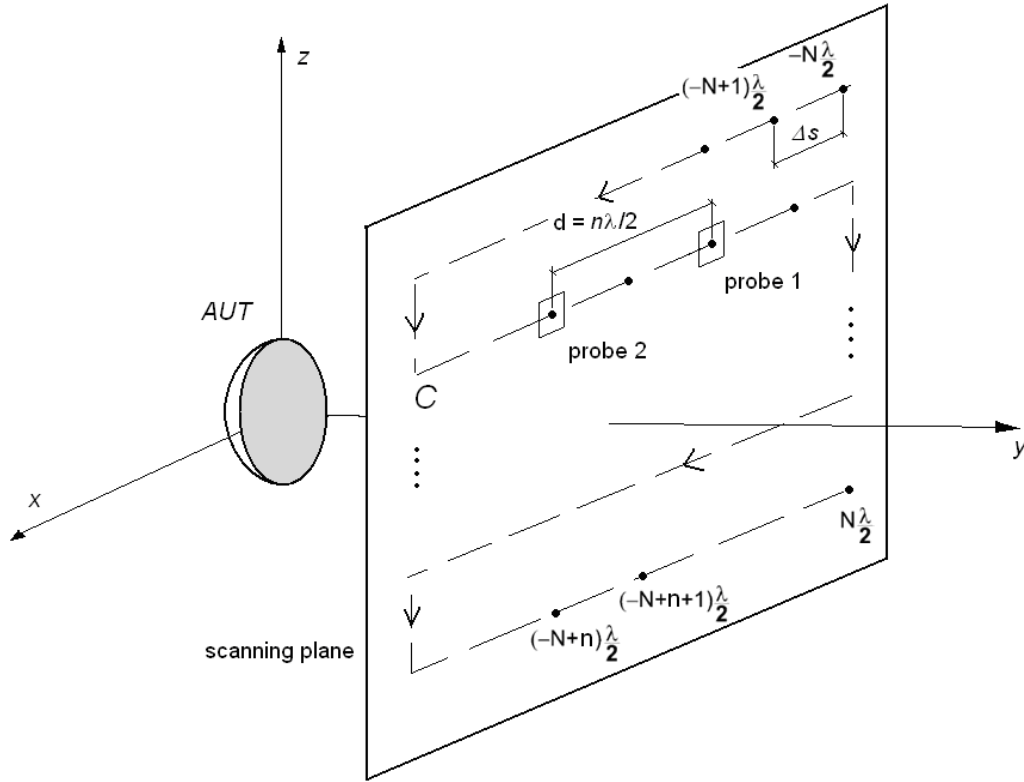
Fig. 3.75 Observation curve C for planar scanning geometry; Phase-shifts illustration for the case $n = 2$

Let us consider an observation curve C over planar scanning geometry (Fig. 3.75), with a sampling step $\Delta s = \lambda/2$ and a separation $d = n\lambda/2$ between two probes, being an integer greater than one. Amplitude data collected by the probes moving along the measurement curve are represented by four squared quantities (Fig. 3.74), namely [35]:

$$\left|V_1\right|^2, \ \left|V_1\right|^2, \ \left|V_1 + V_2\right|^2, \ \left|V_1 + jV_2\right|^2 \tag{3.13}$$

where

$$V_1 = \left|V_1\right| \cdot e^{j\varphi 1}, \quad V_2 = \left|V_2\right| \cdot e^{j\varphi 2}$$

are the complex signals obtained by the integrated probes along C. This information is used to retrieve the unknown phase shift by means of the interferometric formula [36]

$$\Delta\varphi = tg^{-1}\left[\frac{\left|V_1 + jV_2\right|^2 - \left|V_1\right|^2 - \left|V_2\right|^2}{\left|V_1 + V_2\right|^2 - \left|V_1\right|^2 - \left|V_2\right|^2}\right] \tag{3.14}$$

In Fig. 3.75, the *C* is the observation curve and parameter *s* denotes the curvilinear abscissa along *C*. The field radiated by the AUT on the observation curve C is following

$$E(s) = |E(s)| \cdot e^{j\varphi(s)} \tag{3.15}$$

Let us consider only one component of the field for purpose of simplicity and $2N + 1$ measurement points (N even) on the observation curve. After application of the formulas (2) we have the following sets of complex near-field data equal to n, namely

$$E(\Delta\varphi) = \begin{bmatrix} E(s_{(1)}), E(s_{(2)}) = \varepsilon(s_{(2)}) \cdot e^{j\Delta\varphi_1}, E(s_{(3)}) = \varepsilon(s_{(3)}) \cdot e^{j\Delta\varphi_2}, \\ \dots\ E(s_{(i)}) = \varepsilon(s_{(n)}) \cdot e^{j\Delta\varphi_{n-1}} \end{bmatrix} \tag{3.16}$$

where

$$s_{(1)} = \left[-N\lambda/2, (-N+n)\lambda/2, (-N+2n)\lambda/2, \dots\right],$$

$$s_{(2)} = \left[(-N+1)\lambda/2, (-N+n+1)\lambda/2, (-N+2n+1)\lambda/2, \dots\right], \dots$$

$$s_{(n)} = \left[(-N+n-1)\lambda/2, (-N+2n-1)\lambda/2, (-N+3n-1)\lambda/2, \dots\right].$$

where $\varepsilon(s_{(2)}), \varepsilon(s_{(3)}), \dots, \varepsilon(s_{(n)})$ are known quantities and phase shifts $\Delta\varphi_1, \Delta\varphi_2, \dots, \Delta\varphi_{n-1}$ are the unknowns to be determined, whose existence is related to the required distance $d = n\lambda/2$ between the probes. Fig. 3.75 illustrates the meaning of the above phase shifts for the case $n = 2$, which implies the existence of one unknown $\Delta\varphi_1 = \varphi(s_{(1)}^{(1)}) - \varphi(s_{(2)}^{(1)})$ where $\varphi(s_{(n)}^{(j)})$ refers to the phase value at position given by j-th element of set $s_{(n)}$. By changing the phase shift between the two sets of data $\Delta\varphi_1$, we obtain the set S_m of all the fields compatible with the measured data. Now consider the set S_A of all the fields that the AUT can radiate. The field radiated by the AUT is given by the intersection of the two sets, i.e. $S_m \cap S_A$ [35]. To obtain a successful procedure, the set S_A must be as small as possible: so we consider the reduced field $F(\xi) = E(\xi) \cdot e^{j\Psi(\xi)}$, obtained from the field $E(s)$ after extracting a proper phase function $\psi(\xi(s))$ and introducing a suitable parameterization $\xi(s)$ along the observation curve [46].

To conclude the considerations of the hybrid method, the main advantages are in measurement at a single surface and using a simple interferometric algorithm. The method also does not require any information about the AUT and mutual positions of the AUT and the probe. The disadvantage is in the necessity of a simple microstrip circuit for obtaining the necessary amplitude information. Concerning the functional based phase retrieval algorithm, the measurements on two surfaces are used in the proposed minimization method but the scanning approach can be replaced with another one where the amplitudes are measured by two different probes on the same testing surface. So we have the same situation as in the hybrid method. Moreover, the measurement performed on a single surface with a single probe is considered in the thesis. Measurement is then simplified and speeded up. The disadvantage is that this retrieved algorithm requires larger computational efforts than the simple interferometric algorithm. The dimensions of the AUT are also necessary for the algorithm to function properly.

The comparison of the two-plane and single-plane algorithms with the hybrid method is done in the next section. The comparison of the methods was carried out in collaboration with the Microwave Laboratory of the University of Calabria, Italy.

3.5.2 Comparison of the single-plane, two-plane functional methods and the hybrid method

The comparisons are carried out on the radiation pattern reconstruction of two different antenna types: horn antenna and dish antenna. The difference between these reconstructions is particularly in the number of the variables and far field radiation patterns. In case of the horn antenna, radiation pattern is less directional compared with the dish antenna which belongs among directional antennas.

The rectangular horn antenna has the aperture of the size 70×50 mm. The antenna was analyzed at the frequency 10 GHz. The horn antenna and the scanning probe (waveguide R100) were parallel to the horizontal plane (H polarization). The values of the horizontal electric field intensity component were scanned with the pitch of 15 mm (0.5λ) at two scanning planes of the size 1000 × 1000 mm placed in the distance of 200 mm and 400 mm. 4489 (67×67) values on each plane were obtained. With respect to the arrangement of the measurement, the valid angle is $\theta_v = \pm 50^o$. Since the aperture field of the antenna is searched for, the solution space contains only 40 real parameters.
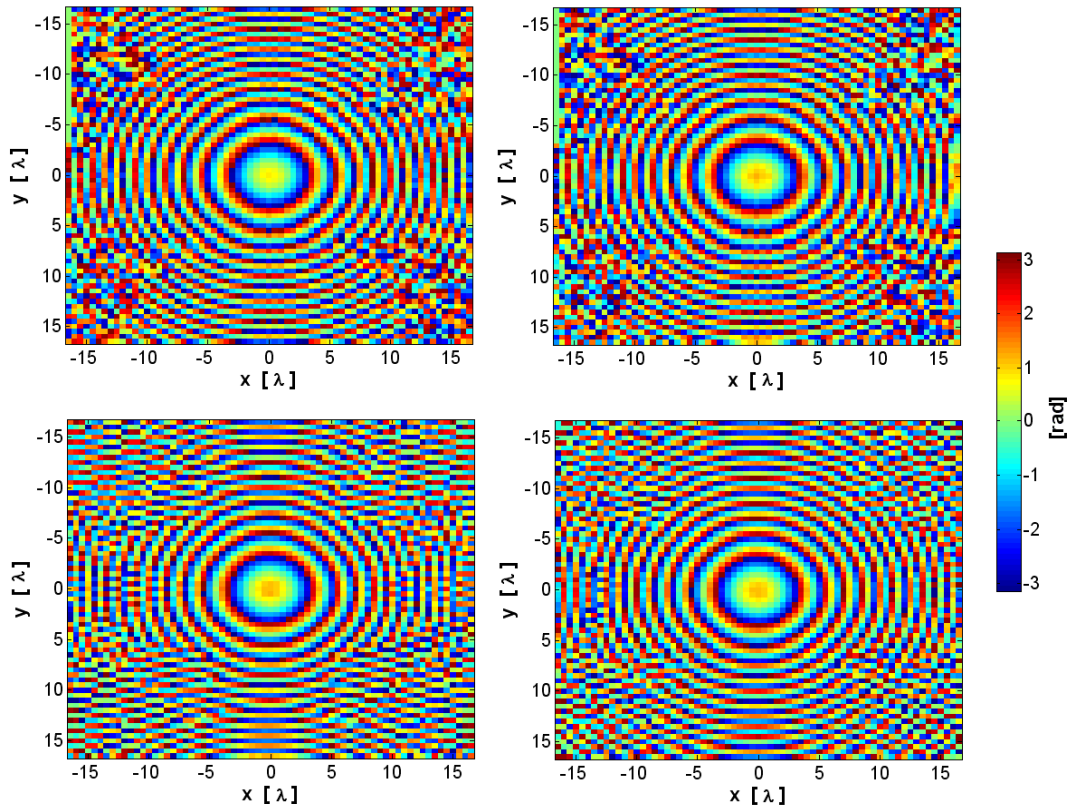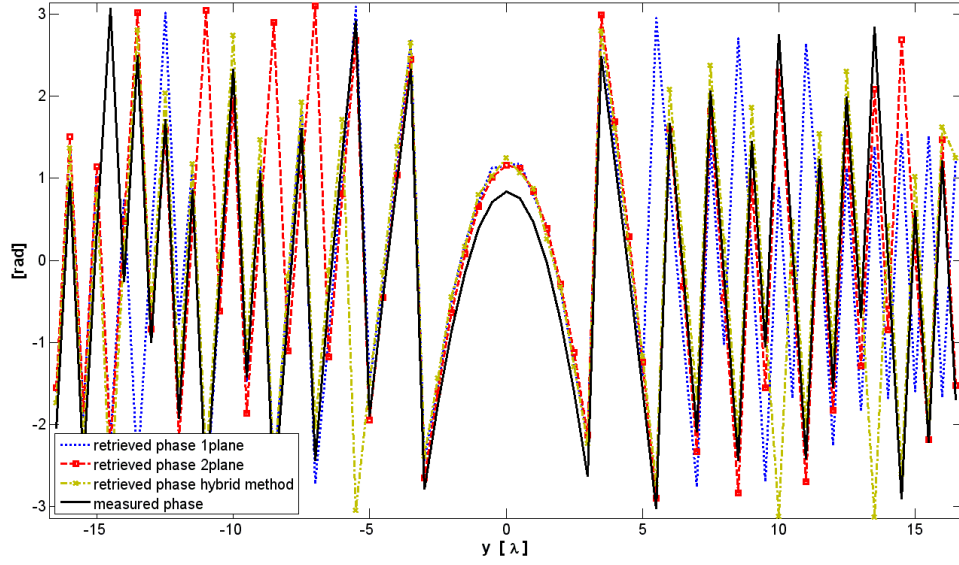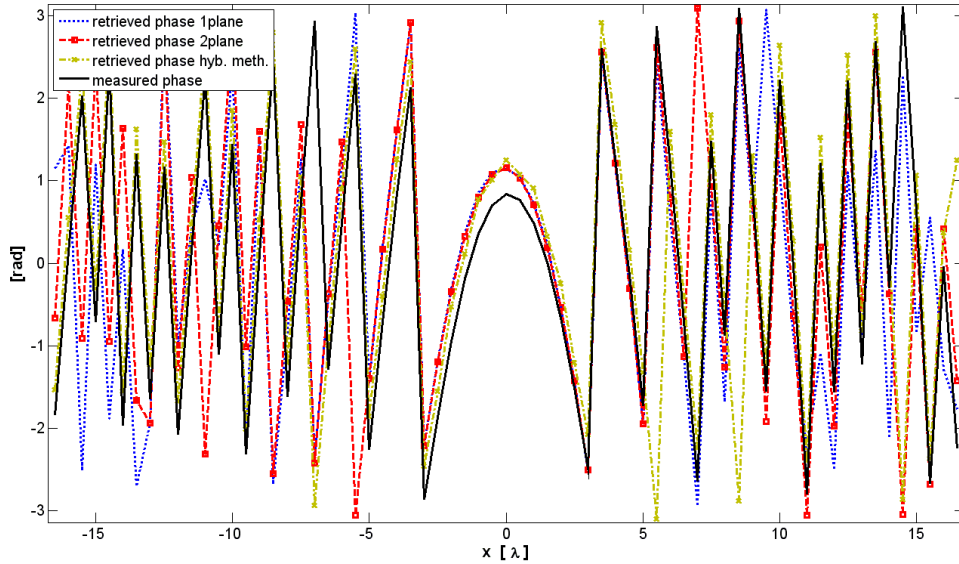

Fig. 3.76 Near-field phase on the first scanning plane; horn antenna:
Top: Left: The measured phase
             Right: The retrieved phase by hybrid method
Bottom: Left: The retrieved phase by single-plane functional methods
             Right: The retrieved phase by two-plane functional methods

Fig. 3.77 Comparison of exact and retrieved near-field phase in vertical cut

Fig. 3.78 Comparison of exact and retrieved near-field phase in horizontal cut

The contour plot of the near-field phase directly measured by the probe is reported in Fig. 3.76. The hybrid method and the single and two plane functional based phase retrieval algorithms, respectively, were applied to obtain the retrieved near-field phase, see also Fig. 3.76. The comparison of the retrieved phase with the exact one is also illustrated in Fig. 3.77 and Fig. 3.78 for main vertical cuts.

From the contour plots reported in Fig. 3.76 it can be easily observed that a good reconstruction is obtained in the central zone of the radiated field, where the signal to noise ratio is sufficiently large. But the results obtained by the hybrid method are more realistic because the method is even able to reconstruct the distortions in the corners of the scanning plane. If we compare the results obtained by the single-plane and the two-plane functional based methods, we can observe that accuracy of the retrieved phase is comparable. From the vertical cuts it can be observed that some retrieved phase points

differ from the measured points. But if we shift the differed values of phase of 360° the better agreement is obtained.
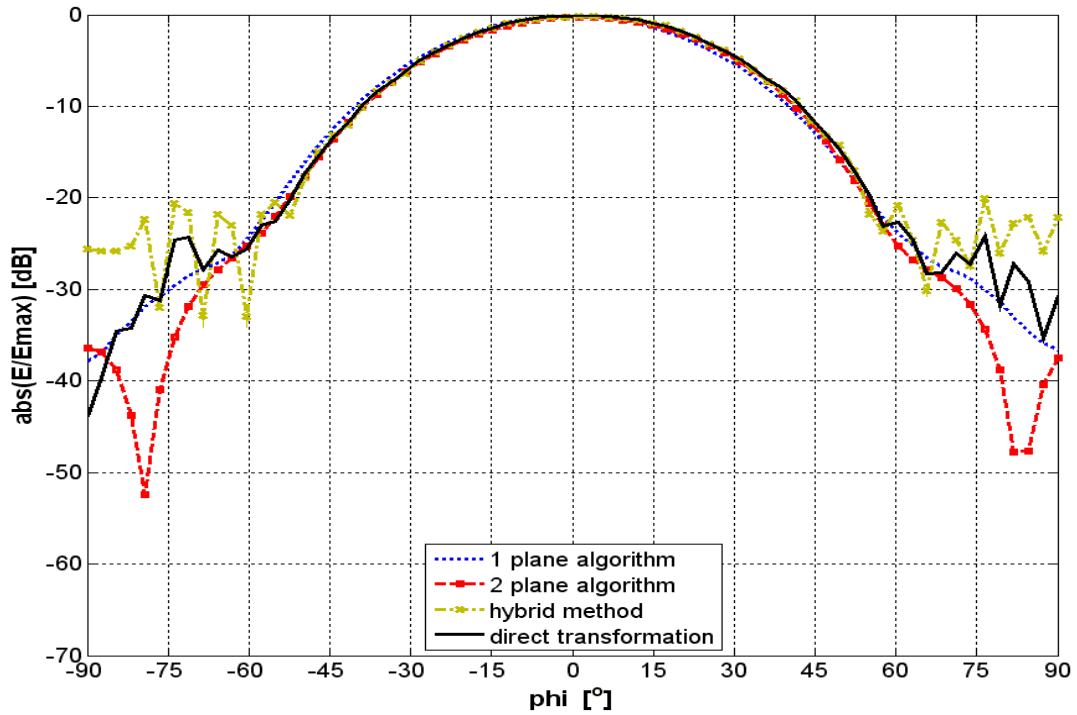

Fig. 3.79 Comparison of the far-field obtained from the accurate and retrieved near-field obtained by the compared methods; H plane
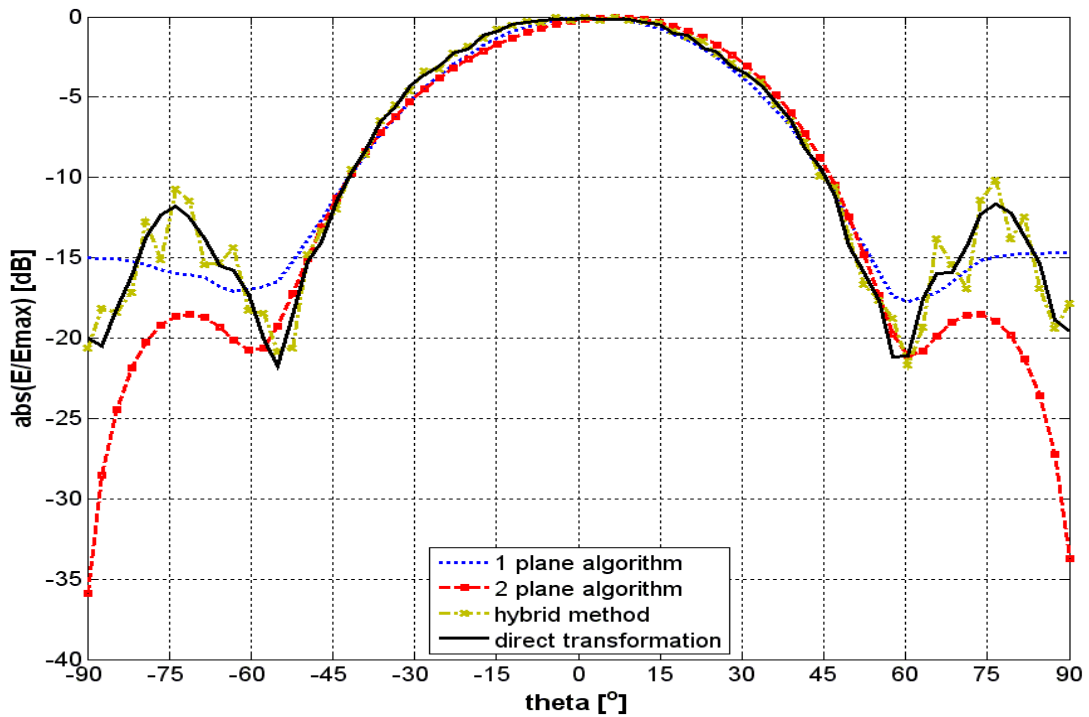

Fig. 3.80 Comparison of the far-field obtained from the accurate and retrieved near-field obtained by the compared methods; E plane

Both the retrieved and measured near-field phases were processed to obtain the radiated far-field. The agreement between the far-field obtained from the retrieved and directly measured near-field phase is shown in Fig. 3.79 for the H plane and in Fig. 3.80 for E plane. The valid angle is $\pm 50^\circ$. In this domain, a good agreement could be observed.

Due to the fact that accuracy of the functional method and hybrid phase retrieval algorithm depends on how accurately amplitude information is measured; we made error analysis to know how the methods are robust against the amplitude error. The samples of amplitude distribution were loaded by error with normal distribution in the range of 0-10 % of the maximum amplitude occurring in the scanning planes. The normal amplitude distribution and amplitude distribution loaded by error are depicted in Fig. 3.81.
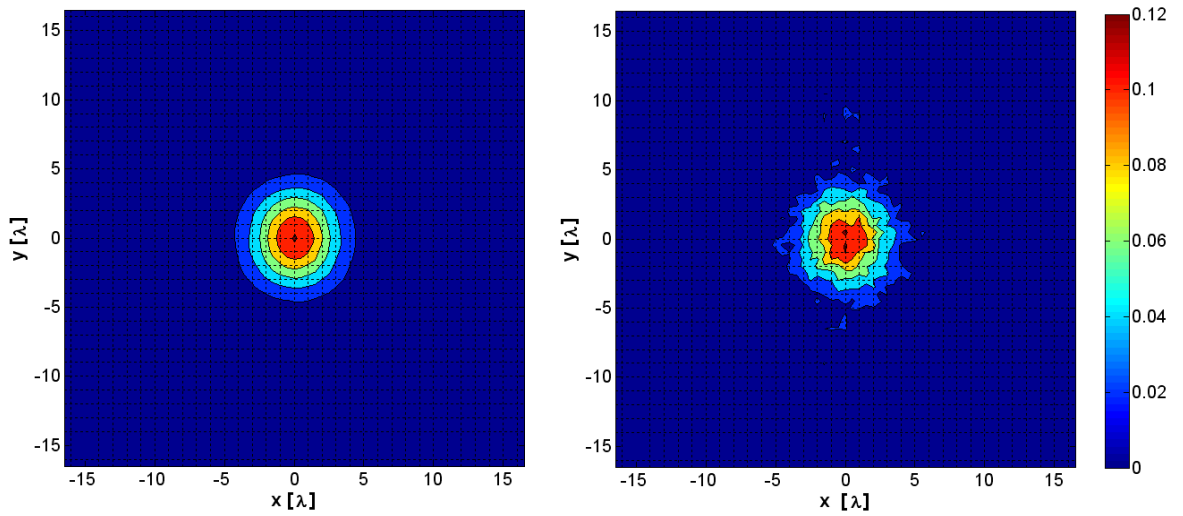

**Fig. 3.81** Normal amplitude distribution and amplitude distribution loaded by error on scanning plane

Fig. 3.82 shows a comparison of the reconstructed phase distributions obtained by individual methods. From the achieved results, the functional based methods seems to be more resistant than the hybrid method against the measured amplitude error and they are able to reconstruct the phase distribution from very strongly noise amplitudes, even when we used amplitudes from a single scanning plane.

Another error analysis was performed for functional based methods. Since functional based method requires the knowledge of the scanning plane distances from the measured antenna, the error analysis is focused on situations when the distance is not known exactly. Because there can be situations when the antenna is placed in a cover. The error distance of the first scanning plane was changed from $0 \div 25$ % of the exact value ($z_1 = 20$ cm) whereas the distance of the second plane was unchanged, see Fig. 3.83. For two cases of the shifts $dz = 2.5$ cm and 5 cm the radiation patterns are depicted in Fig. 3.84. In case of two-plane algorithm we can observe good agreement between the obtained radiation patterns and the accuracy radiation pattern. As it is obvious, the second plane can compensate the error caused by the first scanning plane. In case of the single-plane algorithm, the results are not in agreement. As was expected, with increasing distance of the scanning plane the main lobe of radiation pattern

becomes narrower. So, for the single-plane functional based algorithm we have to known the distance of the measured plane exactly.
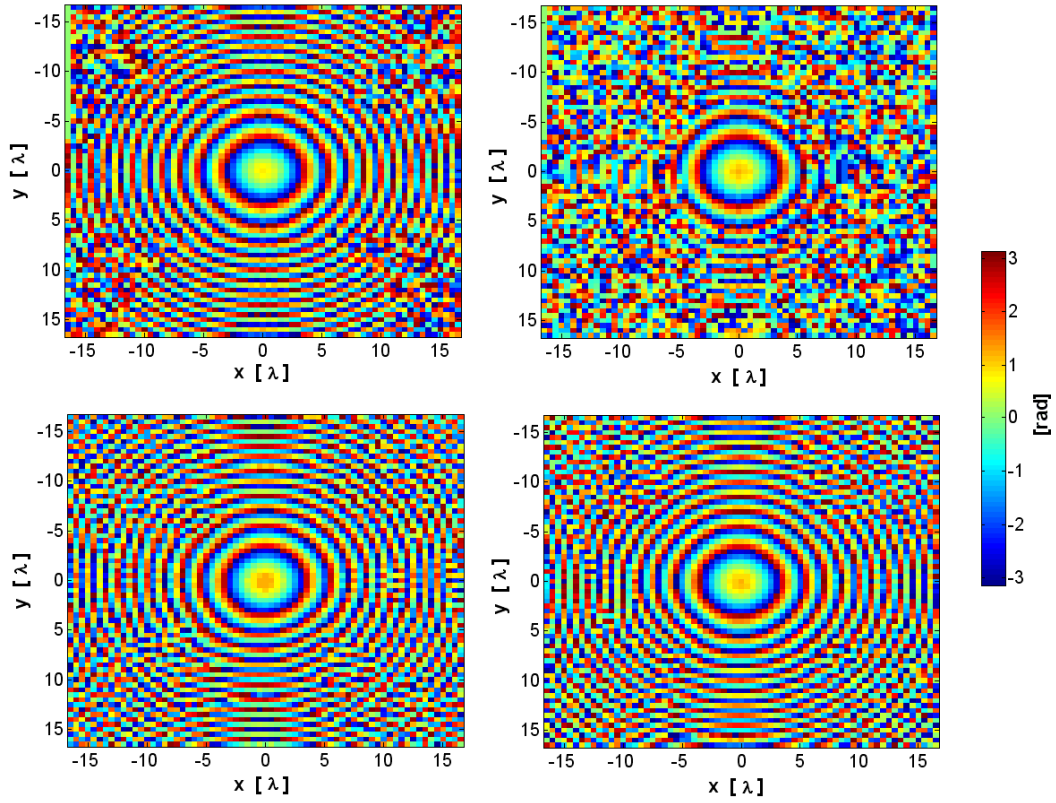
Fig. 3.82 Near-field phase on the first scanning plane reconstructed from amplitudes loaded by error;   Top: Left: The measured phase
Right: The retrieved phase by hybrid method
Bottom: Left: The retrieved phase by single-plane functional methods
Right: The retrieved phase by two-plane functional methods
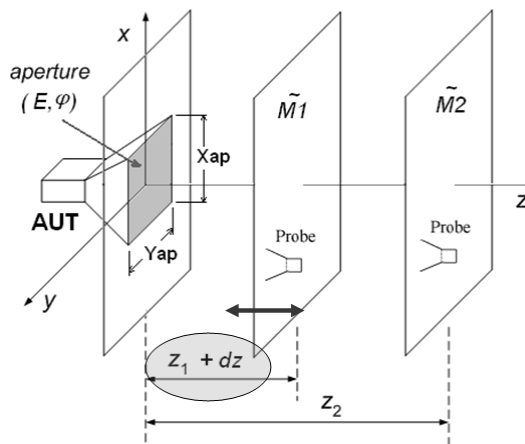
Fig. 3.83 Principle of the error analysis; the distance of the first scanning plane is changed
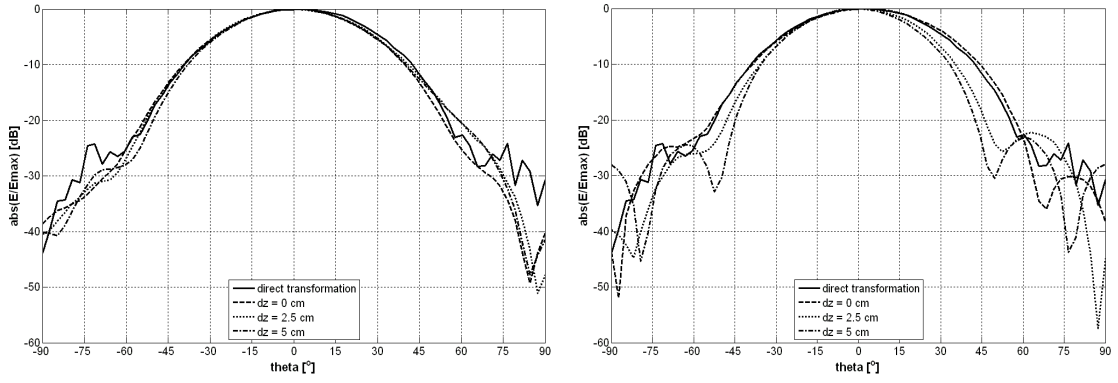
Fig. 3.84 Comparison of far-fields (only H plane) obtained by minimization method for different shifts of the first plane; Left: two-plane algorithm; Right: Single-plane algorithm

The phaseless near-field measurements have been performed also for another antenna type, the dish antenna. The dish antenna with reflector diameter of 0.34 m was analyzed also at the frequency 10 GHz. As the scanning probe the waveguide R100 was used. The distance between the scanning points was 15 mm (0.5λ) and scanning planes of the size 1000×1000 mm were measured in the distance of 200 mm and 400 mm. These distances correspond to the valid angle of $\theta_v = \pm 39.5^o$. 67×67 values on each plane were obtained. Since the aperture of the antenna has 340×340 mm (24 times 24 sampling points), the solution space contains 1 058 real parameters which optimal values are going to be found out.

The comparison of the retrieved phase with the measured one is illustrated in Fig. 3.85 – Fig. 3.87. As expected, excellent agreement is observed in case of the hybrid method which provided a more realistic reconstruction of the phase. For the functional based methods, the agreement between the retrieved phase and the measured one is not so excellent while the two-plane algorithm reached accurate results.

The retrieved near-field phases and the measured ones were used for calculation of the radiated far-field. The agreement between the far-field obtained from the retrieved and directly measured near-field phase is shown in Fig. 3.88 and 3.89. Good agreement in the range $\pm 60^o$ was achieved in case of the hybrid method and the two-plane functional method. For the single-plane minimization method, the agreement between the far-field obtained from the retrieved and directly measured phase is excellent only in the area of the main lobe. This implies that the single plane algorithm is able to reconstruct the radiation pattern only if the phase distribution varies very slowly in the antenna aperture, see central part of the phase distributions in Fig. 3.85. Thus, the single-plane algorithm can be used for antennas having complex electric field distribution on the aperture and radiation pattern perpendicular to scanning plane but the thus obtained radiation patterns are less accurate than in case of the two-plane functional method or the hybrid method.
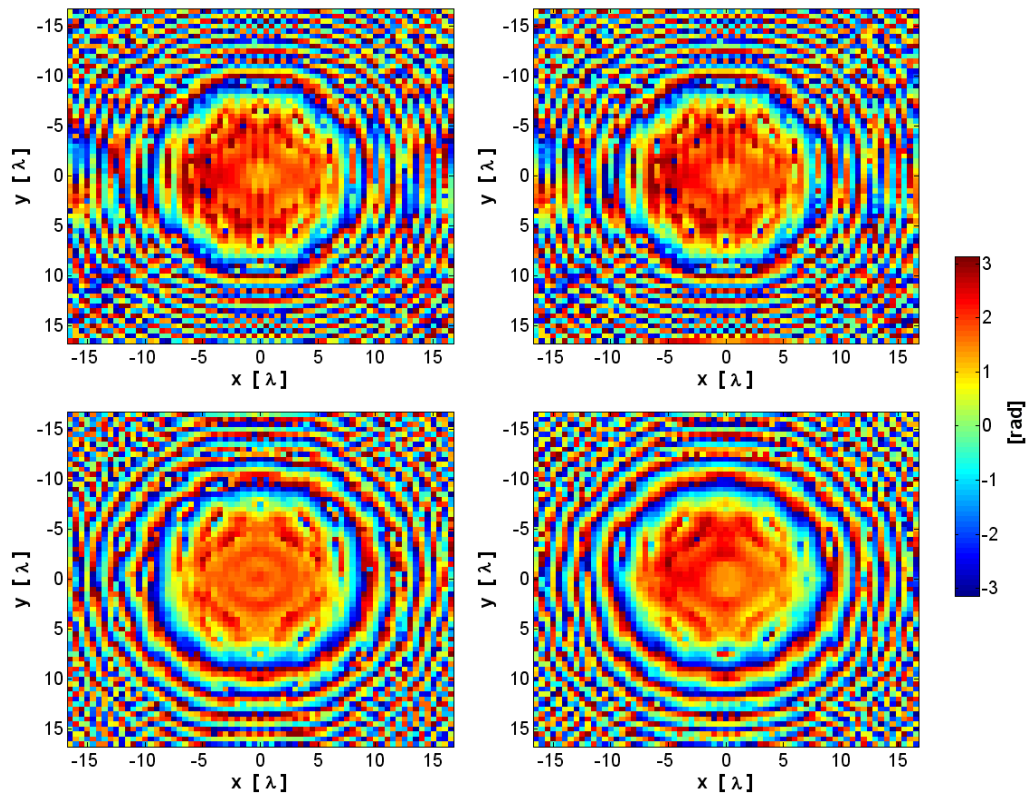
Fig. 3.85 Near-field phase on the first scanning plane; dish antenna:
  Top: Left: The measured phase
                Right: The retrieved phase by hybrid method
  Bottom: Left: The retrieved phase by single-plane functional methods
                Right: The retrieved phase by two-plane functional methods
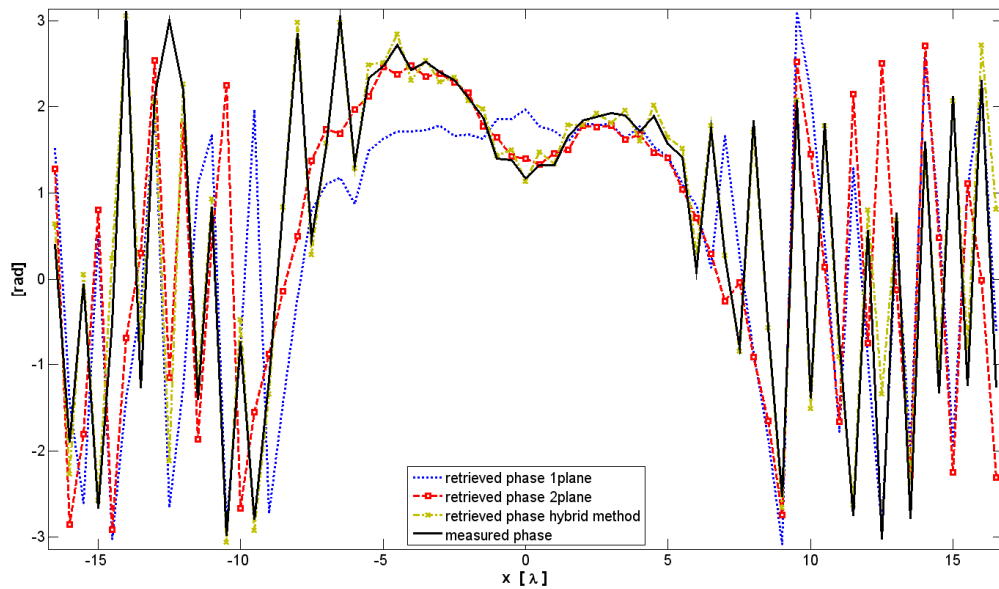
Fig. 3.86 Comparison of exact and retrieved near-field phase in horizontal cut
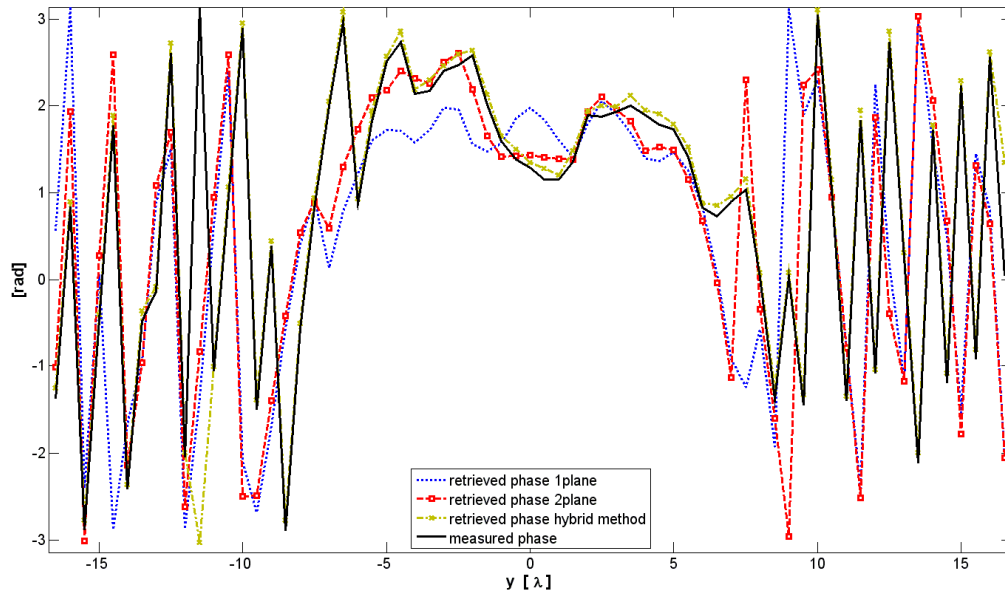
Fig. 3.87 Comparison of exact and retrieved near-field phase in vertical cut
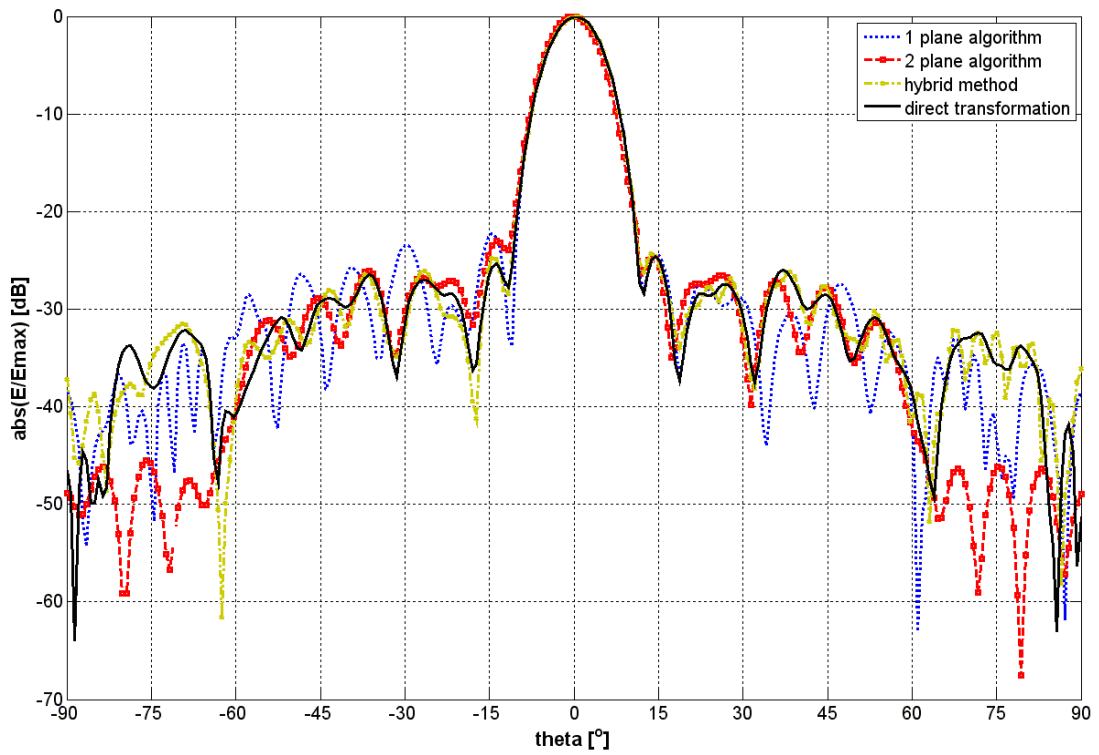
Fig. 3.88 Comparison of the dish antenna far-field obtained from the accurate and retrieved near-field obtained by the compared methods; E plane
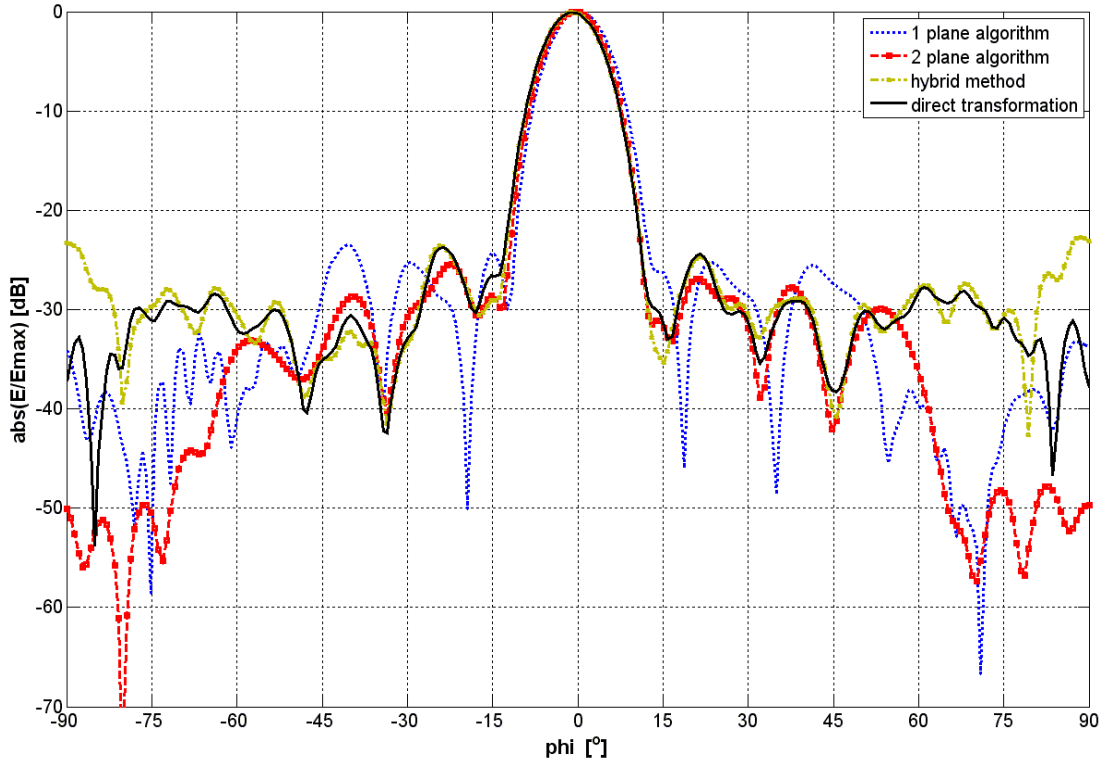
Fig. 3.89 Comparison of the dish antenna far-field obtained from the accurate and retrieved near-field obtained by the compared methods; H plane

To conclude, the phase reconstructions confirm good properties of the hybrid method which is able to reconstruct the phase with very high accuracy. On the other hand, the method could have a problem with phase reconstruction in case where amplitude information is measured with relatively high interferences.

For the functional based method, it was found out that accuracy of retrieved phase is worse than for the hybrid method, especially for the single plane algorithm when the antenna having complex electric field distribution on the antenna aperture is analyzed. Furthermore, it was found that accuracy of the single plane algorithm is sensitive to the distance of the measured plane which has to be known exactly. Contrasting with the hybrid method, the functional method is more robust and is able to reconstruct the phase information from very corrupted amplitude.

Comparing the functional methods, it was confirmed that knowledge of the amplitudes on one plane is sufficient for obtaining initial estimate lying in the global minimum. Thus, the process of obtaining the initial estimate can be simplified and speeds up compared with the two-plane algorithm. In the second part of the algorithm, in the iterative algorithm, using amplitudes from a single plane is possible and the accuracy of results is comparable with the algorithm using amplitude measurements over two planes but the quality of the results may depend strongly on the investigated antenna.

4 Application of the novel algorithm for cylindrical geometry

Planar NF/FF schemes have been the subject of the research in the previous part of the thesis. In this section, attention will paid to the application of the novel phase retrieval techniques for cylindrical geometry which is suitable mainly for antennas having a narrow pattern on one axis and a broad pattern on a second axis. The cylindrical measurements are more time-consuming than the planar one and from the mathematical point of view the cylindrical phase retrieval schemes are also more complicated for implementation.

4.1 Near-field cylindrical scanning

Knowledge of the electric field tangential components on an arbitrary surface, which, ideally, completely surrounds the measured antenna, allows calculating the field anywhere outside this surface, including in far region [11], [14]. However, the practical implementation of cylindrical scanning requires the scanning cylinder of final dimensions. Using the scanning cylinder of final dimensions carries an error in the calculated far field. The size of this error is dependent on the relative intensity of the field outside the scanning cylinder (i.e. on the size of the field, which is failure due to final scanning cylinder).

Suppose that the near field is measured on a scanning cylinder given by radius a. The minimum radius of the scan cylinder enclosing AUT must be greater than R_{min}, where R_{min} is the largest transverse dimension of the AUT in given cut (x or z). Thus, scanning of the antenna near-field is carried out in the interval of the distances R_{min} and $2D^2/\lambda$.

Cylindrical near-field scanning can provide complete angular coverage of the AUT field in horizontal plane but it is limited by the finite height of the cylinder in the vertical plane. There is a definition of the critical angle, which is graphically illustrated in Fig. 4.1 [4]. The size of the AUT and the size and location of the finite measurement area define the critical angle θ_{max}. The calculated far-field pattern of the antenna will be accurate in the region between $\pm\theta_{max}$. The size of the critical angle can be expressed as in the planar scanning by a simple empirical relationship [4]

$$\theta_{max} = \arctan\left(\frac{H - D - P}{2d}\right), \tag{4.1}$$

where d is the distance between AUT and probe, D and P are antenna height and probe height, respectively, and H is height of the scan cylinder. The formula (4.1) says that if we want to achieve a large critical angle, we must use very a high scanning cylinder located close to the measured antenna.
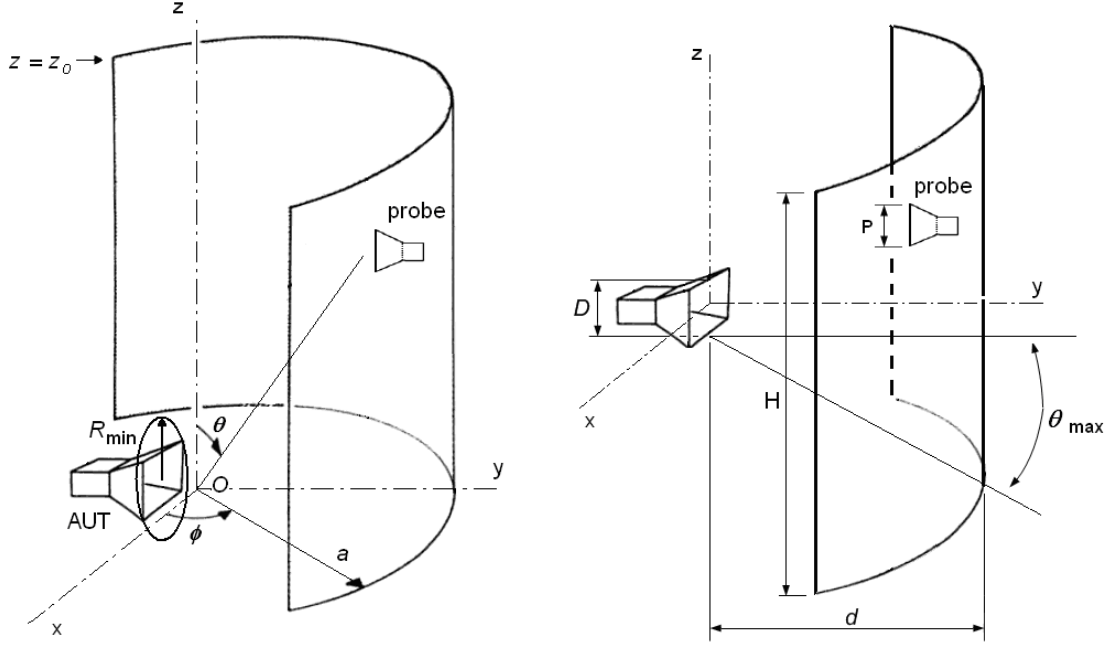
Fig. 4.1 Left: Geometric representation of the cylindrical scanning; Right: Determination of the valid angle θ_{max}

Transformation of the Near-field to Far-field [17], [18]

In this part, the basic formulas for computing the far field radiated by AUT from sampled values of near field on a scan cylinder were derived. The considered geometry of the NF cylindrical scanning is depicted in Fig.4.1. Consider for simplification that the scan cylinder is infinite, so that $z = \pm \infty$.

Both cylindrical and spherical coordinate systems, depending on the convenience, are adopted to describe the antenna near-field, while the spherical one is used in the far-field. As it is well-known, the tangential components $\mathbf{E}$ (E_z, E_ϕ) of the electric field, radiated by the AUT and measured on the cylinder, can be represented as a superposition of elementary cylindrical waves [11]. The FF spherical components of the electric field can be evaluated by:

$$\mathbf{E}(r,\theta,\phi) \approx -\frac{2k\sin\theta \cdot e^{jkr}}{r} \sum_{n=-\infty}^{+\infty} e^{jn\phi} \cdot e^{-j\pi(n+1)/2} \times \left[jA_n(k\cos\theta)\hat{\phi} + B_n(k\cos\theta)\hat{\theta} \right]$$

(4.2)

where k is the wave number and

$$\hat{\phi} = -\hat{\mathbf{x}}\sin\phi + \hat{\mathbf{y}}\cos\phi$$

$$\hat{\theta} = \hat{\mathbf{x}}\cos\theta\cos\phi + \hat{\mathbf{y}}\cos\theta\sin\phi - \hat{\mathbf{z}}\sin\theta$$

(4.3)

are unit vectors for the spherical coordinate system. The modal coefficients (spectra) $A_n(k_z)$ and $B_n(k_z)$ can be expressed in terms of the tangential electric field on the scan cylinder as

$$A_n(k_z) = -\frac{1}{4\pi^2 k_\rho \frac{\partial}{\partial(k_\rho a)} H_n^{(1)}(k_\rho a)} \times \int\limits_{-\infty}^{+\infty}\int\limits_{0}^{2\pi} E_\phi(a,\phi,z)e^{-jn\phi}e^{-jk_z z}\,d\phi dz$$

$$-\frac{nk_z}{4\pi^2 a k_\rho^3 \frac{\partial}{\partial(k_\rho a)} H_n^{(1)}(k_\rho a)} \times \int\limits_{-\infty}^{+\infty}\int\limits_{0}^{2\pi} E_z(a,\phi,z)e^{-jn\phi}e^{-jk_z z}\,d\phi dz, \quad a > R_{min}$$

(4.4)

and

$$B_n(k_z) = \frac{k}{4\pi^2 k_\rho^2 H_n^{(1)}(k_\rho a)} \times \int\limits_{-\infty}^{+\infty}\int\limits_{0}^{2\pi} E_z(a,\phi,z)e^{-jn\phi}e^{-jk_z z}\,d\phi dz, \quad a > R_{min} \qquad (4.5)$$

where $H_n^{(1)}$ is the Hankel function of the first kind and order n with $k_\rho = \sqrt{k^2 - k_z^2}$; $k_z = k\cos\theta$. The formulas (4.2), (4.4), and (4.5) have been derived previously in [13]. Similarly, if we know only magnetic field the expansion coefficients can be also expressed in terms of the tangential magnetic field [18].

The formulas (4.4) and (4.5) apply if the field on the scan cylinder is measured with an ideal electric dipole oriented along the z and ϕ directions. Even though the radius a of the scan cylinder appears on the right-hand side of the expressions for the modal coefficients $A_n(k_z)$ and $B_n(k_z)$, the expansion coefficients themselves are independent of a.

The formulas (4.4) and (4.5) for the modal coefficients involve an integration over an infinite scan cylinder that extends all the way from $z = -\infty$ to $z = +\infty$ and covers the entire angular region $0 \le \phi < 2\pi$. Let us write this integral as

$$F_n(k_z) = \int\limits_{-\infty}^{+\infty}\int\limits_{0}^{2\pi} \Psi(a,\phi,z)e^{-jn\phi}e^{-jk_z z}\,d\phi dz \qquad (4.6)$$

where $\Psi(a,\phi,z)$ is one of the tangential field components. In practical near-field measurements, the field is measured only on a truncated scan cylinder, which is assumed from $z = -z_0$ to $z = +z_0$ where z_0 is a positive height. Moreover, only a limited angular region $\phi_0 \le \phi < 2\pi - \phi_0$ can be covered by the scan. Typically, the field outside the scanned area is neglected and the exact expression for the spectrum is approximated by

$$F_n(k_z) = \int\limits_{-z_o}^{z_o}\int\limits_{\phi_o}^{2\pi-\phi_o} \Psi(a,\phi,z)e^{-jn\phi}e^{-jk_z z}\,d\phi dz \qquad (4.7)$$

Thus, it is assumed that the contribution to the integral (4.7) from the region not covered by the scan is negligible. For cylindrical near-field measurements of antennas this assumption is often valid because the measurements are set up so that very little energy is radiated in directions not covered by the finite scan cylinder.

Sampling Theorem and Computation Scheme

The derived formulas for the far field involve integrations of the field over the scan cylinder and infinite summations over angular region. In this section, these formulas were discretized so that the far field of the AUT can be computed from a finite number of field values sampled at regular intervals on the scan cylinder. As part of the discretization, we present sampling theorems that determine the sample spacing required for accurate far-field calculation.

The scan cylinder is truncated and put in cylindrical coordinates by $\rho = a$ and $|z| \le z_0$, and the field on the scan cylinder is measured at the grid points expressed in terms of the cylindrical coordinates as $\phi = (p - 1)\Delta\phi$, $p = 1, 2, \ldots, N_\phi$ and $z = (q - 1)\Delta z - z_0$, $q = 1, 2, \ldots, N_z$. The formulas of this section require field measurements for the entire 360° range. If the scan cylinder is angularly truncated, zeros are simply inserted into the array positions that correspond to measurement points that are outside the scanned area. Note that z_0 satisfies the relation $z_0 = (N_z - 1)\Delta z/2$.

If every point on the scan cylinder is at least one wavelength or so away from the nearest point on the AUT [16], the sampling intervals can be chosen as follows [15]:

$$\Delta\phi = \frac{2\pi}{N_\phi}, \qquad N_\phi = 2\,\mathrm{int}\big(kR_{\min} + n_1\big), \qquad \Delta z = \frac{\lambda}{2} \qquad\qquad (4.8a, 4.8b)$$

where $R_{\min}$ is the radius of the minimum cylinder, n_1 is a small integer, and λ is the wavelength. In (4.8) the function "int" denotes the integer value.

The sampling theorem [15] also shows that the infinite summation in the far-field formula (4.2) can be replaced by the finite summation that extends from $n = -N_\phi/2$ to $n = N_\phi/2$. Further, the two-dimensional array Ψ_{pq} which contains the field values $\Psi(a, \phi, z)$ at the ϕ–z grid points is introduced. A straightforward discretization of the formula (4.7) for the spectrum then gives

$$F_n\big(k_z\big) = \Delta z \Delta\phi.e^{jk_z z_o} \sum_{p=1}^{N_\phi} \sum_{q=1}^{N_z} e^{-jn\Delta\phi(p-1)} e^{-jk_z\Delta z(q-1)} \Psi_{pq}\,. \qquad\qquad (4.9)$$

Note that both the far-field formula (4.2) and the formula (4.9) for the spectrum can be computed efficiently with the FFT.

Near-field to Near-field transformation [19]

Let us denote by $\mathbf{E} = (E_1, E_2)$ the complex tangential near field distribution over the first surface by a source of finite extension. A dyadic linear operator $\mathbf{T}$ with components

$$\mathbf{T} = \begin{bmatrix} T_{11} & T_{12} \\ T_{21} & T_{22} \end{bmatrix} \qquad\qquad (4.10)$$

connects $\mathbf{E}$ to the corresponding tangential near field components over the second surface.
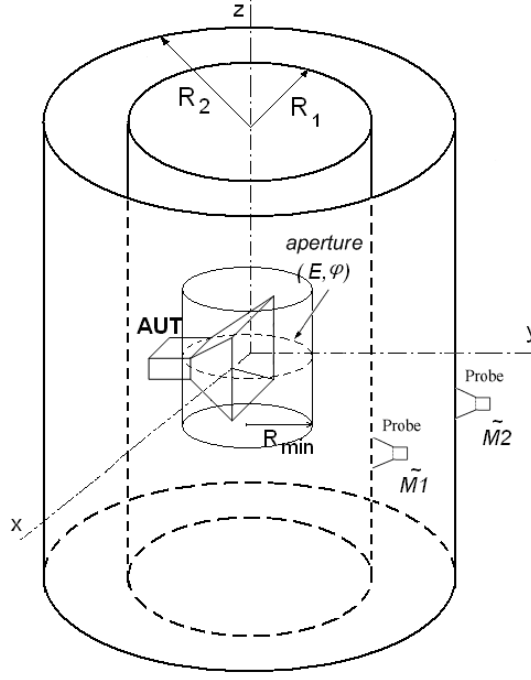
Fig. 4.2   Relevant to scanning geometry

For the cylindrical geometry, the field components to be considered are the ones tangential to the cylindrical scanning surface that is the one along the z axis and the one along the ϕ versor (see Fig. 4.2). Adopting the cylindrical vector wave expansion for the near field on each surface, the operator **T** can be written as

$$\mathbf{T} = F_\phi^{-1} F_z \cdot \mathbf{H} \cdot F_z^{-1} F_\phi \tag{4.11}$$

where F_z is the Fourier transform in the z variable, that is

$$F_z : g \in L^2(-\infty, +\infty) \Rightarrow F_z = \frac{1}{2\pi} \int_{-\infty}^{+\infty} g(z) \cdot e^{-jhz} \, dz \in L^2(-\infty, +\infty) \tag{4.12}$$

and F_ϕ is the Fourier series operator in the ϕ variable, that is

$$F_\phi : g \in L^2(-\pi, +\pi) \Rightarrow F_\phi = \frac{1}{2\pi} \int_{-\pi}^{+\pi} g(\phi) \cdot e^{-jn\phi} \, d\phi \in l^2 \tag{4.13}$$

With $L^2(., .)$ and l^2, respectively denoting the spaces of functions square integrable over the corresponding domain and the space of square summable sequences. Moreover, the matrix **H** of the function is given by

$$\begin{bmatrix} \dfrac{H_n(\chi R_2)}{H_n(\chi R_1)} & 0 \\[3mm] \dfrac{nh}{\chi^2}\left[-\dfrac{1}{R_1}\dfrac{H'_n(\chi R_2)}{H'_n(\chi R_1)} + \dfrac{1}{R_2}\dfrac{H_n(\chi R_2)}{H_n(\chi R_1)} \right] & \dfrac{H'_n(\chi R_2)}{H'_n(\chi R_1)} \end{bmatrix} \tag{4.14}$$

With $\chi = \sqrt{k^2 - h^2}$, $h = k \cdot \cos\theta$, $H_n(\cdot)$ is the Hankel function of order n, $H'_n(\chi R_i) = \partial H_n(\chi R_i)/\partial R_i$, $k = 2\pi/\lambda$ and R_1 and R_2 are the radii of the scanning cylinders.

From the matrix (4.14) it is clear that cylindrical field distributions $E_z(R,\phi,z)$ at two separate radii are related by the equation [2]

$$E_z(R_2,\phi,z) = \int\limits_{-\pi}^{+\pi}\int\limits_{-\infty}^{+\infty}\left\{\frac{1}{4\pi^2}\int\limits_{-\pi}^{+\pi}\int\limits_{-\infty}^{+\infty}E_z(R_1,\phi,z)\cdot e^{-jn\phi}\cdot e^{jhz}\,d\phi dz\right\}\times\frac{H_n^{(2)}(\chi R_2)}{H_n^{(2)}(\chi R_1)}\cdot e^{jn\phi}\cdot e^{-jhz}\,d\phi dz$$

(4.15)

and for the component $E_\phi(R,\phi,z)$

$$E_\phi(R_2,\phi,z) = \int\limits_{-\pi}^{+\pi}\int\limits_{-\infty}^{+\infty}\left\{\frac{1}{4\pi^2}\int\limits_{-\pi}^{+\pi}\int\limits_{-\infty}^{+\infty}E_z(R_1,\phi,z)\cdot e^{-jn\phi}\cdot e^{jhz}\,d\phi dz\right\}\times$$

$$\times\frac{nh}{\chi^2}\cdot\left[-\frac{1}{R_1}\frac{H_n'^{(2)}(\chi R_2)}{H_n'^{(2)}(\chi R_1)} + \frac{1}{R_2}\frac{H_n^{(2)}(\chi R_2)}{H_n^{(2)}(\chi R_1)}\right]\cdot e^{jn\phi}\cdot e^{-jhz}\,d\phi dz +$$

$$+\int\limits_{-\pi}^{+\pi}\int\limits_{-\infty}^{+\infty}\left\{\frac{1}{4\pi^2}\int\limits_{-\pi}^{+\pi}\int\limits_{-\infty}^{+\infty}E_\phi(R_1,\phi,z)\cdot e^{-jn\phi}\cdot e^{jhz}\,d\phi dz\right\}\times\frac{H_n^{(2)}(\chi R_2)}{H_n^{(2)}(\chi R_1)}\cdot e^{jn\phi}\cdot e^{-jhz}\,d\phi dz$$

(4.16)

So for the transformation from the first scanning cylinder to the second one the Hankel function of second kind are used. Note that the above expressions (4.15) and (4.16) can be implemented with high numerical efficiency by using the FFT algorithm. To simplify the relations (4.15) and (4.16) they are transcribed into the following forms

$$E_z(R_2,\phi,z) = 2\text{DFFT}^{-1}\left\{2\text{DFFT}[E_z(R_1,\phi,z)]\cdot\frac{H_n^{(2)}(\chi R_2)}{H_n^{(2)}(\chi R_1)}\right\}$$

(4.17)

$$E_\phi(R_2,\phi,z) = 2\text{DFFT}^{-1}\left\{\begin{array}{l}2\text{DFFT}[E_z(R_1,\phi,z)]\cdot\dfrac{nh}{\chi^2}\cdot\\[2mm]\cdot\left[-\dfrac{1}{R_1}\dfrac{H_n'^{(2)}(\chi R_2)}{H_n'^{(2)}(\chi R_1)} + \dfrac{1}{R_2}\dfrac{H_n^{(2)}(\chi R_2)}{H_n^{(2)}(\chi R_1)}\right]+\\[3mm]+2\text{DFFT}[E_\phi(R_1,\phi,z)]\cdot\dfrac{H_n'^{(2)}(\chi R_2)}{H_n'^{(2)}(\chi R_1)}\end{array}\right\}.$$

(4.18)

Formulas for transformation inside, from cylinder of radius R_2 to the cylinder radius R_1, have the same form just instead of Hankel functions of the second kind the first kind Hankel functions are applied. Moreover, derived electric filed distribution on the first scanning cylinder is multiplied by the ratio of the scanning cylinders radii (R_1/R_2).

The above expressions can be implemented in a simple way. Transformations involve matrix multiplications and Fourier transforms, which can be performed via the FFT. The computation of the matrix (4.15) involves essentially only Hankel functions;

therefore they can be evaluated at once and stored for subsequent use in the course of the iterative procedure.

### 4.1.1 Limitation of the near-field near-field transformations

The near-field transformations between two separate cylinders are related by the formulas which are based on Hankel functions. The Hankel functions of the first and second kind are used to express forward and backward-propagating cylindrical wave solutions of the cylindrical wave equation.

The limitations of the forward and backward transformations were investigated in [52], [60], [61]. For this purpose the linear array was modeled consisting of eight z directed electric dipoles placed along the z axis and $\lambda/2$ equispaced. Each dipole was fed by a unit electric current. The near field component along z of the electric field was synthesized from R_{min} to the end of NF region (30λ). Maximum dimension of the AUT was $R_{min} = 4\lambda$ (in z direction).

First, the limitation of the forward transformation was investigated. The theoretical values of the electric field component E_z in main cuts ($z = 0$ m, $\phi = 0^o$) were confronted with electric field distribution obtained by forward transformation of the computed electric distribution in distance 4λ. The comparison of electric field distribution from 4λ to 30λ is shown in Fig. 4.3. It can be observed from the achieved distributions that computed results are slightly different from the theoretical ones. Finally, it was found out that theoretical values and the calculated ones agree well in case when radius R_{min} was at least 5λ , see Fig. 4.4. It follows that the minimum radius value, where we are looking for the electric field distribution on antenna aperture, is chosen $R_{min} = 1.25D$, where D is the largest transverse dimension of the AUT.
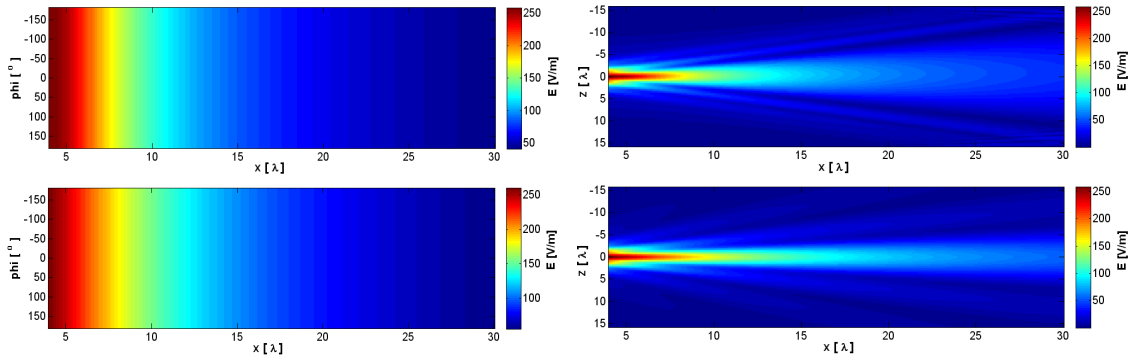
Fig. 4.3 Comparison of simulated amplitude distribution of electric field intensity E_z and calculated one obtained by forward transformation from electric distribution in distance 4λ in main cuts; top: calculated; bottom: theoretical
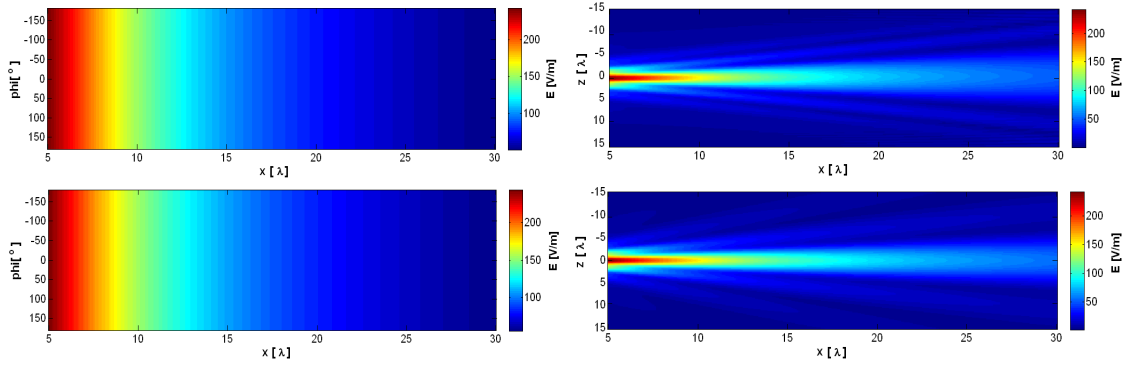
Fig. 4.4 Comparison of simulated amplitude distribution of electric field intensity E_z and calculated one obtained by forward transformation from electric distribution in distance 5λ in main cuts; top: calculated; bottom: theoretical

Now let us pay attention to backward transformation. Transformations were made from 30λ, 20λ and 10λ to distance of R_{min} (5λ). Comparisons of the computed and theoretical electric field distribution in vertical cut ($\phi = 0^o$) and horizontal cut ($z = 0$ m) are depicted in Fig. 4.5 – Fig. 4.7.

It can be observed from backward transformations that the transformations retain the character of the electric field distribution but compared to the theoretical distributions these vary in levels of the electric field. The difference is more obvious when the transformation is carried out to greater distances. Therefore, for the backward transformation it is preferable that the distance between cylinders for which the transformation is carried out is minimal.

Methods based on local minimization of functional require a relatively large separation of the scanning surfaces (usually a few wavelengths [19]), to provide as different amplitude distribution as possible. This can be avoided by using an algorithm based on GO. It was proved that the radiation patterns can be reconstructed even when the distance between scanning surfaces is less than half of the wavelengths [7], [50]. So the condition of the minimum distance between cylinders can be satisfied.
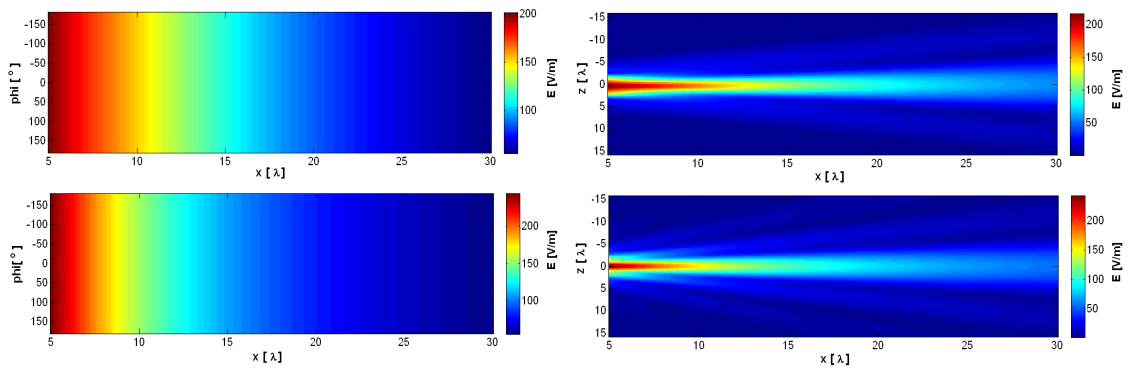

Fig. 4.5 Comparison of simulated amplitude distribution of electric field intensity E_z and calculated one obtained by backward transformation from electric distribution in distance 30λ in main cuts; top: calculated; bottom: theoretical

Fig. 4.6 Comparison of simulated amplitude distribution of electric field intensity E_z and calculated one obtained by backward transformation from electric distribution in distance 20λ in main cuts; top: calculated; bottom: theoretical
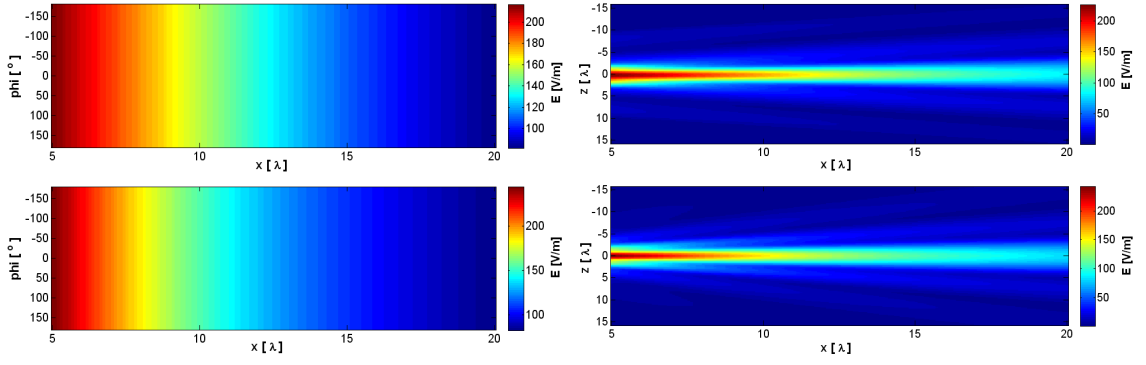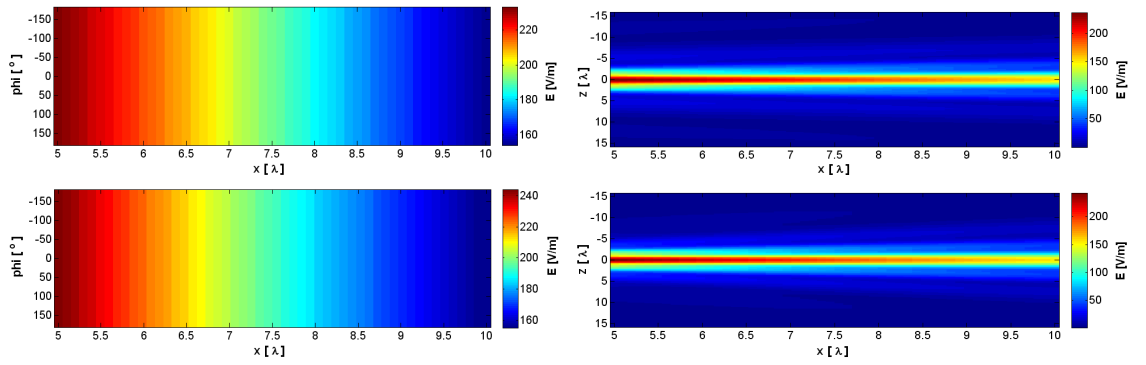

**Fig. 4.7** Comparison of simulated amplitude distribution of electric field intensity E_z and calculated one obtained by backward transformation from electric distribution in distance 10λ in main cuts; top: calculated; bottom: theoretical

4.2 Phase retrieval cylindrical algorithm

The designed functional based method was made-over for cylindrical scanning geometry. Unlike in the planar field the goal of the algorithm is to find the minimal value of functional representing the electric field distribution on the cylinder with minimum radius R_{min}. The radius R_{min} corresponds to the largest transverse dimension of the AUT [58], [59], [62], [66]. Also in this case of the cylindrical scanning, the amplitudes on a single and two cylinder surfaces will be assumed and comparison of the methods will be done.

Since it was found out that the backward transformation is less accurate than the forward transformation the classic minimization approach instead of the new one (chapter 3.1.2) is used. The classic minimization approach does not employ backward transformation. Otherwise the cylindrical minimization algorithm was designed according to the planar algorithm. The fitness function to be minimized has also the same form (3.7).
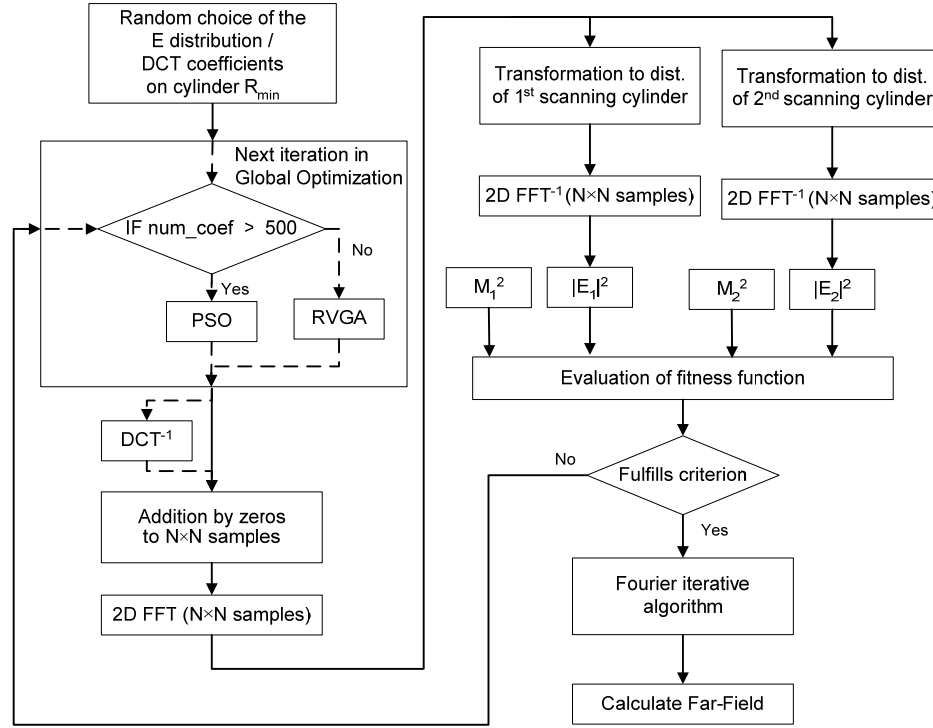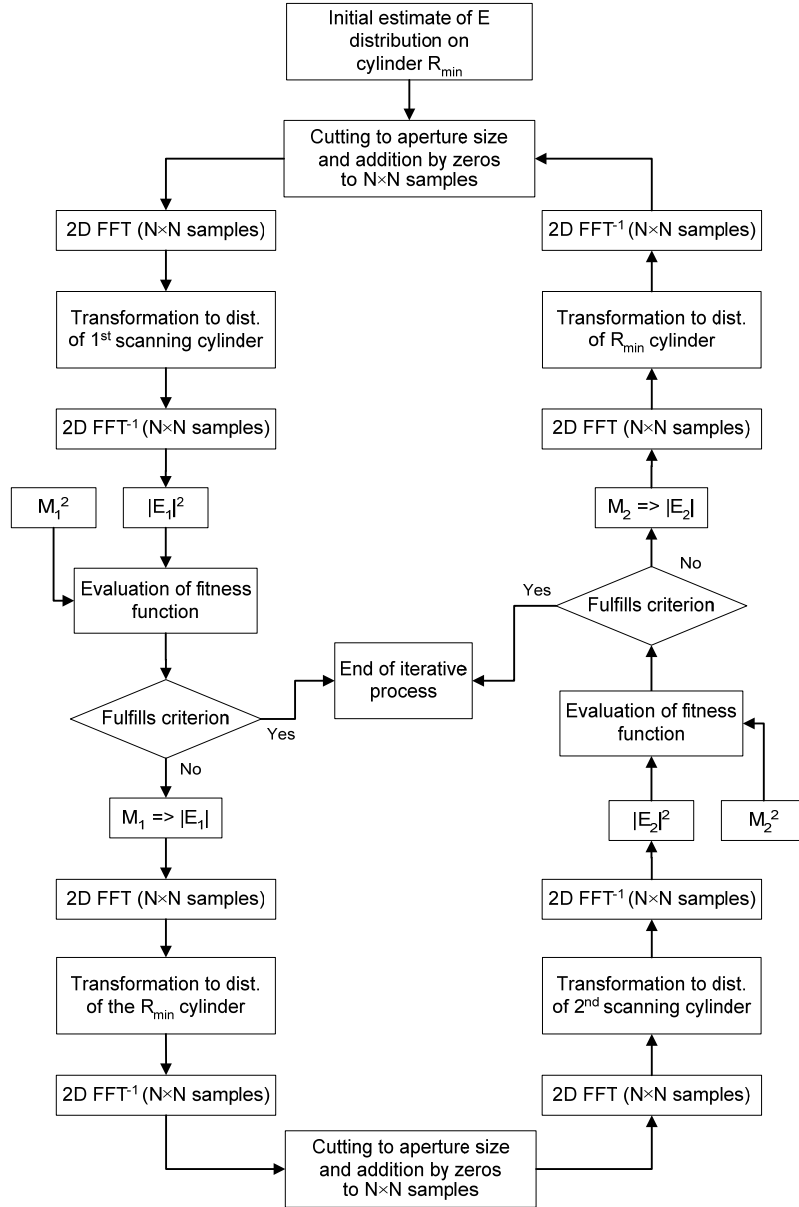
Fig. 4.8 Flow chart of the cylindrical minimizing algorithm

The classic approach used in the designed minimization method is shown in Fig. 4.8. First, random initial estimate of the electric field distribution on the cylinder R_{min} is performed. Zero padding is applied to the distribution to get the same extension as the scanning surfaces have. After this operation, the initial electric field is propagated using Hankel functions to the distance of the first and the second scanning surfaces. In the next step, the computed and the measured amplitudes are compared. For electrically large antennas the minimization algorithm is complemented by the image compression method (the DCT). The procedure is repeated until the maximum number of iterations is reached. In the next part the FIA is used for improving of the initial estimate obtained by minimization algorithm. The made-over algorithm for cylindrical case is depicted in Fig. 4.9. In the FIA backward transformations are used so we have to keep in mind that we introduce error into the algorithm by using backward transformations. Finally, the calculated electric field distribution on cylinder R_{min} is used to calculate the far-field pattern of the antenna.

In case of the single-plane algorithms the schemes have only one difference. Since the amplitudes on a single surface only are assumed, the transformations to the second cylinder are eliminated.

Fig. 4.9 Flow chart of the Fourier iterative method for cylindrical case

4.3 Application of the designed minimization method for reconstruction of radiation patterns

The application of the described method was carried out on the radiation pattern reconstruction of the horn antenna and the dish antenna. The same antennas were used for comparison of the novel algorithm with the hybrid method (chapter 3.5.2). The experimental measurements were carried out in collaboration with the Microwave Laboratory of the University of Calabria, Italy [35].

The horn antenna

The rectangular horn antenna had the aperture of the size 70×50 mm. The antenna was analyzed at the frequency 10 GHz. A rectangular waveguide R100 was used as the

scanning probe. The values of the electric field intensity were scanned with the sampling steps $\Delta z = 15$ mm ($\lambda/2$) and $\Delta\phi = 4^o$ at two scanning cylinders placed in the distance of 200 mm and 400 mm from the AUT aperture. 4 230 (47×90) values on each cylinder were obtained. The height of the cylinders was 690 mm, therefore the valid angle in vertical cut was $\theta_v = \pm 58^o$. Since the aperture field of the antenna is desired, the solution space contains only 40 real parameters. The measurement site arrangement is shown in Fig. 4.10.

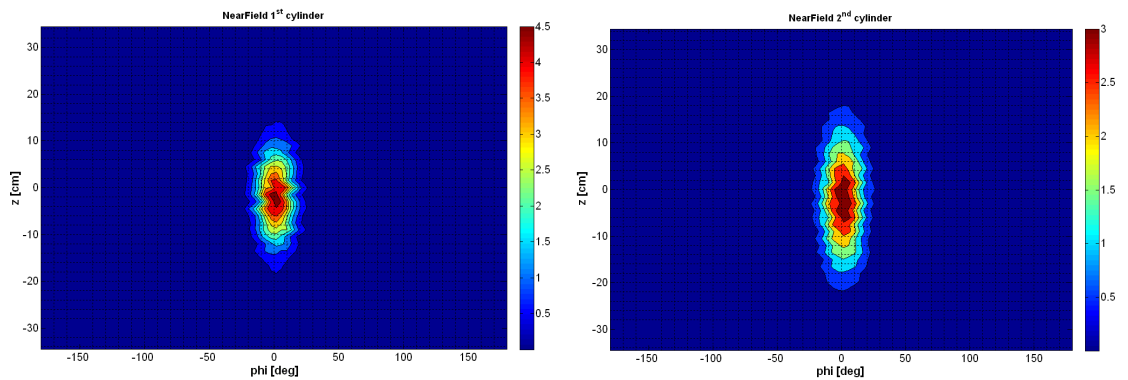The contour plots of the near-field amplitudes measured by the probe are depicted in Fig. 4.11. We can observe amplitude shifts in some rows of the contour plot. It was due to the scanning facility which shifts the measurement point for one step in some rows.
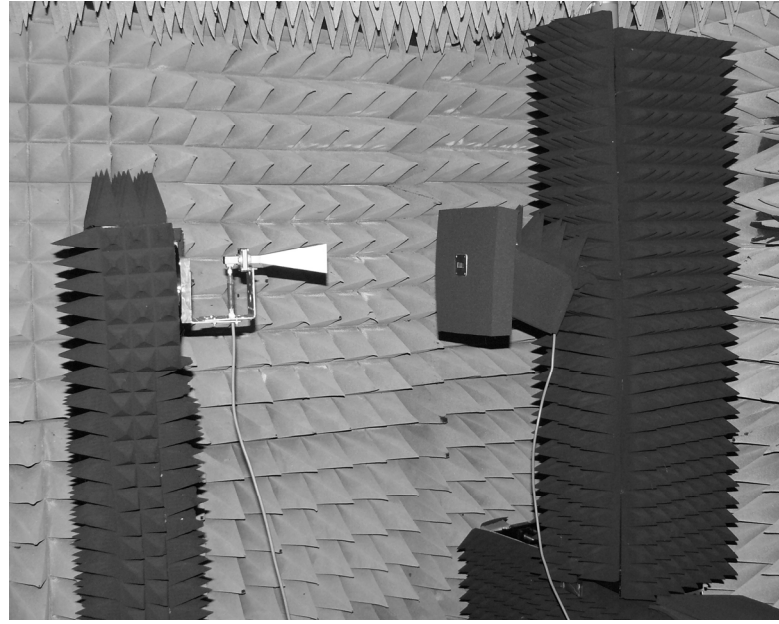
Fig. 4.10 Measurement site arrangement of the horn antenna

**Fig. 4.11** Contour plot of the near-field amplitudes for both scanning cylinder; horn antenna

The minimization algorithm using RVGA without the DCT was used for the initial reconstruction of the phases and amplitudes on the cylinder of radius $R_{min} = 190$ mm (the distance between AUT aperture and rotation axis). The reconstruction was carried out for electric field component E_z only in domain $\pm 90^o$. The single amplitude

algorithm and the two amplitude algorithm were assumed for the reconstruction of the radiation patterns.

The results obtained after 50 iterations are shown in Fig. 4.12 and Fig. 4.13. The radiation patterns obtained by the single surface algorithm are depicted by dashed line and the two surface algorithm are depicted by dotted line. The reconstructed far-field radiation patterns show that the accuracy of the obtained results is not sufficient yet and the improvement of accuracy is necessary. For this purpose the local method was applied to ensure the required precision of the radiation patterns. The far-field results obtained after using the FIA are shown in Fig. 4.14 and Fig. 4.15. The reconstructed radiation patterns are in good agreement with the pattern gained by the direct transformation in domain of the main lobe i.e. in E plane it is $\pm60^{\circ}$ and in H plane it is $\pm40^{\circ}$. If we compare the results obtained by the single-surface and the two-surface functional based method, we can observe that the accuracy of the retrieved phase is comparable.
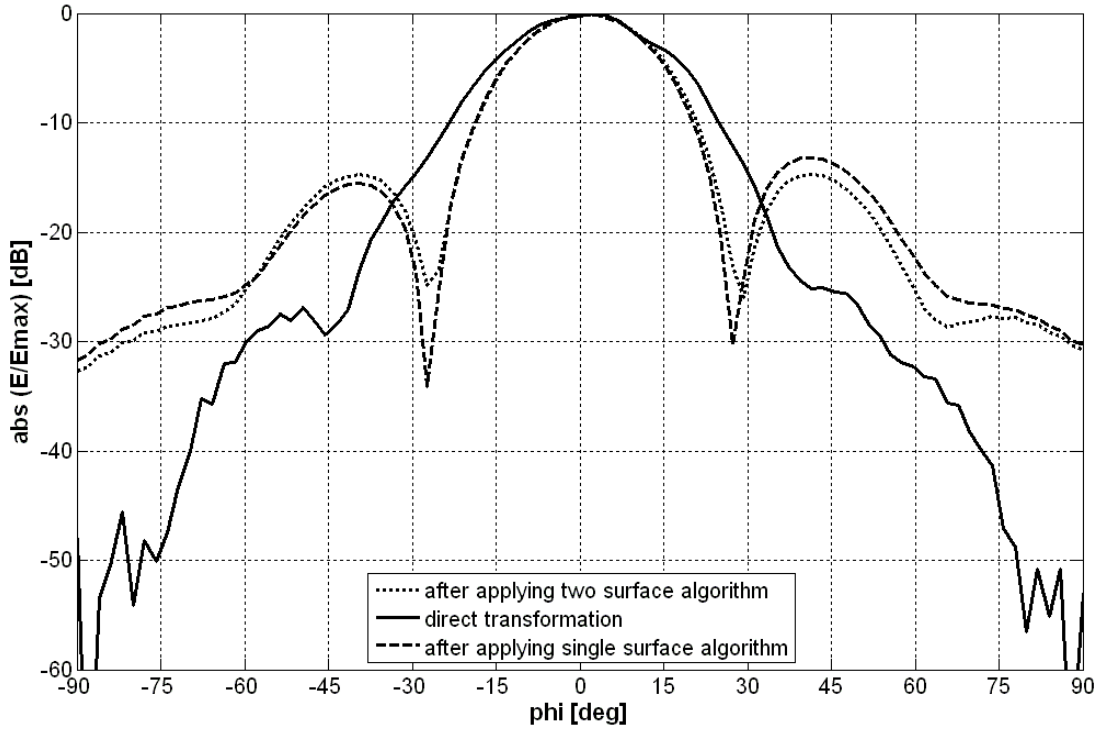
Fig. 4.12 Reconstructed H plane radiation patterns of the horn antenna after applying single the surface algorithm and the two surface algorithm
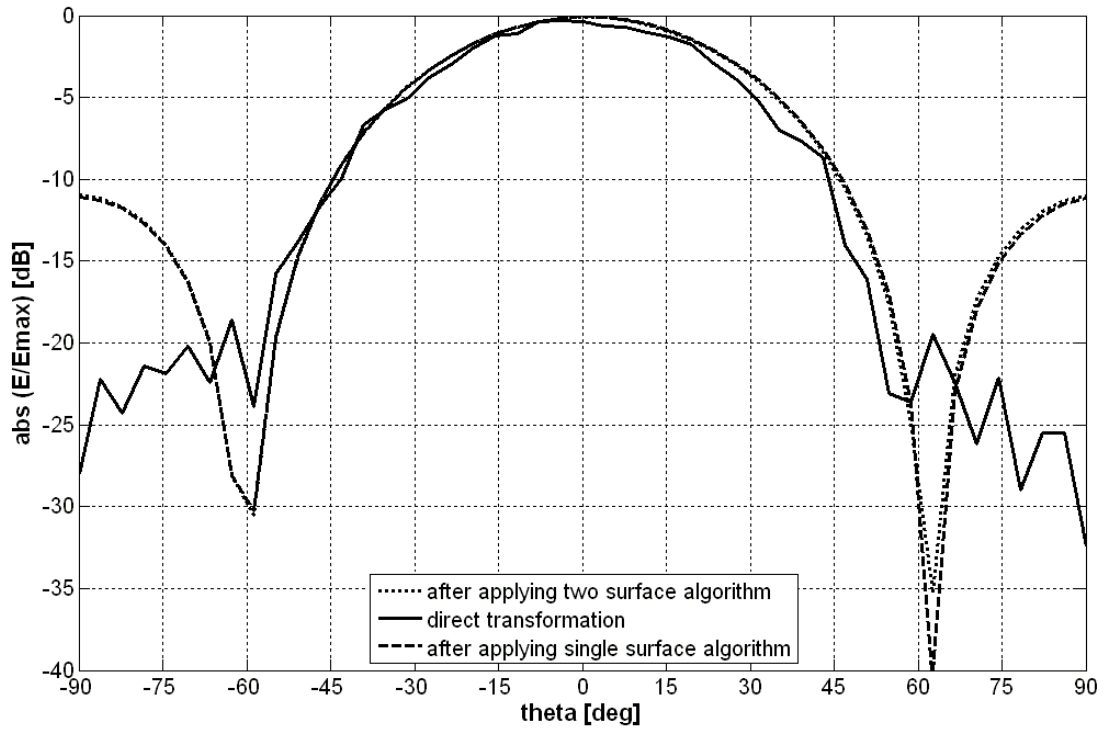
Fig. 4.13 Reconstructed E plane radiation patterns of the horn antenna after applying the single surface algorithm and the two surface algorithm
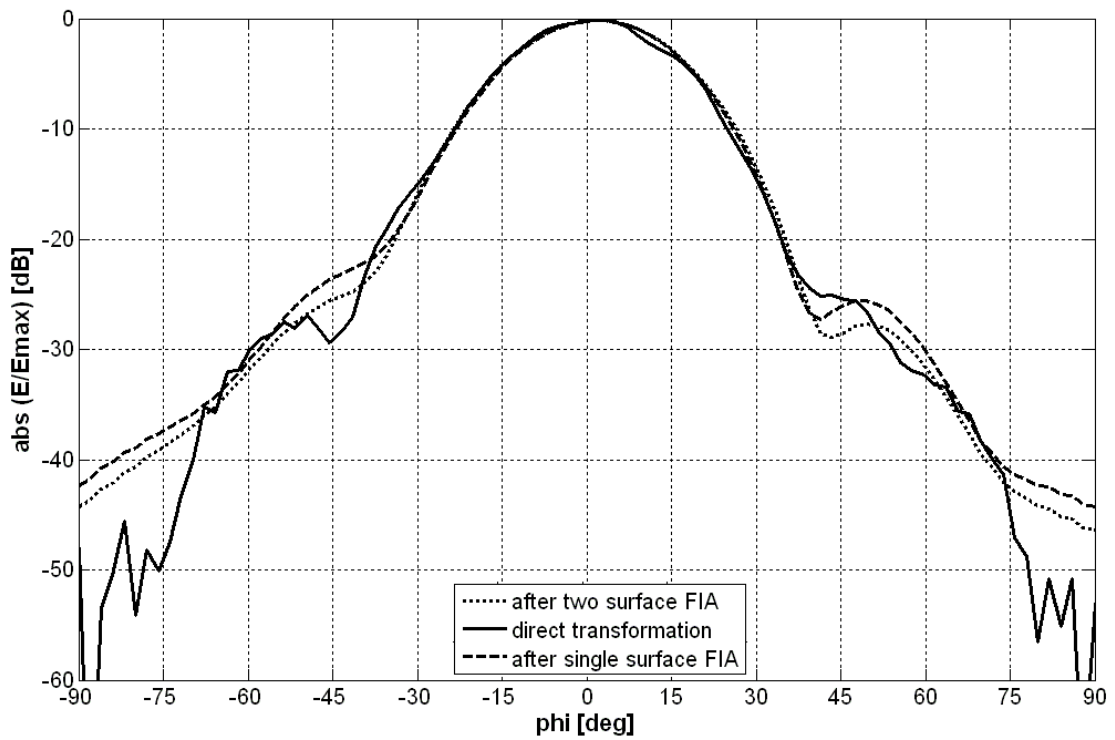
Fig. 4.14 Reconstructed H plane radiation patterns of the horn antenna after applying the single surface FIA and the two surface FIA

Fig. 4.15 Reconstructed E plane radiation patterns of the horn antenna after applying the single surface FIA and the two surface FIA

The dish antenna

The algorithm was also experimentally tested on a standard X-band dish antenna having a reflector diameter of 0.34 m, see Fig.4.16. A rectangular waveguide of aperture dimensions 22.86 mm × 10.16 mm was used as the scanning probe. Near-field amplitude measurements were performed on two cylindrical surfaces of radius R_1 = 600 mm and R_2 = 800 mm, respectively. The antenna was analyzed at a frequency 10 GHz within a cylindrical grid of 67×145 points along z and ϕ, respectively. Sampling steps Δz = 15 mm ($\lambda/2$) and $\Delta \phi$ = 2.5° were used. Since the aperture of the antenna is 340 mm × 340 mm (23 times 23 sampling points), the solution space contains 1 058 complex parameters the optimal values of which are to be found out.
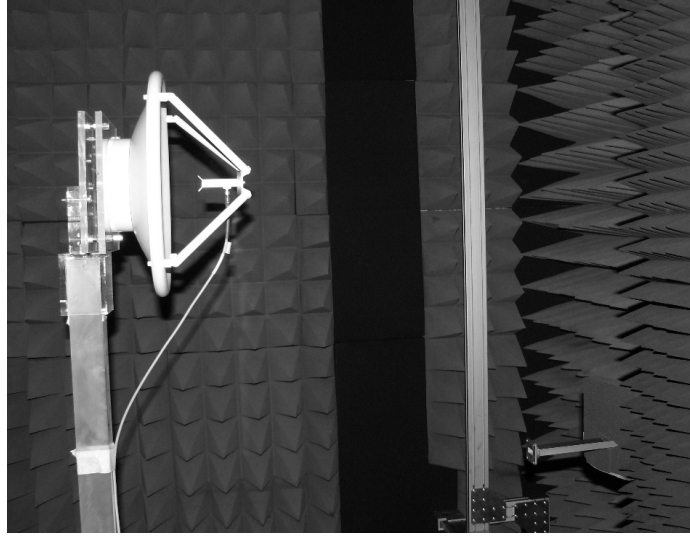
Fig. 4.16 Measurement site arrangement of the dish antenna
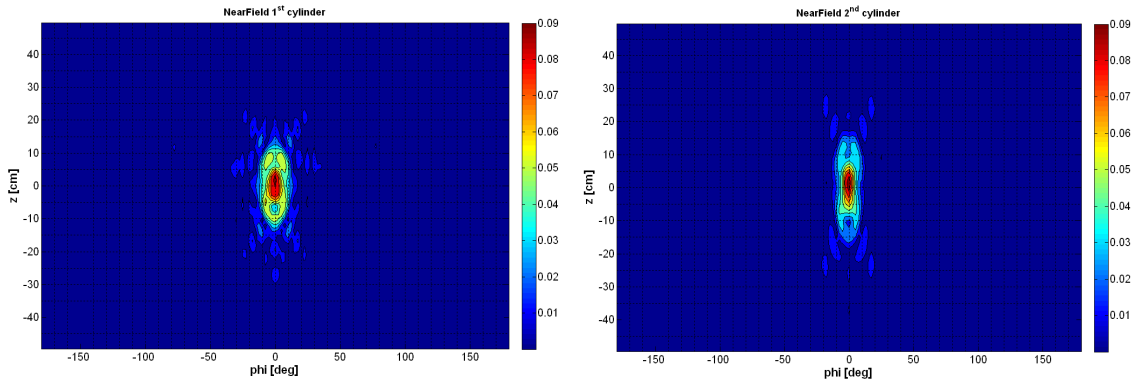
Fig. 4.17 Contour plot of the near-field amplitudes for both scanning cylinders; dish antenna

The reconstruction was carried out for electric field component E_z only. The minimization approach with the DCT was used for the initial reconstruction of the phases and amplitudes on the cylinder of radius 350 mm (R_{min}). For the reconstruction, the RVGA/DCT method exploits 20 coefficients instead of 529 complex parameters representing electric field distribution on cylinder R_{min}. Radiation patterns obtained after one hundred iterations are shown in Fig. 4.18 and Fig. 4.19. We can see that the accuracy of retrieved far-field is not sufficient, especially in H plane. It is due to the lossy compression method used.

Subsequently, the Fourier iterative method was used to improve the initial estimate obtained by RVGA/DCT, see Fig. 4.20 and Fig. 4.21. For the two-surface FIA, the agreement between the retrieved far-field and far-field obtained by transformation of the complex near-field data is excellent in the domain of the main lobe. We can observe that the retrieved far-field becomes less accurate approximately below -30 dB.

The use of single cylinder FIA showed the problem with reconstruction of radiation pattern, especially in H plane where it was not even able to reconstruct the main lobe. So, knowledge of the amplitudes on one cylinder is sufficient for getting the initial estimate lying in the global minimum. Thus, the process of obtaining the initial estimate can be simplified and speeds up compared with the two-cylinder algorithm. But to refine the results, the two-cylinder FIA is necessary.
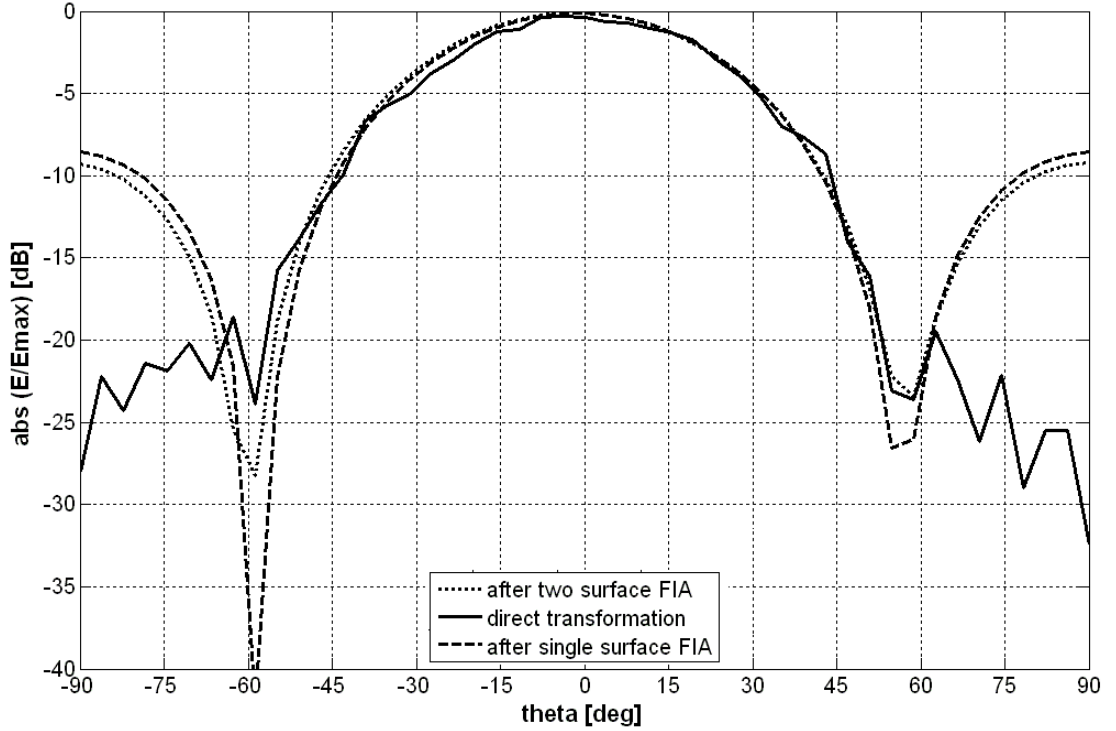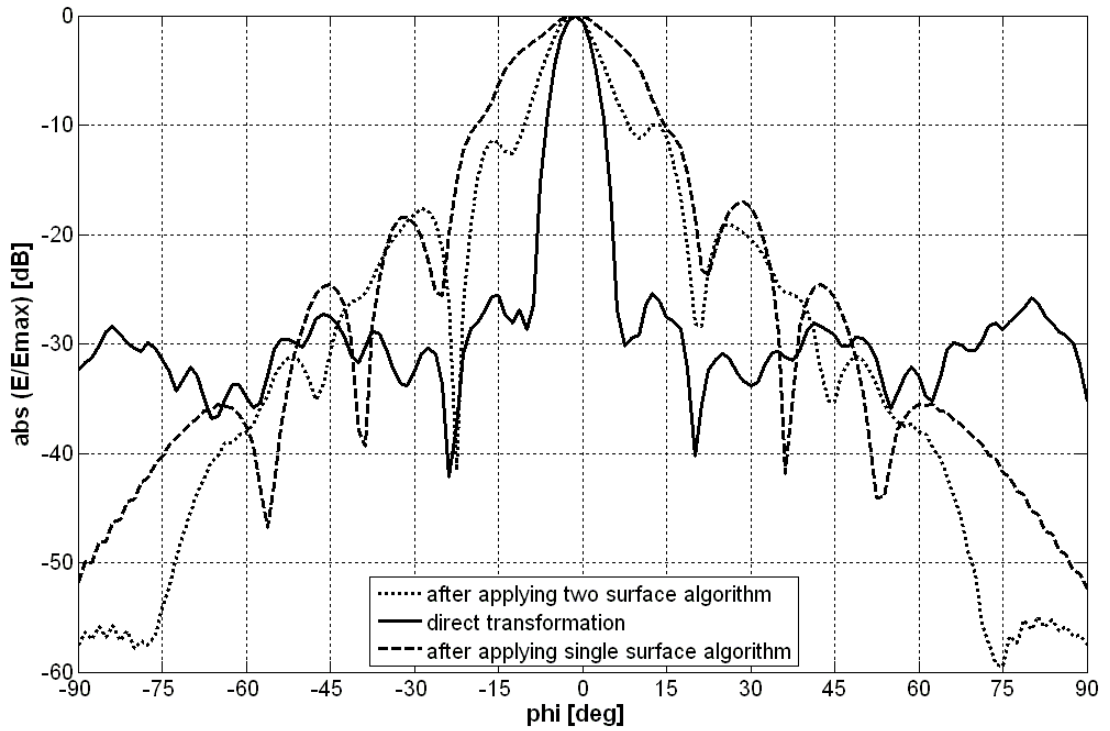
Fig. 4.18 Reconstructed H plane radiation patterns of the dish antenna after applying the single surface algorithm and the two surface algorithm
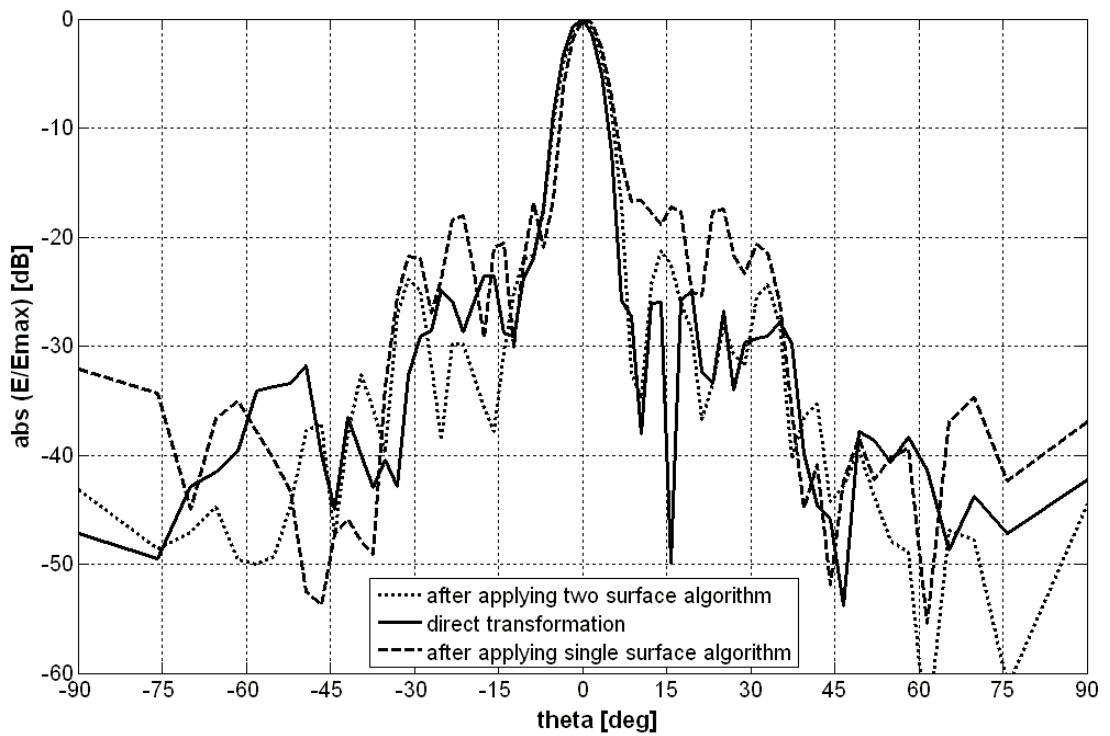
Fig. 4.19 Reconstructed E plane radiation patterns of the dish antenna after applying the single surface algorithm and the two surface algorithm
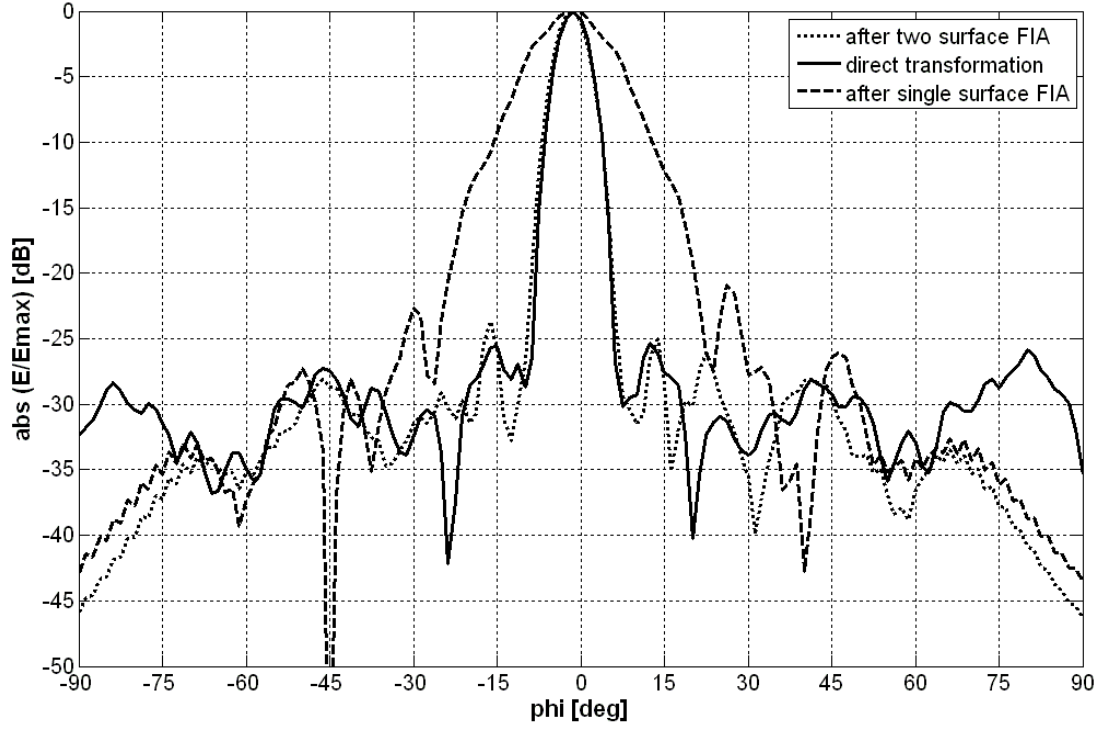
Fig. 4.20 Reconstructed H plane radiation patterns of the dish antenna after applying the single surface FIA and the two surface FIA
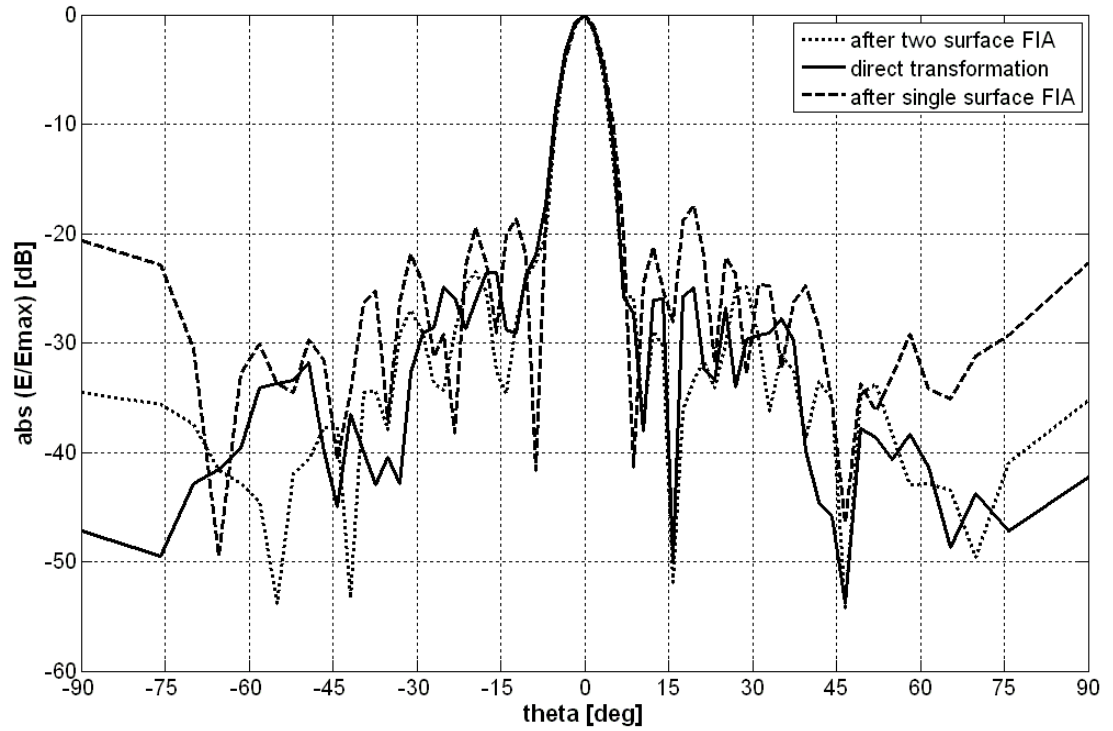

Fig. 4.21 Reconstructed E plane radiation patterns of the dish antenna after applying the single surface FIA and the two surface FIA

A novel phase retrieval method combining a global optimization with image compression method and simple iterative method was described in this chapter. The method was applied for the cylindrical near-field phaseless measurements. The

designed method eliminates the disadvantages of the previous cylindrical methods [19], [23]. The algorithm does not require an initial estimate in the area of the global minima obtained by a rough phase measurement, and does not need additional information about the measured antenna.

The two-cylinder functional based algorithm is very robust and faster than minimization algorithms published so far. The described algorithm was applied for the phase reconstruction of two different antennas (dish antenna and horn antenna). The accuracy of the far-field patterns obtained by the phase retrieval algorithm is comparable with other minimization methods. In case of the single cylinder phase retrieval algorithm it was found out that if we reconstruct the radiation patterns of an antenna having relatively simple electric field distribution on antenna aperture, accuracy of the obtained results is sufficient. Otherwise, the accuracy can strongly depend on the type of the analyzed antenna.

5 Conclusions

This thesis deals with the reconstruction of the radiation patterns from phaseless measurements in the near field. This theme is still current and a complete solution has not been found for many problems yet. Particularly, the effective minimization of the functional and the effective reconstruction of the phase distribution are the biggest problems of all the current methods.

The introduction briefly describes the main phase retrieval methods used for obtaining radiation patterns from the amplitude measurements in the near field. Their advantages and disadvantages were described. In most cases, these functional based methods suffer from a large numerical complexity or large computational efforts. Therefore, effective minimization of the functional and the effective reconstruction of the phase distribution, respectively, are required.

The above mentioned facts imply the aim of my dissertation which is to find a minimization algorithm that works very effectively even in cases when the radiation properties of electrically large antennas are analyzed. The application of the novel minimization algorithm for cylindrical scanning geometry is also the aim of the dissertation.

Under these circumstances, the properties of minimization algorithm were researched. The selection of the minimization approach, optimization technique and the appropriate functional influences mainly convergence properties of the algorithm. That is why they were investigated and appropriately chosen. To reveal the global minimum area faster, the possibilities in the form of initial estimates for accelerating minimization algorithm were also considered. And finally, the idea of representation of the unknown electric field distribution by a few coefficients was implemented into the minimization algorithm.

The aim has been realized and the novel original method for reconstructing an unknown phase distribution from two amplitude measurements was presented. The proposed algorithm is very robust and faster than comparable algorithms available. The algorithm does not require any initial guess in the region of the global minima and any additional information about the AUT. The application of the described algorithm for the phase reconstruction was verified for four kinds of antennas.

Designed near-field phaseless approach for the antenna far-field characterization combines a global optimization, an image compression method and a local optimization in conjunction with conventional two-surface amplitude measurements. The global optimization method is used to minimize the functional, the image compression method is used to reduce the number of unknown variables, and the local optimization method is used to improve the estimate achieved by the previous method. As the minimization tool, two optimization techniques were chosen, Real-Coded Genetic Algorithm and Particle Swarm Optimization. The decision on which method will be used is based on the number of optimized variables. Due to its best compression properties, the Discrete Cosine Transform is considered to reduce the number of unknown variables. The usage

of a compression method for reconstruction of phase is completely original and had never been published before this thesis. The Fourier iterative algorithm which is commonly used in the reconstruction of radiation patterns is exploited as a local method.

The previous minimization method is based on the minimization of the difference between the calculated and measured amplitudes on two surfaces (on single surface with two different probes) in the near-field region. Other investigations presented in this thesis were focused on the possibilities of using amplitude from only a single scanning surface for reconstruction of the radiation pattern.

It was found out that knowledge of the amplitudes on a single surface in the minimization algorithm is sufficient for obtaining initial estimate lying in the global minimum. Thus, the process of obtaining the estimate can be simplified and speeds up compared with the two-surface algorithm. In the second part of the algorithm, in Fourier iterative algorithm, amplitudes from a single surface can be used only if the reconstruction is performed for antennas having relatively simple electric field distribution on antenna aperture and the main lobe perpendicular to the scanning surface. In these cases, the accuracy of the obtained results is comparable with algorithm using amplitude measurements over two surfaces. Otherwise, the accuracy of the results may depend strongly on the investigated antenna.

The novel phase retrieval algorithm was applied also for cylindrical geometry which is suitable mainly for antennas having a narrow pattern on one axis and a broad pattern on a second axis. The reconstructions carried out on a cylindrical surface confirmed the findings established during the reconstruction on a plane surface.

Bibliography

[1] FORDHAM, A. J. An Introduction to Antenna Test Ranges, Measurements and Instrumentation. Microwave Instrumentation Technologies, LLC. available on http://www.lehman-inc.com/pdf/mag.pdf

[2] YAGHJIAN, A. Z. An Overview of Near-Field Antenna Measurements. *IEEE Transaction on Antennas and Propagation*. 1986, vol. 34, no. 1, p. 30 – 45.

[3] WACKER, P. F. Unified Theory of Near-Field Analysis and Measurement: Nonmathematical Discussion. *IEEE Transactions on Antennas and Propagation*, vol. Ap-30, no. 1, 1982

[4] SLATER, D. *Near-Field Antenna Measurements*. Boston: Artech House, 1991, ISBN 0-89006-361-3.

[5] APPEL-HANSEN, J. *"Antenna measurements" in The Handbook of Antenna Design*, vol. 1, London: Peregrinus, ch. 8. 1982. ISBN 0906048826

[6] JOHNSON, R. C. ECKER, H. A. AND HOLLIS, J. S. Determination of far-field antenna patterns from near-field measurements, Proc. *IEEE*, vol. 61, pp. 1668–1694, Dec. 1973.

[7] TKADLEC, R. *Near-Field Antenna Measurements*. Dissertation Thesis. Brno: Brno University of Technology, 2005.

[8] KERNS, D. M. Analytical Techniques for the Correction of Near-field Antenna Measurements Made With an Arbitrary but Known Measuring Antenna. In *Abstract of URSI-IRE Meeting*. Washington DC 1963, p. 6–7.

[9] RAHMAT-SAMII, Y. GALINDO-ISRAEL, V. AND MITTRA, R. A plane-polar approach for far-field construction from near-field measurements, *IEEE Trans. Antennas Propagat.*, vol. AP-28, pp. 216–230, Mar. 1980.

[10] WILLIAMS, L. I. RAHMAT-SAMII, Y. Novel bi-polar planar near-field measurement scanner at UCLA, In *IEEE Antennas Propagat. Soc. Int. Symp. Dig.*, Ontario, Canada, June 1991, pp. 1446–1449.

[11] LEACH, Jr., W. M., PARIS, D. T. Probe-Compensated Near-field Measurements on Cylinder. *IEEE Transaction on Antennas and Propagation*. 1973, vol. 21, no. 7, p. 435 – 445.

[12] WACKER, P. F. Near-field Antenna Measurements Using a Spherical Scan: Efficient Data Reduction With Probe Correction. In *IEE conference publication*. London 1974, p. 286 – 288.

[13] RICARDI, L. J., BARROWS, M. L. A Recurrence Technique for Expanding a Function in Spherical Harmonics. *IEEE Transaction on Computation*. 1972, vol. 21, no. 6, p. 583 – 586.

[14] YAGHJIAN, A. D. *Near-Field Antenna Measurements on a Cylindrical Surface: a Source Scattering-Matrix Formulation*. Boulder, CO: National Bureau of Standards, 1977, NBS Technical Note 696 (revised).

[15] HANSEN, J. E. HALD, E. J. JENSEN, F. AND LARSEN, F. H. *Spherical Near-Field Antenna Measurements*. London, U.K.: Peter Peregrinus, 1988.

[16] YAGHJIAN, A. D. Sampling criteria for resonant antennas and scatterers, *J. Appl. Phys.*, vol. 79, pp. 7474–7482, May 1996, (correction, vol. 79, p. 2547, Aug. 1996).

[17] BUCCI, O.M. GENNARELLI, C. RICCIO, G. Efficient near-field-far-field transformation with cylindrical scanning by a finite and non redundant number of data. *Antennas and Propagation Society International Symposium*, 1995. AP-S. Digest Vol. 1, June 1995, pp. 256 - 259

[18] HANSEN, T.B. MARR, R.A. LAMMERS, U.H.W. Bistatic RCS Calculations From Cylindrical Near-Field Measurements. Antennas and Propagation, *IEEE Transactions*. Volume 54, Issue 12, Dec. 2006 pp. 3846 - 3856

[19] ISERNIA, T. LEONE, and G. PIERRI, R. A new approach to antenna testing from near field phaseless data: the cylindrical scanning. *IEEE Proc. H*, 1992, 139, pp. 363-368

[20] GABOR, D. Microscopy by reconstructed wavefronts, In *Proc. Royal Soc.*, London, U.K., vol. A, no. 197, pp. 454–487, 1949.

[21] JUNKIN, G. BENNET, J. C. HUANG, T. Holographic near-field/far-field for therahertz antenna testing, in *Proc. 19th Antenna Measurement Tech. Assoc. Meet. Symp.*, Boston, MA, Nov. 1997, pp. 419–423.

[22] ERICKSON, N., TOLLS, V. Near-field Measurements of the Submillimeter Wave Astronomy Satellite Antenna. In *Proceedings of the 20th ESTEC Antenna Workshop on Millimeter Wave Antenna Technology and Antenna Measurements*. Noordwijk 1997, p. 313 – 319.

[23] BUCCI, O. M., D'ELIA, G., LEONE, G., PIERRI, R. Far-field Pattern Determination from the Near-field Amplitude on Two Surfaces. *IEEE Transaction on Antennas and Propagation*. 1990, vol. 38, no. 11, p. 1772 – 1779.

[24] LEONE, G., PIERRI, R., SOLDOVIERI, F. On the Performances of Two Algorithms in Phaseless Antenna Measurements. In *Proceedings of the 10th ICAP*. Edinburgh 1997, p. 1/136 – 1/141.

[25] ISERNIA, T., LEONE, G., PIERRI, R. Radiation Pattern Evaluation from Near-Field Intensities on Planes. *IEEE Transactions on Antennas and Propagation*. 1996, vol. 44, no. 5, p. 701 – 710.

[26] PIERRI, R., D'ELIA, G., SOLDOVIERI, F. A two Probes Scanning Phaseless Near-field Far-field Transformation Technique. *IEEE Transaction on Antennas and Propagation*. 1999, vol. 47, no. 5, p. 792 – 802.

[27] NEWELL, A. C. Error analysis techniques for planar near-field measurements. *IEEE Transactions on Antennas and Propagation*. 1988, vol. 36, no. 6, p. 754 – 768.

[28] YACCARINO, R. G., RAHMAT-SAMII, Y. Phaseless Bi-Polar Planar Near-Field Measurements and Diagnostics of Array Antennas. *IEEE Transactions on Antennas and Propagation*. 1999, vol. 47, no. 3, p. 574 – 583.

[29] RAHMAT-SAMII, Y. YACCARINO, R. G. Microwave antenna imaging, diagnostics, and phaseless reconstruction. *Int. J. Imaging Syst. Technol.*, vol. 8, no. 4, pp. 396–406, 1997.

[30] RAZAVI, S. F., RAHMAT-SAMII, Y. A new look at phaseless planar near-field measurements: limitations, simulations, measurements, and a hybrid solution. *IEEE Antennas and Propagation Magazine*, vol. 49, no. 2, 2007, pp. 170-178

[31] PETRE, P. SARKAR, T. K. Planar near-field to far field transformation using an equivalent magnetic current approach. *IEEE Trans. Antennas Propagat.*, vol. 40, pp. 1348–1356, Nov. 1992.

[32] TAAGHOL, A. SARKAR, T. K. Near-field to near/far-field transformation for arbitrary near-field geometry, utilizing an equivalent magnetic current. *IEEE Trans. Electromagn. Compat.*, vol. 38, pp. 536–541, Mar. 1996.

[33] LAS-HERAS, F. SARKAR, T. K. A direct optimization approach for source reconstruction and NF-FF transformation using amplitude-only data. *IEEE Trans. Antennas Propag.*, vol. 50, no. 4, pp. 500–510, Apr. 2002.

[34] ALVAREZ, Y. LAS-HERAS, F. PINO, M. R. Reconstruction of Equivalent Currents Distribution Over Arbitrary Three-Dimensional Surfaces Based on Integral Equation Algorithms. *IEEE transactions on antennas and propagation*, vol. 55, no. 12, pp. 3460-3468, December 2007

[35] COSTANZO, S. DI MASSA, G. and MIGLIORE, M. D. A novel hybrid approach for far-field characterization from near-field amplitude-only measurements on arbitrary scanning surfaces. *IEEE transactions on antennas and propagation*, vol. 53, no. 6, pp. 1866-1874, June 2005

[36] COSTANZO, S. DI MASSA, G. An integrated probe for phaseless near-field measurements. *Measurement*, vol. 31, pp. 123–129, 2002.

[37] COSTANZO, S. DI MASSA, G. and MIGLIORE, M. D. Integrated microstrip probe for phaseless near-field measurements on plane-polar geometry. *Electron. Lett.*, vol. 37, no. 16, 2001.

[38] ROBINSON, J., SINTON, S., RAHMAT-SAMII, Y. Particle swarm, genetic algorithm, and their hybrids: optimization of a profiled corrugated horn antenna. In *Proceedings of the IEEE International Symposium on Antennas and Propagation*. San Antonio: IEEE, 2002, vol. 1, p. 314–317.

[39] CARLISLE, A., DOIZIER, G. An off-the-shelf PSO. In *Proc. Workshop Particle Swarm Optimization*. Indianapolis, 2001.

[40] ZELINKA, I. *Artificial Intelligence in Problems of Global Optimization*, BEN, 2002, 190 p. ISBN 80-7300-069-5

[41] KURUP, D. G. HIMDI, M. RYDBERG, A. Synthesis of Uniform Amplitude Unequally Spaced Antenna Arrays Using the Differential Evolution Algorithm. *IEEE Transactions on Antennas and Propagation*, AP-51, 9, September 2003, pp. 2210-2217.

[42] JOHNSON, J. M., RAHMAT-SAMII, Y. Genetic algorithms in engineering electromagnetics. *IEEE Antennas and Propagation Magazine*. 1997, vol. 39, no. 4, p. 7–21.

[43] HAUPT, R. L., HAUPT, S. E. *Practical genetic algorithm*. A Wiley-Interscience Publication, 1998, ISBN 0-471-18873-5

[44] AHMED, N., NATARAJAN, T., RAO, K. R. Discrete cosine transform, *IEEE Trans. Computer*, vol. COM-23, no. 1, pp. 90-93, 1974.

[45] DAUBECHIES, L. The Wavelet Transforms, 'Time-Frequency Localization and Signal Analysis. *IEEE Trans. Inform. Theory*, 1990,36: 963-3005.

[46] BUCCI, O. M. GENNARELLI, C. AND SAVARESE, C. Representation of electromagnetic fields over arbitrary surfaces by a finite and nonredundant number of samples. *IEEE Trans. Antennas Propag.*, vol. 46, pp. 351–359, 1998.

[47] VON LERBER, A. VIIKARI, LISENO, V. ALA-LAURINAHO, J. AND RÄISÄNEN, A.V. A Feasibility study of phase retrieval algorithms at sub-millimeter wavelengths. In *Proceedigns of The 27th Annual Antenna Measurement Techniques Association (AMTA) Meeting & Symposium*, Newport, RI, USA, 2005, p. 79 - 84.

List of my references

[48] PUSKELY, J. NOVÁČEK, Z. POKORNÝ, M. Using global optimization approaches to reconstruct radiation patterns. In *Proceedings of the 14th Conference on Microwave Techniques COMITE 2008*. 2008. s. 347-350. ISBN: 978-1-4244-2137-4.

[49] PUSKELY, J. NOVÁČEK, Z. Application of the global optimization approaches to planar near-field antenna phaseless measurements. In *Proceedings MMS'2008 Mediterranean Microwave Symposium*. Damascus: 2008. s. 231-236. ISBN: 9954-8577-0-2.

[50] PUSKELY, J. NOVÁČEK, Z. Antenna far-fields determination from phaseless measurement using the real-valued GA. In *Proceedings of the Junior Scientist Conference 2008*. 2008. p. 271 - 272. ISBN 978-3-200-01612-5.

[51] PUSKELY, J. NOVÁČEK, Z. Evaluating power density in vicinity of commercial antennas . In *Proceedings of 17th International Conference on Microwaves, Radar and Wireless Communications MIKON 2008, vol. 1*. 2008. s. 205-208. ISBN: 83-906662-7-8.

[52] PUSKELY, J. Field Investigation in Vicinity of Dipole Arrays. In *12th International Student Conference on Electrical Engineering POSTER 2008*. 2008. s. 5-8.

[53] PUSKELY, J. NOVÁČEK, Z. Using global optimization to reconstruct phase distribution on antenna's aperture from only amplitude measurements. In *Proceedings of the 14th conference STUDENT EEICT 2008, 3.vol.* 2008. s. 52-56. ISBN: 978-80-214-3616-9.

[54] PUSKELY, J. NOVÁČEK, Z. Reconstruction of the radiation patterns from data with limited knowledge of the phase. In *Proceedings ZVŮLE 2008*. 2008. s. 220-223. ISBN: 978-80-214-3709-8.

[55] PUSKELY, J. NOVÁČEK, Z. Directivity pattern reconstruction from phaseless near- field measurements. In *Proceedings of the International Traveling Summer School on Microwaves and Lightwaves 2008*. Praha: 2008. s. 231-236.

[56] PUSKELY, J. NOVÁČEK, Z. Application of the Global Optimization Approaches To Planar Near-Field Antenna Phaseless Measurements. *Radioengineering*. April 2009, Vol. 18, No. 1, pp. 9 - 17. ISSN 1210-2512.

[57] PUSKELY, J. NOVÁČEK, Z. New Look to Real Valued Genetic Algorithm Used to Reconstruct Radiation Patterns. In *Proceedings of the 15th Conference Radioelektronika 2009*. 2009.

[58] PUSKELY, J. NOVÁČEK, Z. Reconstructing Radiation Patterns Using Amplitude Measurements on Cylindrical Surfaces. In *Proceedings of the International Conference on Electromagnetics in Advanced Applications ICEAA 2009*. Torino, Italia: 2009. s. 52-56.

[59] PUSKELY, J. NOVÁČEK, Z. Reconstruction of the radiation patterns from amplitude measured on cylindrical surface. In *Electronic proceedings Sireni vln v blizke a vzdalene zone anteny*. Pardubice: Univerzita Pardubice, 2009. s. 21-28. ISBN: 978-80-7395-172- 6.

[60] PUSKELY, J. POKORNÝ, M. Evaluating electromagnetic distribution in vicinity of commercial antennas. In *Proceeding of the 13th International Student Conference on Electrical Engineering POSTER 2009*. Praha: 2009. s. 125-128.

[61] PUSKELY, J. NOVÁČEK, Z. Computing of the EM field from only amplitude measurement on cylindrical surfaces. In *Proceedings Králíky 2009*. Brno, Czech Republic: 2009. s. 221-225. ISBN: 978-80-214-3938- 2.

[62] PUSKELY, J. NOVÁČEK, Z. Design of algorithm reconstructing radiation patterns using only amplitude measurements on cylindrical surfaces. In *Proceedings of the International Traveling Summer School on Microwaves and Lightwaves 2009.* Roma, Italia: 2009. s. 345-352.

[63] PUSKELY, J. NOVÁČEK, Z. Comparison of Different Approaches for Reconstruction of Radiation Patterns. In *Proceedings of the 14th Conference on Microwave Techniques COMITE 2010.* Brno: 2010. s.199-202. ISBN:978-4244-6351-0.

[64] PUSKELY, J. NOVÁČEK, Z. Reconstruction of Antenna Radiation Pattern at 310 GHz Using Image Compression Methods. In *The proceedings of EuCAP 2010.* Barcelona, Spain: 2010. s. 1-5.

[65] PUSKELY, J. NOVÁČEK, Z. Exploiting of the Compression Methods for Reconstruction of the Antenna Far-Field Using Only Amplitude Near-Field Measurements. *Radioengineering,* 2010, Vol. 19, No. 2, s. 299-306. ISSN: 1210- 2512. 2010

[66] PUSKELY, J. NOVÁČEK, Z. Far-Field Reconstruction Based on Compression Method from Cylindrical Near-Field Phaseless Measurements. In *Proceedings of the International Conference on Electromagnetics in Advanced Applications ICEAA 2010. Sydney*, Australia: 2010. will be published

Curriculum Vitae

Name: Ing. Jan Puskely
Date of birth: September 7th, 1982
Nationality: Czech republic
Address: Hranická 6, 75124 Přerov
E-mail: puskely.jan@seznam.cz

Education:

Since 2007   Department of Radio Electronics (DREL),
                 Faculty of Electrical Engineering and Communication (FEEC),
                 Brno University of Technology (BUT)
                 Ph.D. Study, Doctoral Thesis: *"Reconstruction of the antenna near field"*

2005 – 2007   DREL, FEEC, BUT
                 M.Sc. Study, Diploma Thesis: *"Broadband antennas for EMC testing"*

2002 – 2005   DREL, FEEC, BUT
                 B.Sc. Study, Bachelor Thesis: *"Baluns"*

Awards:

2009   Best Paper Award on Student Conference POSTER 2009,
                 MTT/AP/ED/EMC Joint Chapter of the Czechoslovak Section of IEEE.

2009   The Student Conference POSTER 2009, 2nd place.

Experiences:

05-06 / 2010   Microwave Laboratory, DEIS, University of Calabria, Italy; aimed to
                 antenna near-field phaseless measurement techniques

04 / 2009   TKK Helsinki University of Technology, Espoo, Finland; aimed to
                 antenna measurements at millimeter and submillimeter wavelengths

2008 - 2010   Chairman of IEEE Student Branch Brno University of Technology

Projects and grants:

2007- 2009   co-investigator at project of the Grant Agency of the Czech Republic
                 „Near Field of Antenna Arrays"

2008 - 2010   member of the Ph.D. student's team at project of the Grant Agency
                 of the Czech Republic „Modeling and simulation of fields"

2009 - 2010   involved in projects „Antennas for Car2Car Communication",
                 supported by the Volkswagen, Germany

2009   obtained grant „Innovations of laboratory experiments in the course
                 Electromagnetic waves, antennas and lines" supported by the
                 Ministry of education of the Czech republic, Prague

2010   involved in projects „Novel technology for microwave links",
                 supported by the TESLA Pardubice, Czech republic

Specialization:

Analysis and design of antennas, modeling and simulation of microwave and RF structures, antenna measurement, EMC, design of radio and microwave links

Languages: English – communication level